Rydberg ionisation into confined and discrete systems

Jemma A Gibbard

Corpus Christi College, University of Oxford

A thesis submitted for the degree of Doctor of Philosophy

Trinity 2015

Rydberg ionisation into confined and discrete systems

Jemma A Gibbard, Corpus Christi College

A thesis submitted in partial fulfilment of the requirements for the degree of
Doctor of Philosophy at the University of Oxford
Trinity Term, 2015

Abstract

The energy levels of a hydrogen Rydberg atom approaching a metallic structure are perturbed by the image-charge interaction with the surface. At small atom-surface separations surface ionisation of the Rydberg electron can occur, whereby the electron is transferred to a metal-localised state. In previous studies investigating surface ionisation at bulk metallic surfaces, this state has been part of a conduction band; however this thesis focuses on metallic and structured surfaces where the Rydberg electron transfers into a discrete image-state or hybrid 'well-image state'.

The surface ionisation of hydrogen Rydberg atoms at a Cu(100) projected band-gap surface is investigated experimentally and theoretically. Experimentally, the surface ionisation of an incident beam of hydrogen Rydberg atoms is measured by extraction of the resulting ions. Resonance-enhanced charge transfer is seen for hydrogen Rydberg states that are degenerate with copper-localised image-states. A wavepacket propagation study shows that for on-resonance states the maximum in the surface-ionisation probability is shifted away from the surface by decreasing the collisional velocity.

The discrete hybrid 'well-image states' localised along the surface normal of a thin-film change energy with thin-film thickness. The interaction of hydrogen Rydberg atoms with iron thin films deposited on an insulating substrate is investigated. The preference for electron penetration along the surface normal is seen by the resonance-enhancement of charge transfer at energies where the Rydberg state and well-image state are degenerate. By changing the thickness of the thin film, by in situ depositions, the energies of the well-image state are altered and the Rydberg n-values at which resonances occur, change. At a thickness of 30-monolayer the energetic spacings between the well-image states and the Rydberg states become comparable, and the single well-image state resolution is lost.

A wavepacket-propagation study investigates the interaction of a nanoparticle and low-n hydrogen Rydberg atoms. The nanoparticle has a fully confined potential which at small radii yields well-spaced, fully discrete well-image states. Resonance-enhanced charge transfer occurs when the Rydberg state and the nanoparticle well-image state energy levels are degenerate. However, when there is poor energy matching between the nanoparticle well-image state and the Rydberg atom, no charge transfer is seen i.e. surface ionisation does not occur.

Overall, the work presented here demonstrates the capability of Rydberg-surface studies to identify discrete, high-lying energy levels at specific surfaces.

Acknowledgements

I would like to thank my supervisor Tim Softley for all of his time, help and support, and the rest of team Softley for their friendship throughout. Tim has encouraged me with my experiments, helped me to understand the results and been willing to read endless drafts of this thesis.

Of all the group, I am particularly grateful to my fellow Rydbergers. When I first joined the group Eric taught me all about the wavepacket propagation method and the theoretical work in this thesis is heavily indebted to him. Mark D helped me get started working in lab. Chris has worked with me for the last couple of years on the experiment and he has always been willing to help in the lab, read mountains of written work or drive us to Alton Towers. Finally I must say thank you to Mike, who has been patient through several years of no signal and subsequent 'sharing' of the experiment.

My eight years in Oxford have been defined by my friends, and I am grateful to all of them, whether they are here now or not, for their friendship and support. I would like to thank my Corpus friends Krishna, Johnathan and Dan for making my first year really fun, and Angie, Min and Matt for reminding me of Hilda's throughout. A special mention must go to Jemma though, who has done her Dphil at the same time and really understands when things go wrong!

Most importantly I must thank my family. My Mum and Dad have supported me in everything I do and I feel lucky to have them. My little sister Jess has been an exceptional housemate and has made the last couple of years a lot more fun!

Contents

Chapter 1

Introduction

The collision of a gas-phase Rydberg atom or molecule with a solid surface typically leads to transfer of the Rydberg electron to the surface at atom-surface separations less than $4n^2a_0$ [1], where n is the principal quantum number of the Rydberg electron and a_0 is the Bohr radius. This is especially true for metallic surfaces, for which the Rydberg electron energy is degenerate with the conduction band of the metal so that resonant charge transfer occurs. In general there are two sets of parameters to investigate, the properties of the Rydberg atom or molecule and the properties of the surface. Work to date has primarily focused on the first of these. Experimental and theoretical studies of this phenomenon have focused on the effects of varying the n quantum number [1–3], the parabolic quantum numbers n_1 and n_2 [4, 5], the velocity of the incoming particle and the applied fields [5–7], and observing how the rate of ionisation varies as a function of distance from the surface [8] .

Experimental studies have been primarily conducted with flat metal surfaces, for which the ionisation dynamics are almost independent of the

material used because of the rather generic behaviour of resonant charge transfer to the conduction band. There have also been some experimental and theoretical investigations into the effects of adlayers and thin dielectric films [9], the influence of the band gap in semiconductor surfaces [10], and the effects of corrugation and patch charges [11]. All these studies point to a degree of sensitivity of the charge transfer process to the surface physical and electronic structure.

This thesis focuses on the surface ionisation of hydrogen Rydberg atoms at surfaces which have discrete image-states in the coordinate along the surface normal, such as projected band gap surfaces, thin films and nanoparticles. The experiments and related theory presented in this thesis demonstrate that the surface ionisation dynamics of a Rydberg atom provide a sensitive probe of the electronic structure of a surfaces with discrete states. Additionally the experiments presented in this thesis show a new way to probe high-lying image-states in these confined systems.

1.1 Rydberg atoms and their properties

Rydberg atoms are electronically excited species with one valence electron occupying a hydrogenic orbital of large principal quantum number n. A neutral Rydberg atom consists of an excited electron and a positively charged ion. To a first approximation it can be assumed that the Rydberg electron moves under a hydrogenic Coulomb potential due solely to the electrostatic interaction with the positively charged ion. The large separation between the ion and the electron makes this a reasonable assumption. The average

orbital radius is large ($r = a_0 n^2$), as is its orbital period ($\Omega_n = n^3/2\pi$) [12]. For an $n = 30$ hydrogen atom the Rydberg orbital radius is 48nm and the classical Rydberg orbital period is 103fs. The principal quantum number n, the orbital angular momentum quantum number l and the magnetic quantum number m_l are used to describe the Rydberg electron wavefunction.

1.1.1 Rydberg series

The energy of the electron within an atomic Rydberg state, $E_{n,l}$, is given by the Rydberg formula [12],

$$\frac{E_{n,l}}{hc} = -\frac{R_H}{(n - \delta_l)^2} \tag{1.1}$$

where h is Planck's constant, c is the speed of light, $R_H = 109677.583\text{cm}^{-1}$ is the Rydberg constant, and δ_l is the l-dependent quantum defect. Shielding of the nucleus in many–electron atoms is accounted for by the quantum defect.

For hydrogen atom Rydberg states, as considered in this thesis, there are no additional electrons to shield the nucleus from the Rydberg electron, therefore $\delta_l = 0$. This leads to all the l states within the same n manifold being degenerate, such that the energy of a hydrogen Rydberg atom in the absence of an external field is determined to a very good approximation by n. At a higher level of approximation effects such as spin–orbit coupling, the lamb shift and nuclear spin interaction lead to small deviations from equation 1.1, but these terms are not considered in this thesis.

1.1.2 Properties of Rydberg atoms

Many of the properties of Rydberg atoms (and molecules) are a result of their characteristic large orbital radius and low binding energy. Individual quantum states may be studied, as a combination of tuneable laser excitation and electromagnetic fields allows for high-level control of state selectivity [13]. In the presence of a surface, it is possible to orient the electron density of a hydrogen Rydberg atom towards or away from the surface [5].

Rydberg atoms are highly polarisable ($\propto n^7$). The large dipole moment makes it possible to deflect [14,15] and decelerate [15] Rydberg atoms far more easily than ground state species. In the future, a Rydberg chip–decelerator [16] will be added to the hydrogen Rydberg–surface experimental setup in our lab to allow deceleration of the Rydberg hydrogen atoms in front of the surface. It is the large dipole moment which also makes Rydberg atoms sensitive to perturbing electric fields, such as the presence of a surface.

Rydberg states have relatively long lifetimes with respect to spontaneous decay ($\propto n^3$) and blackbody radiation stimulated decay ($\tau_{n,l}^{bb} = 3n^2/4\alpha^3 k_B T$) [12], where α is the fine structure constant, k_B is the Boltzmann constant and T is temperature. For example the hydrogen Rydberg atom in the $10s$ state has a radiative lifetime of 1µs [12]. This is due to the large orbital radius and the relatively short time the electron spends near the nucleus. Additional decay channels are possible for molecular Rydberg states such as autoionisation and predissociation [13, 17]. However these decay pathways make the ionisation dynamics of molecular Rydberg states more complicated and such states are not considered in this thesis.

1.2 Rydberg atoms in an electric field

The presence of a homogeneous electric field mixes the angular momentum states within the degenerate n-manifolds. This is known as the Stark effect. The resulting perturbed states have different spatial distributions of electron density and may have large dipole moments aligned along the field axis. Direct field ionisation of the Rydberg atom can occur at large field strengths.

The interaction of a Rydberg atom with a metal surface is akin to a dipole-dipole interaction. It is shown in section 1.3.2 that the perturbation of the energy levels and wavefunction of the Rydberg electron by the surface is similar to that of the Stark effect.

1.2.1 The Stark effect in hydrogenic systems

In the presence of an external electric field, hydrogenic systems experience the linear Stark effect, whereby the magnitude of the perturbation is proportional to the field strength, F. In the absence of an electric field each n-manifold is n^2-fold degenerate. The Hamiltonian for the system in the presence of a homogeneous electric field F oriented along the z axis is:

$$H = H^0 + H^1 \tag{1.2}$$

$$H^0 = -\frac{1}{2}\nabla^2 - \frac{1}{r} \tag{1.3}$$

$$H^1 = -\widehat{F}.\widehat{\mu} = -F\mu_z = +Fr\cos\theta \tag{1.4}$$

Here $\widehat{\mu}$ is the dipole moment operator and μ_z is its z-component with the whole system defined in terms of spherical polar coordinates. H^0 is the zero–

field Hamiltonian and H^1 is the perturbing Stark Hamiltonian. Using the hydrogenic wavefunctions, the eigenfunctions of H^0 $|nlm_l\rangle = R_{n,l}(r)Y_{l,m_l(\theta,\phi)}$ as a basis set, the matrix elements of H^1 are,

$$\langle n'l'm'_l \,|Fr\cos\theta|\, nlm_l\rangle = F\,\langle n'l' \,|r|\, nl\rangle\,\langle l'm'_l \,|\cos\theta|\, lm_l\rangle \tag{1.5}$$

Non-zero matrix elements are derived from the orthogonality relations of the spherical harmonics $Y_{l,m_l}(\theta,\phi)$ with $m'_l = m_l$ and $l' = l \pm 1$ [18]. For non–zero values this leads to the selection rules $\Delta m_l = 0$ and $\Delta l = \pm 1$ for the field in the z direction. In the presence of a homogeneous external field the symmetry of the potential is reduced from spherically symmetric to cylindrically symmetric about the z or field axis. l is not conserved as the total orbital angular momentum vector $\widehat{\underline{l}}$ precesses around the z axis. Therefore l is no longer a good quantum number such that only m_l is conserved.

The Schrödinger equation derived from the Hamiltonian in equation 1.4, using the parabolic coordinate basis (ζ,η,ϕ),

$$\zeta = r + z, \quad \eta = r - z, \quad \phi = \arctan\frac{y}{x} \tag{1.6}$$

is separable and therefore exactly solvable for a hydrogenic system [18].

The normalised eigenfunctions determined by solving the Schrödinger equation are,

$$\Psi_{n_1 n_2 m_l} = \frac{e^{\pm i m_l \phi}}{\sqrt{\pi n}} \frac{n_1!^{\frac{1}{2}} n_2!^{\frac{1}{2}} e^{\frac{-(\zeta+\eta)}{2n}} (\zeta\eta)^{\frac{m_l}{2}} L^{m_l}_{n_1+m_l}(\zeta/n) L^{m_l}_{n_2+m_l}(\eta/n)}{n^{m_l+\frac{3}{2}}(n_1+m_l)!^{\frac{3}{2}}(n_2+m_l)!^{\frac{3}{2}}} \tag{1.7}$$

where $L^{m_l}_n(x)$ are the Laguerre polynomials and n_1 and n_2 are the new

parabolic quantum numbers. These quantum numbers define the number of nodes in the parabolic coordinates ζ and η respectively. The parabolic coordinate quantum numbers are related to the spherical coordinate quantum numbers by:

$$n = n_1 + n_2 + |m_l| + 1 \tag{1.8}$$

The parabolic quantum numbers n_1 and n_2 are often described in terms of $k = n_1 - n_2$, which is a measure of the electron density along the z axis. It can take $(n - m_l)$ integer values ranging from $-(n - |m_l| - 1)$ to $(n - |m_l| - 1)$. The electron probability density is given by expressing equation 1.7 in spherical polar coordinates and taking the absolute squared magnitude:

$$|\Psi_{nn_1n_2m_l}(r, \theta, \phi)|^2 = r^{2n-2}(1 + \cos\theta)^{2n_1+|m_l|}(1 - \cos\theta)^{2n_2+|m_l|}e^{-\frac{2r}{n}} \tag{1.9}$$

A positive k state is known as a 'blue-shifted' Stark state because it increases in energy with field and corresponds to electron density located along the $+z$ axis, whereas a negative k value corresponds to a 'red-shifted' Stark state and has electron density directed along the $-z$ axis. For $k = 0$ the electron density is distributed fairly isotropically in the z plane with angular nodes. Field ionisation characteristics are strongly determined by the k value of a Rydberg state.

The Schrödinger equation may be solved exactly for a hydrogen atom in a field. However, rather than calculating these solutions numerically, the energy levels may also be approximated analytically using perturbation theory yielding the energy of a hydrogenic Stark state in a given field as a series

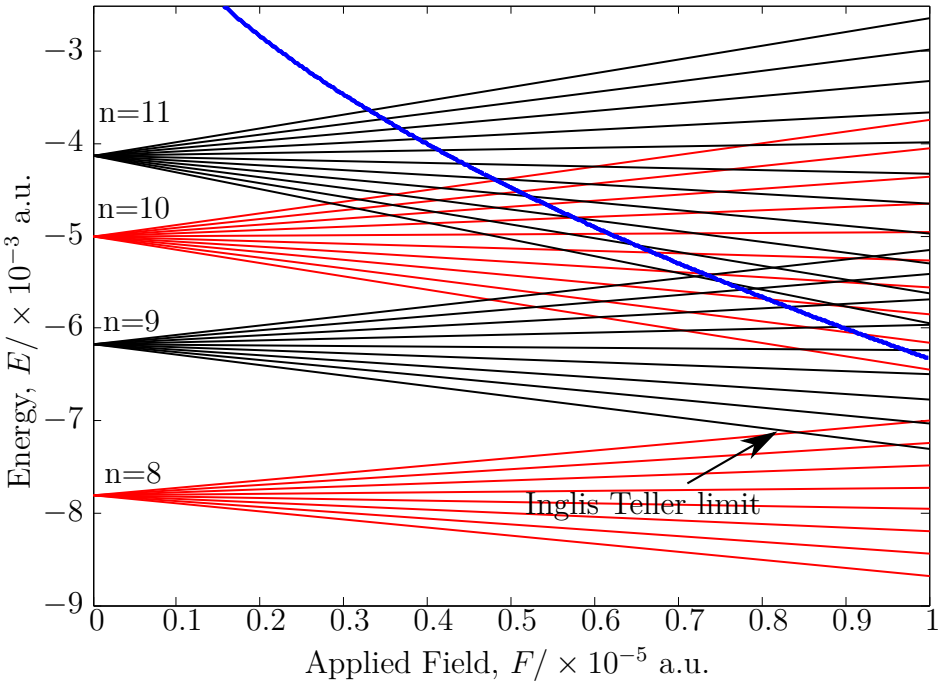

Figure 1.1: The Stark state energies of the $m_l = 0$, $n = 8 - 11$ hydrogen atom Rydberg series as a function of applied field given by equation 1.10. The Inglis-Teller limit defines the field dependent crossing of neighbouring manifolds. The k manifolds of $n = 8$ and $n = 10$ are red, and the others black. The blue line shows the classical field ionisation limit given by $-2\sqrt{F}$ and described in subsection 1.2.2.

expansion [19],

$$E^{\text{Stark}}_{n,m_l,k}(F) = -\frac{1}{2n^2} + \frac{3}{2}nkF - \frac{1}{16}[17n^2 - 3k^2 - 9m_l^2 + 19]F^2 + O(F^3) + ... \quad (1.10)$$

At low field strengths, the Stark splitting for a given n-manifold is linearly dependent on the magnitude of the electric field F, giving rise to the term 'linear Stark splitting' for hydrogenic systems (i.e. $E \propto F$). The energy of the Stark states of the $n = 8 - 11$ hydrogen Rydberg atoms are shown in figure

1.1 as a function of applied field. At larger external fields the higher-order corrections ($F^2, F^3, ...$) become more significant and the degeneracy associated with the m_l quantum number is lifted. It should be noted that the manifold of Stark states arising from an even m_l state are not degenerate with those arising from an odd m_l state, as for a given n they give rise to a different series of k-states as described by equation 1.8. At sufficiently large field strengths the most blue-shifted state of a given n-manifold crosses the most red-shifted state of the $(n+1)$-manifold. In figure 1.1 this is where the most red-shifted state in the $n = 9$ manifold crosses the neighbouring extreme blue-shifted state of the $n = 8$ manifold. This is known as the Inglis-Teller limit. In hydrogenic systems this is a 'real' crossing as the off-diagonal matrix elements are zero, i.e. there is no interaction between neighbouring states. However for non-hydrogenic systems this is not the case and avoided crossings occur.

1.2.2 Field Ionisation

The application of an external electric field along the z axis modifies the Coulombic potential V_{Coulomb}, by addition of the Stark potential V_{Stark} forming the Coulomb-Stark potential $V_{\text{Coulomb-Stark}}$,

$$\mathrm{V}_{\text{Coulomb-Stark}} = \mathrm{V}_{\text{Coulomb}} + \mathrm{V}_{\text{Stark}} = -\frac{1}{r} + Fz \tag{1.11}$$

As illustrated in figure 1.2 there is a saddle point at $z = -1/\sqrt{F}$ with $V_{\text{Coulomb-Stark}} = -2\sqrt{F}$, in atomic units. As this is a one–dimensional potential, the ion to electron separation $r = |z|$. In figure 1.1 the blue line is the classical ionisation energy $(-2\sqrt{F})$ of a hydrogen Rydberg atom in

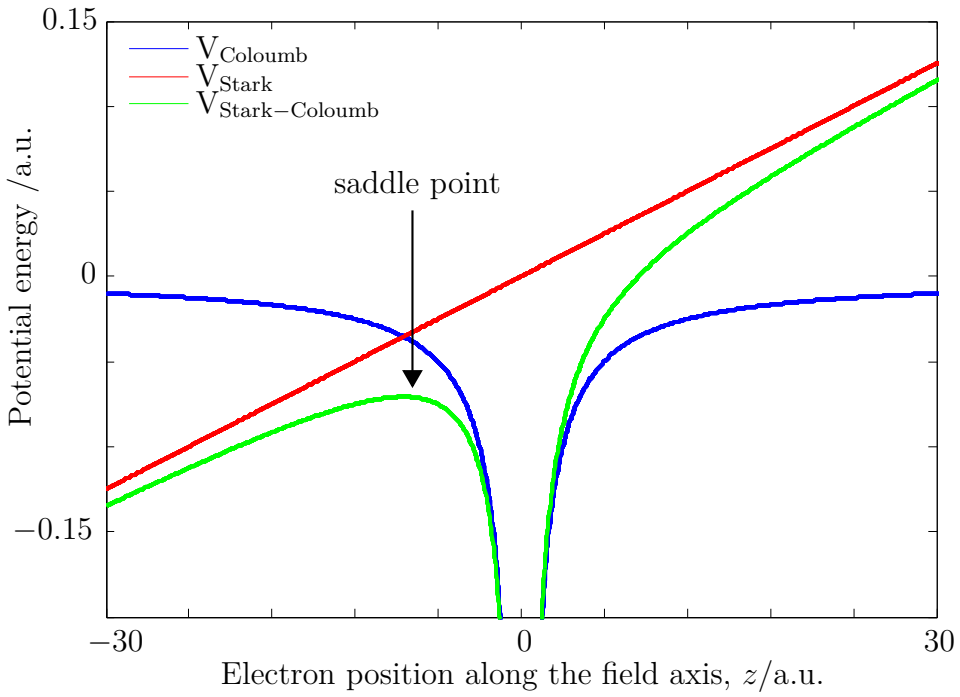

Figure 1.2: The combined Coulomb and Stark potential $V_{\text{Stark}-\text{Coulomb}}$, and the constituent Stark and Coulomb potentials. The saddle point in the green curve drops to lower energy as the external field is increased, and field ionisation becomes easier. The ion core is located at $z = 0$.

the presence of an external field. At fields larger than this field ionisation of the Rydberg atom will be energetically favourable, however the rate of field ionisation will be largely dependent on the k-state of the Rydberg atom. Classical ionisation corresponds to the electron occupying a state which is higher in energy than the saddle point, whereas states that are lower in energy are classically bound. However, the barrier is of finite width so all states may be field ionised via tunnelling through the potential barrier. Consequently all energy levels are metastable with respect to ionisation, but the lifetimes of those which lie below the saddle point in energy are very long i.e. Stark

states in figure 1.1 at fields lower than the blue line of classical ionisation energy are relatively stable. States which lie above the saddle point in energy do not ionise immediately but have a finite lifetime on an experimentally observable time scale.

As a blue-shifted hydrogenic state lies higher in energy than a red-shifted state of the same n it would be reasonable to expect that the blue-shifted state would ionise faster. However experimental studies show that the converse is true. The electron density of a blue-shifted Stark state is orientated along the $+z$ axis, away from the saddle point, as described by the parabolic quantum number k and equation 1.9. However the electron density of the red-shifted Stark state is located along the $-z$ axis, towards the saddle point. Therefore blue-shifted hydrogenic Stark states are kinetically more stable and ionise slower than their red-shifted counterparts.

For hydrogenic systems diabatic field ionisation occurs. In the diabatic regime no coupling between neighbouring n-manifolds occurs and Stark states can cross whilst maintaining their own character with increasing field strength. In contrast non–hydrogenic systems may show adiabatic behaviour at crossings leading to different field ionisation characteristics [4]. The diabatic field ionisation behaviour of hydrogen atoms makes them a useful choice for the Rydberg surface ionisation experiments described in this thesis [5].

1.3 Ionisation at Metallic Structures

Ionisation of a Rydberg atom at a metallic structure occurs via resonant charge transfer of the Rydberg electron from its localised atomic orbital to an

unoccupied metallic state, which is degenerate in energy. Depending on the electronic structure of the surface this may be a discrete state, or one within a band. Following ionisation of the Rydberg atom the positively charged ion will accelerate towards the surface under the influence of its image charge, where it is neutralised via an Auger process [20]. Experimentally, a large positive potential is applied to the metal surface to repel the ion before neutralisation and allow it to be detected as described in section 4.1.4 [5].

1.3.1 Perturbation of energy levels due to the surface

At long range, the presence of a Rydberg atom induces an instantaneous polarisation of the electron density within the metal. This can be described as a long range dipole-dipole interaction. First–order perturbation theory can be used to approximate the energy shift of the atomic Rydberg energy levels due to the presence of the surface. At large atom-surface separations, D, the surface potential is approximated by the dipole-dipole attraction [21],

$$\mathrm{V}_{\mathrm{dipole-dipole}} = -\frac{1}{16D^3}(r^2 + z^2) \tag{1.12}$$

where r and z are the electron coordinates in the ion frame, as illustrated in figure 1.3. The dipole-dipole interaction potential is an additional perturbation to the combined Coulomb-Stark potential depicted in figure 1.2. The energy of a Stark state in the presence of an electric field F and at atom-surface separation D is approximated by [22],

$$E_{n,m_l,k}(F,D) \approx E^{\mathrm{Stark}}_{n,m_l,k}(F) - \frac{n^2}{64D^3}(8n^2 + 8 - 4m_l^2 + 12k^2) \tag{1.13}$$

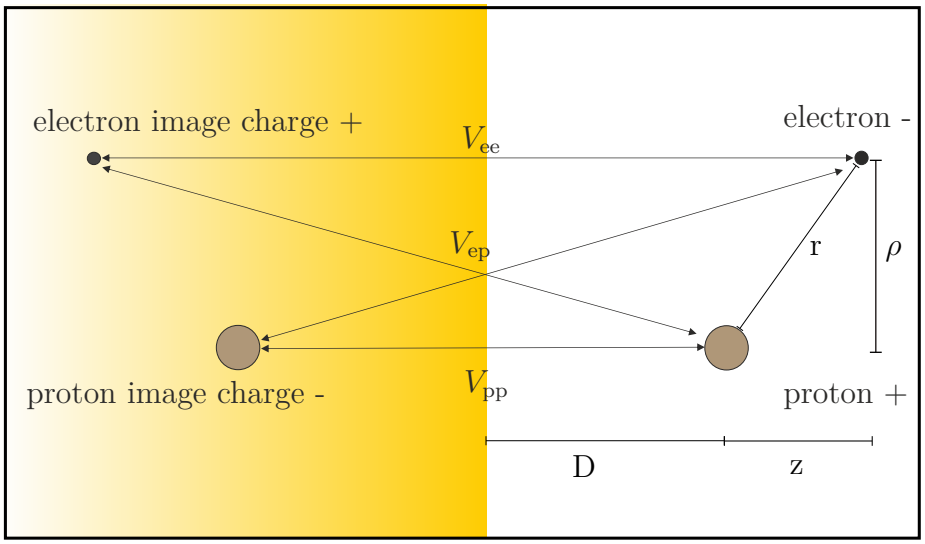

Figure 1.3: The image–charge model and the geometry of the interaction of a Rydberg state and a surface. The electron coordinates are r and z, and the atom-surface separation is D.

where $E^{\text{Stark}}_{n,m_l,k}(F)$ is the energy of the Stark state in the presence of an external electric field, as given by equation 1.10. The presence of the surface therefore lowers the energy of a state within this theoretical framework. Equation 1.13 is only valid at large atom–surface separations where the rate of charge transfer and orbital overlap is insignificant, and the dipole-dipole potential is a valid description of the surface potential.

1.3.2 Image–Charge model

In order to understand the origin of the surface potential it is useful to consider the classical image charge model. This provides a simple analytical way of describing the interaction between a Rydberg atom and the surface.

The image–charge model treats the Rydberg electron and ion as single point charges. Near a surface these point charges induce image-charges within

the surface. The surface potential is the sum of the interactions between the four point charges, as shown in figure 1.3. z is the Rydberg electron's z coordinate relative to the ion, r is the Rydberg electron ion separation and D is the atom surface separation. The attractive electron and electron-image interaction V_{ee}, the repulsive electron-image proton interaction V_{ep} (and the identical proton electron-image interaction), and the attractive Coulombic interaction between the Rydberg electron and ion V_{Coulomb} are considered explicitly in the calculations in this thesis. The attractive proton proton-image interaction V_{pp} lowers the energy of all electronic states, both those of the surface and the Rydberg atom, by the same amount for a given atom-surface separation and so does not affect the dynamical properties of the system, with the exception of the mean field calculations in which the acceleration of the ion under the influence of its own image charge is treated explicitly, as described in section 2.4.

$$V_{\mathrm{total}} = V_{\mathrm{Coulomb}} + V_{\mathrm{surface}} = V_{\mathrm{Coulomb}} + V_{\mathrm{ee}} + V_{\mathrm{ep}} \tag{1.14}$$

It should be noted that the image–charge model creates the correct electrostatic field by treating the blurred charge localisation at the surface-vacuum interface as a point charge further from the surface. The situation is analogous to an optical reflection in a mirror, whereby the reflected object appears to be deep within the mirror, but in reality is localised at the mirror plane.

A classical model of point charges can adequately describe the interaction potentials at large distances from the surface. The classic image-charge potential breaks down at small atom–surface separations and within the

metal. The asymptotic form of the potential for hydrogen is given by,

$$\lim_{D,(z+D)\to\infty} V_{\text{surface}}(z, D, \rho) = V_{ee}(z, D) + V_{ep}(z, D, \rho) \tag{1.15}$$

where,

$$\lim_{D,(z+D)\to\infty} V_{ee}(z, D) = -\frac{1}{4(z+D)} \tag{1.16}$$

$$\lim_{D,(z+D)\to\infty} V_{ep}(z, D, \rho) = \frac{1}{\sqrt{(z+2D)^2+\rho^2}} \tag{1.17}$$

where $\rho = \sqrt{r^2 - z^2}$.

While this classical model represents the bound states of a Rydberg atom near a surface, to model the surface ionisation of Rydberg atoms a potential is required that interpolates between the finite bulk potential of the metal and the asymptotic limit. By this consideration the classical image charges are clearly unsuitable.

Various one dimensional pseudo-potentials have been proposed to account for V_{ee} at small D, often based on the invariance of the surface under rotation along the surface normal. The cylindrical symmetry in the system also results in the conservation of m_l. The analytical Jellium model proposed by Jennings *et al.* [23] can be used as a free metallic surface potential in this case, and corrugated potentials such as the Chulkov potential [24], can capture more complex features of the surface. These are discussed in more detail in section 2.3.2.

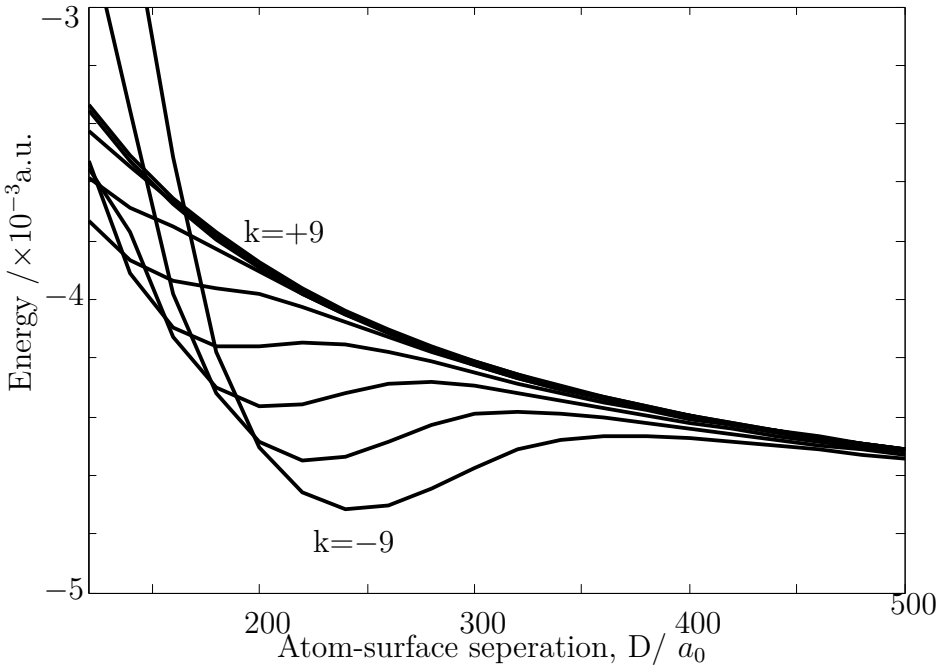

Figure 1.4: The energy of the Stark states of the n=10 hydrogen Rydberg atom on approach to a metal surface calculated using a complex scaling method [25, 26].

1.3.3 Surface Ionisation

The presence of a metal surface perturbs and mixes the zero-order wavefunctions of Rydberg states, even at relatively large atom-surface separations, inducing direct coupling and l-mixing between the excited Rydberg states. The surface potential also breaks the z parity of the system and this loss of symmetry causes avoided crossings between states within the n-manifold. States with the same m_l mix forming hybridised Stark states. Degeneracy within the n-manifold is lost as a variety of surface–orientated and vacuum–orientated states are formed, which have their electron density localised

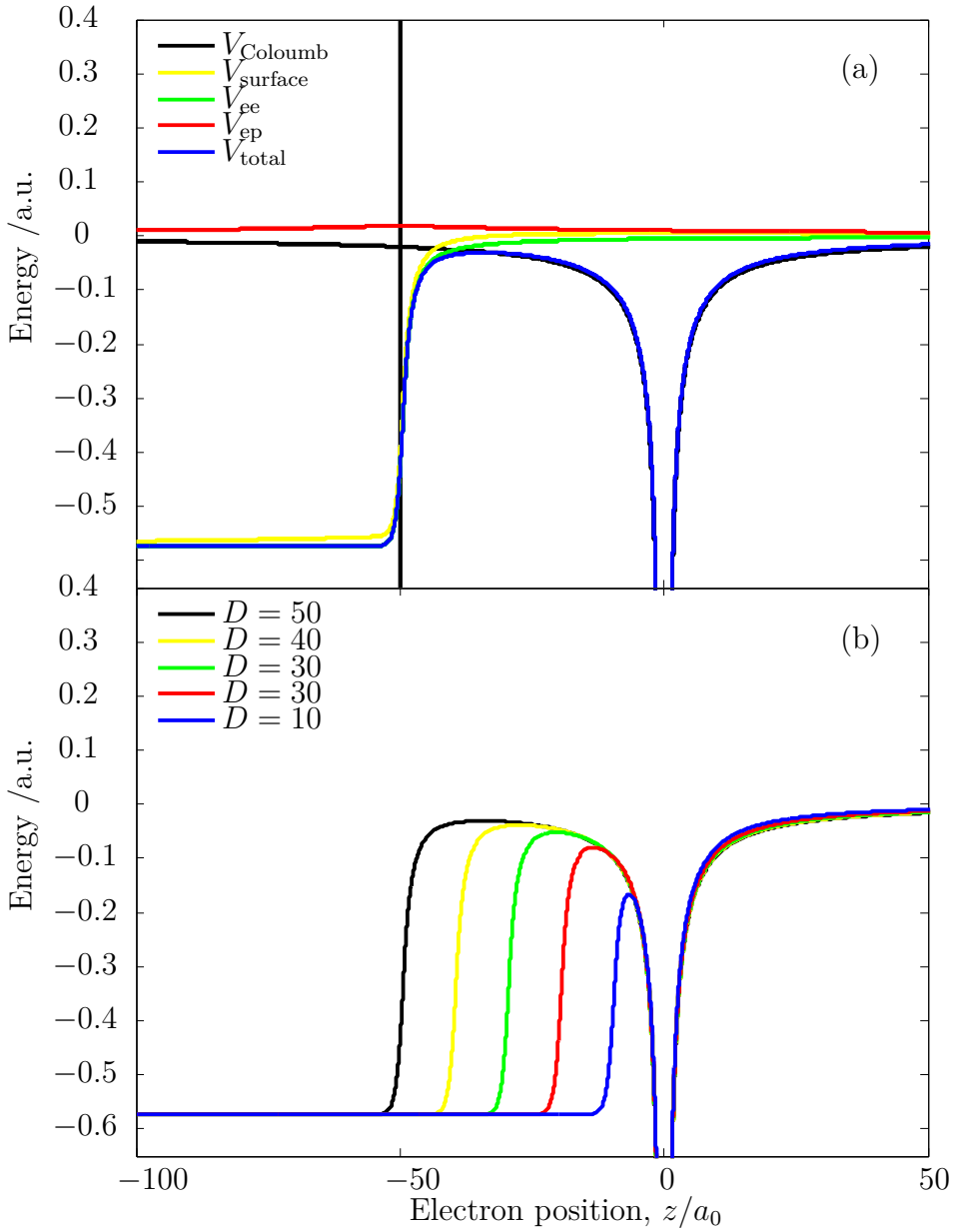

Figure 1.5: (a) The electron image electron interaction V_{ee}, the proton image electron interaction V_{ep}, the Coulomb potential V_{Coulomb}, the surface potential V_{surface} and the total potential experienced by the Rydberg electron V_{total}. The surface is located at $z = -50a_0$, as shown by the vertical black line, and the ion is at $z = 0a_0$. (b) The atom–surface separation D is decreased so that the height and width of the barrier to surface ionisation is decreased.

between the ion and the surface, or behind the ion oriented into the vacuum respectively.

Figure 1.4 shows the energies of the different Stark states of the $n = 10$ hydrogen atom Rydberg state on approach to a surface. Clearly the energy of the Rydberg state changes on approach to a surface, and the magnitude of the change is largely dependent on the k-state. Such that more surface-orientated states exhibit a minimum in energy further from the surface, than the vacuum-orientated states which continue to rise in energy on approach to the surface.

Figure 1.5 shows the full potential experienced by the Rydberg electron, which is a combined Coulombic attraction to the ion V_{Coulomb} and the surface potential, V_{surface}. Within the metal surface the potential takes a constant, element specific value which describes the binding potential of an electron within the bulk metal, i.e., not at the surface. A saddle point is seen in total potential experienced by the electron, represented by the blue line in figure 1.5(a), along the surface normal. This potential barrier between the ion and the surface is similar to the one observed for the case of a Rydberg atom in an external electric field as described in section 1.2.1. Classically, surface ionisation can be understood to occur when the D-dependent barrier height is less than the electron binding energy. This is known as 'over-the-barrier' surface ionisation. A quantum mechanical view of ionisation allows tunnelling through the barrier, and allows discrete energy states in the metal.

In figure 1.5(b) it is shown that decreasing atom–surface separation results in a decrease in the height and width of the barrier to surface ionisation. The decreasing height permits more over-the-barrier ionisation, and the decreasing

width increases the rate of tunnelling through the barrier. Both of these increase the rate of surface ionisation.

As discussed in subsection 1.2.1 in the presence of an external electric field the hydrogen atom experiences a linear Stark effect, where the degeneracy of an n-manifold is broken. The presence of a surface causes a similar breaking of degeneracy, however the associated loss of symmetry causes avoided crossings rather than the actual crossings seen in the diabatic limit of the hydrogenic Stark effect. The differing orientations of electron density caused by the presence of a surface, are analogous to the different k states, but the exact location of the electron density differs from the Stark effect, because the field is not homogenous.

Red-shifted states in the presence of a surface are lower in energy but surface oriented, whereas blue-shifted states are higher in energy but vacuum oriented. Despite the smaller binding energy of the blue-shifted states the wavefunction is localised away from the saddle point meaning it is kinetically more stable to surface ionisation and so surface ionises at a lower rate compared to the red-shifted state.

Experimentally, the ionisation distances D_{ion} for an extreme red-shifted hydrogen atomic Rydberg state at a conducting metal surface is found to be $D_{\text{ion}} \approx 3.8n^2a_0$, whereas for an extreme blue-shifted state $D_{\text{ion}} \approx 1.2n^2a_0$ [27, 28]. Ionisation distances scale with the mean radius of the Rydberg electron ($\propto n^2$).

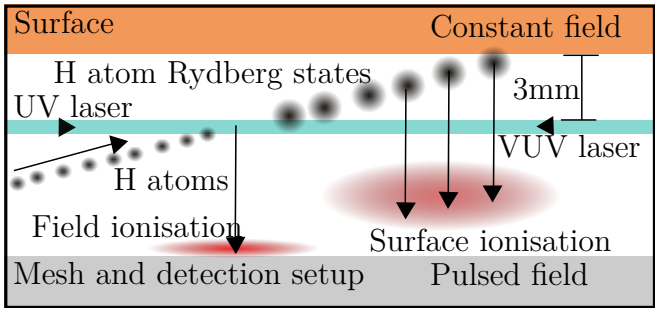

Figure 1.6: A schematic of the experimental setup, showing the excitation of hydrogen atoms to a Rydberg state, the field and surface ionisation processes and the extraction of the resultant ions.

1.3.4 Extracting ions after surface ionisation

In order to measure a 'surface ionisation signal', as described in section 4.1.4, the ions produced in the surface ionisation process must be extracted. As depicted in figure 1.6, a large external negative voltage is applied to a metal mesh opposite the surface a few microseconds after excitation of the Rydberg atoms. This applied field stops the ions colliding into the surface and being neutralised via an Auger process [20], and directs the ions into a TOF detector.

The field required to extract the ion is dependent on its perpendicular collisional velocity $v_\perp$ and on the atom–surface separation D_{ion} at the point of ionisation. After ion formation the ion starts at the Rydberg atom velocity $v_\perp$ and is accelerated by its image charge and decelerated by the applied field as it carries on moving towards the surface. When it reaches position D its kinetic energy is,

$$T(D) = T_0 + F(D - D_{\text{ion}}) + \frac{1}{4D} - \frac{1}{4D_{\text{ion}}} \tag{1.18}$$

where $T_0 = \frac{1}{2}mv_\perp^2$ is the perpendicular kinetic energy of the Rydberg atom

at the point of ionisation. The applied field, F, needs to be large enough to overcome the initial kinetic energy and the image–charge acceleration if the ion is to be extracted.

Necessarily, at the turning point of its trajectory the ion must have zero kinetic energy. Equating equation 1.18 to zero and multiplying through by D results in,

$$FD^2 - \left[FD_{\text{ion}} - T_0 + \frac{1}{4D_{\text{ion}}}\right]D + \frac{1}{4} = 0 \tag{1.19}$$

which is a quadratic in D. The quadratic only has real and non-trivial solutions when,

$$FD_{\text{ion}} - T_0 + \frac{1}{4D_{\text{ion}}} \geq \sqrt{F} \tag{1.20}$$

from the condition $b^2 \geq 4ac$ for a quadratic equation of the form $ax^2+bx+c = 0$. Multiplying through by D_{ion} and solving for $\sqrt{F}$ gives the well known result [29],

$$F_{\text{min}} = \left[\frac{1}{2D_{\text{ion}}} + \sqrt{\frac{T_0}{D_{\text{ion}}}}\right]^2 \tag{1.21}$$

where F_{min} is the minimum field required to extract the ion and prevent its collision with the surface. Any applied field less than F_{min} results in ions hitting the surface before being extracted and so not being detected.

Substituting this into equation 1.19 and realising that the quadratic can only have one root gives the turning point of the ion to be located at a distance,

$$D_{\text{Turn}} = \frac{F_{\text{min}}D_{\text{ion}} - T_0 + \frac{1}{4D_{\text{ion}}}}{2F_{\text{min}}} \tag{1.22}$$

Experimental surface ionisation profiles record the amount of ion signal from surface ionisation as a function of external field. By changing the

extraction field the detectable region of ionisation is altered. As the field is decreased, the detectable region is located further from the surface and the measured ion signal represents Rydberg atoms that surface ionise further from the surface.

However, above the field ionisation threshold, for isolated gas-phase atoms, the hydrogen Rydberg atoms are field ionised as soon as they are formed, independent of the surface. Above the threshold of field ionisation changing the applied electric field has little effect on the amount of ion signal recorded.

1.4 Previous studies investigating the surface ionisation of Rydberg atoms and molecules

The surface ionisation dynamics of Rydberg atoms have been studied extensively using theoretical and experimental methods. The primary focus of previous work has been to understand the effect the properties of the Rydberg atoms have on the surface ionisation process. The influence of the principal quantum number n [1], the parabolic quantum number k [5], the velocity of the incoming particle and applied fields [5, 6], and the rate of ionisation as a function of distance from the surface [8] have all been studied. Additionally for non-hydrogenic atoms, adiabatic and non-adiabatic passage through surface-induced energy level crossings play a key role in the evolution of the Rydberg state as it approaches the surface [4].

Fabre *et al.* sent a beam of sodium Rydberg atoms through a 'grating', to measure the transmission of the Rydberg atoms as a function of principal

quantum number [1]. The 'grating' was a series of 2μm slits in a thin gold film. The Rydberg atoms which pass through the slits are field ionised, and a field ionisation signal recorded. However some of the Rydberg atoms which pass through the slits surface ionise, and then are not measured in the field ionisation signal. Effectively the 'grating' acts as a 'sieve' to determine the atom-surface separation over which surface ionisation occurs. In this case a value of $D \approx 4.5n^2$ was determined.

Kocher *et al.* passed a beam of lithium Rydberg atoms through a gold mesh and measured the field ionisation signal of the Rydberg atoms which were transmitted [2, 3]. Those Rydberg atoms which had surface ionised at the mesh were not measured. The signal was found to vary repeatably with time, and as a function of temperature. This was attributed to the formation of an adsorbate layer of lithium atoms and other neutrals on the gold mesh, which changed the local fields near the mesh and increased the amount of surface ionisation seen.

Dunning *et al* investigated the surface ionisation of xenon Rydberg atoms at an Au(111), copper and Si(100) surface [4, 11, 27, 30]. Xenon atoms were selected as the the rare-gas does not react or stick to the surfaces in an attempt to reduce the effect of localised fields arising from the presence of adsorbate layers on the surface. By the application of a large applied field to the surface the ions produced via surface ionisation were extracted and measured, resulting in a surface ionisation profile, similar to the ones presented in this thesis. The magnitude of the field required to extract an ion allowed the atom-surface separation at which ionisation occurred to be calculated. In this case the atom-surface separation of surface ionisation was

approximately $D = (4.5 \pm 0.9)n^2 a_0$, which was similar to that predicted by hydrogenic calculations [6].

One of the more surprising results to arise from these experiments was the lack of surface ionisation dependence on the k state and the related electron distribution [4]. Excitation in the presence of a small Stark field allowed the preparation of extreme red and blue-shifted xenon Rydberg atoms. However the surface ionisation profiles for both red- and blue-shifted Rydberg atoms were the same. This was attributed to the mixing of Rydberg states in the presence of the large applied field and the surface. Stark state calculations explained the experimental results by showing adiabatic evolution of neighbouring extreme blue- and red-shifted states.

The measurements with xenon Rydberg atoms at an Si(100) surface showed measurable surface ionisation signals at very low applied fields, compared to the surface ionisation for the Au(100) surface. This difference was attributed to the presence of stray fields at the surface [11,30]. Metastable ion bombardment removes the hydrogen used to pacify the silicon surface, so that significant adsorbate layers form. The localised stray fields caused by the adsorbate layer significantly changes the height of the barrier to surface ionisation and as such changes the atom-surface separation at which surface ionisation occurs, giving rise to signals at lower fields [4].

The ionisation of hydrogen Rydberg molecules (H_2) incident at a gold and aluminium surface has been investigated by Lloyd *et al* [13]. Rotational and vibrational excitation of the molecular ion provided additional degrees of freedom compared to an atomic system. The ion signal, as a result of the surface ionisation process, showed strong, repeatable, resonance features as a

function of applied field, attributed to avoided crossings in the Stark map, and evidence was seen for 'surface–induced rotational autoionisation'. Both gold and aluminium surfaces have conduction bands over the energy range of interest, so the materials do not influence the ionisation rate. However, significant changes to the surface ionisation profiles were seen when the surface roughness was comparable to the Rydberg orbital dimensions [31]. For H_2 and Xe [4] the Stark states affect the orientations of the Rydberg electron density with respect to the surface resulting in different surface ionisation profiles, but the presence of adiabatic behaviour at level crossings in the Stark map, leads to scrambling of the energy level on approaching a surface, such that the orientation was not preserved.

The ionisation of hydrogen Rydberg molecules at a doped silicon surface was investigated by Sashikesh *et al* [10]. Differences were seen in the behaviour of the resonant charge transfer process with the nature of the dopant and its concentration , demonstrating the surface sensitivity of the surface ionisation process. In this case the results were modelled by assuming a distribution of localised charges in the surface creating additional fields that depended on the dopant density. Additionally, the amount of ion signal for both n- and p-doped silicon surfaces was larger than for the corresponding surface ionisation measurements at a gold surface.

So *et al* investigated the surface ionisation of hydrogen atom Rydberg states at a gold surface [5] and surface ionisation profiles were measured across the k manifold. The profiles showed high level control over the orientation of the electron density in the presence of a surface was possible with hydrogen atoms, and that the k state had a large effect on the atom-surface separation

of surface ionisation. This was attributed to the presence of actual crossings in the Stark map of hydrogen atom, as described in section 1.2.1.

1.5 Surfaces with discrete energy levels

Previous experimental studies of Rydberg surface ionisation have primarily focused on metallic surfaces with a bulk continuum of states at the Rydberg energy range of interest. This leads to resonant charge transfer behaviour which is largely independent of the elemental composition of the surface. However, the work in this thesis demonstrates that Rydberg surface ionisation is also an effective probe of surfaces with a discrete ladder of image-state energy levels.

Ionisation dynamics of Rydberg states at these surfaces has a stronger n-dependence than for a bulk metal. Simplistically only Rydberg states degenerate with a discrete energy level can undergo resonant charge transfer and hence will surface ionise.

1.5.1 Projected band gap surfaces

The bulk 3D band structure of a crystal is described in terms of Bloch states, which are the electron wavefunctions within the bulk crystal lattice. At the surface, this three–dimensional band structure is projected onto the two–dimensional surface, and the periodic boundary conditions are terminated. The surface-localised states must exponentially decay into the vacuum. This change in boundary condition results in a new 'projected band structure' at the surface. There are 'surface resonances' which are degenerate bulk and

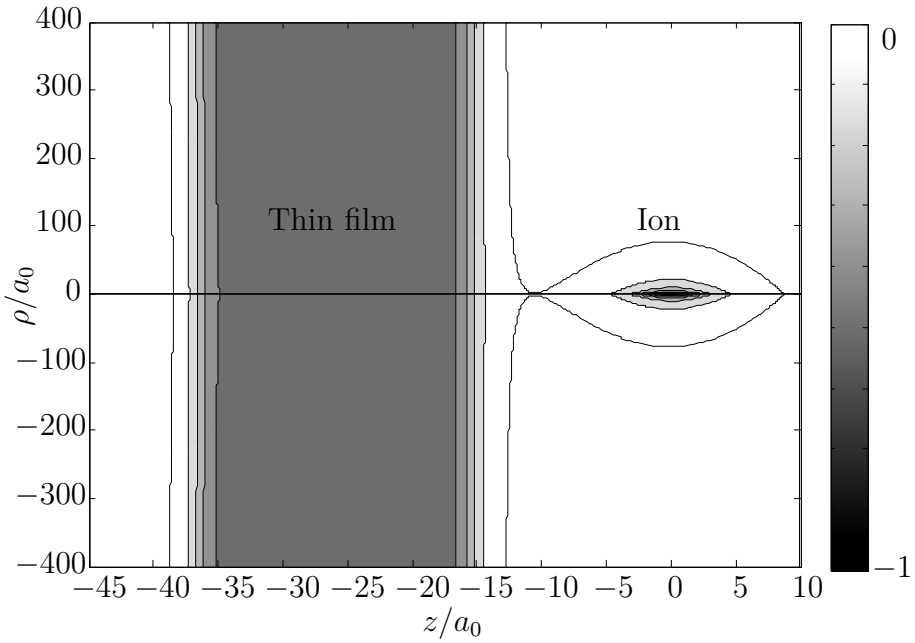

Figure 1.7: The total potential felt by a Rydberg electron in front of a thin film in the presence of the Rydberg ion. Along the surface normal, denoted by a black line, the thin film acts as a one dimensional quantum well, but it the other two dimensions there is no confinement of the potential.

surface states, and the purely surface-localised 'surface' states which are not degenerate with the bulk electronic band.

For free–electron metals, such as gold, the projected band structure is degenerate with the bulk metal and thus forms a continuum. However some metallic crystal planes, such as the Cu(100) and Cu(111), have a projected band gap at the surface as described in chapter 5. In such surfaces, within the energy range of the projected band gap, there are discrete surface states described in section 1.6.

1.5.2 Thin films

Thin metallic films can be described as a two-dimensional metallic continuum parallel to the surface, and a one-dimensional quantum well along the surface normal as shown in figure 1.7. Using angle-resolved photoemission it has been shown that this well yields discrete one dimensional particle-in-a-box style states along the surface normal [32]. The energies of these well-states and the spacings between neighbouring well-states decrease with increasing film thickness. The particle-in-a-box states couple to the two dimensional continuum, and form a stack of two-dimensional manifolds.

The surface electronic structure of a thin film is effectively a intermediate between a metal with a projected band, and one with a projected band gap, such that there are states at the surface, but they are discrete and well spaced in energy from each other. The exact energies of the discrete states are dependent on the substrate upon which the thin film is mounted. The band gap of the substrate provides the effective confinement in the system, such that electron density is confined within the thin film, and cannot leak into the support at energies degenerate to the substrate's band gap. In the case of the support being an insulator, the well depth is determined by the elemental crystal plane of the thin film. As the metal film increases in thickness this band structure tends towards the limit of the bulk metallic crystal plane's projected band structure.

1.5.3 Nanoparticles

A nanoparticle, with a diameter in the range of several nanometers, behaves as a three-dimensional spherical quantum well [33]. Fully confined discrete states are formed which are widely spaced in energy at small radii. For small nanoparticles the wavefunctions are atom–like and there is no coupling possible between neighbouring states.

As the dimensions of the nanoparticle increase, the energy gap between neighbouring states decreases as in the simplistic particle-in-a-spherical-box model, and ultimately the limit of a curved metallic surface is reached. The projected band structure of such a surface is different to its flat analogue, as a curved surface cannot result from cleavage of the bulk along a specified crystal plane. Additionally, as nanoparticles are typically grown from a cluster, the internal geometric and electronic metallic structure is often different to that of a bulk metallic surface, deposited under thermodynamic conditions.

Experimental preparation of nanoparticles on a surface often requires solvents and surfactants to produce a specific monolayer coverage on a support mount [34]. The presence of these additional components modifies the interaction potential between the nanoparticles and the surroundings, changing the energy and spatial distribution of any surface localised states. Additionally the substrate can act like an electron drain, such that the nanoparticle states are no longer fully confined.

1.6 Image-states

Image-states of surfaces are formed by the presence of an electron outside of a surface, degenerate with a band gap energy. The image-state wavefunction protrudes into the vacuum from the surface. In Rydberg-surface collisions, significant overlap between the Rydberg electron wavefunction and the image-state wavefunction is therefore possible as the Rydberg atom approaches the surface, allowing resonant charge transfer to occur. It is this dependence of the resonant charge transfer process on the energy and spatial distribution of the image-states, that allows Rydberg surface ionisation to be used as a probe of surface electronic structure.

1.6.1 The wavefunction of an electron at a surface

The electronic structure of the surface may differ significantly from the bulk due to the disruption of chemical bonds and structural reconstruction. Furthermore, the boundary conditions require the electronic wavefunction to decay exponentially into the vacuum in the direction perpendicular to the surface. For the Bloch states in the conduction band, the shift in energy due to the termination at the vacuum interface may be minimal. However the situation is different for an electron with energy in the band gap, for which the wavefunction must also decay towards the bulk of the metal. This leads to the existence of 'surface states' in which the wavefunction in the direction of the surface normal is confined to the surface region. Intrinsic surface states arise from the cleavage of the bulk metal (translational symmetry perpendicular to the surface is lost), and are localised mainly in the surface atomic layer [35,36],

with a wavefunction that decays exponentially towards the vacuum.

A second, but closely related type of surface state is the 'image-charge state'. An electron outside the surface at a distance z will give rise to an image-charge attractive potential of the form,

$$V(z) = -\frac{1}{4z}. \tag{1.23}$$

This one-dimensional long range Coulomb-like potential can in principle support an infinite series of bound states forming a Rydberg-type series where the usual nuclear charge Z is replaced with $Z/4$ and the energies are given by,

$$E_{\mathrm{IS}}(n_{\mathrm{img}}) = -\frac{1}{16}.\frac{1}{2(n_{\mathrm{img}}+a)^2} \tag{1.24}$$

here n_{img} is the image-state index and a is the quantum defect parameter for a given surface. Image-states arise from the Coulomb-like attractive image potential of an electron outside the metal surface and the surface barrier created by a gap of available bulk electronic states in the metal. The wavefunction of these image-states is localised mainly in the vacuum region of the interface. Such states are only observable in a band gap region as those degenerate with the conduction band are effectively mixed and broadened into the band [37]. There may also be intrinsic surface states in the band gap; whereas for image-states the wavefunction is almost entirely outside the metal, for surface states it is located at the surface with some significant penetration inside (similar to the difference between valence and Rydberg states of isolated molecules.)

In the direction parallel to the surface (for both surface and image-states)

the wavefunction will be very similar to the bulk metal states (except to the extent that it is perturbed by surface reconstruction) and kinetic energy is not quantised. The wavefunction in the direction parallel to the surface has the form,

$$\Psi_k = \Psi_{xy}(z)\exp(k_x x + k_y y) \tag{1.25}$$

where k_x is the momentum in the x direction and k_y is the momentum in the y direction. In the nearly free-electron model the states form bands with energy,

$$\epsilon(k) = E_{\mathrm{IS}} + \frac{\hbar^2}{2m}(k_x^2 + k_y^2) \tag{1.26}$$

where E_{IS} is the energy of the state with zero parallel momentum.

The corresponding one dimensional image-state wavefunctions along the surface normal are [38],

$$\Psi^{\mathrm{IS}}_{n_{\mathrm{img}}}(z) = zR_{n_{\mathrm{img}},l=0}(z/4), \tag{1.27}$$

where $R_{n_{\mathrm{img}},l=0}(z/4)$ is the normalised hydrogenic (s-wave) radial wavefunction [39] . Thus, image-states can extend far into the vacuum ($\langle z\rangle^{\mathrm{IS}}_{n_{\mathrm{img}}} = 6(n_{\mathrm{img}} + a)^2\mathrm{a}_0$), and in the context of the Rydberg-surface interaction there can be significant overlap with the Rydberg electronic wavefunction at a long distance from the surface. The resonance effects in charge transfer via image-states are expected to be particularly significant, especially when compared with the surface states.

However, for conducting metals such as gold, the image-states are degenerate with the conduction band and the strong coupling of the image-states

to the degenerate continuum means that the energies are extremely broad and the resonant states short lived. States of this kind are known as image resonances and electrons occupying these states have similar behaviours to those occupying ordinary crystal derived states. Thus it is only for band-gap semiconductors, or the projected band gap surfaces or nanostructures considered here, where such states are sufficiently narrow in energy and long lived to observe resonant charge transfer to a specific state.

For the thin metal films the surface electronic structure is complicated by the fact that both the quantum well and the image-state attraction potentially lead to discrete states. An electron outside this surface induces a discrete ladder of image-states which overlap with the well-states, forming a series of hybrid well-image states. Individual wavefunctions have varying amounts of well–state or image–state character, dependent on the energy matching of the two. As the film thickness increases, the well-states increase in number, and become closer together in energy, such that the hybrid well-image states have more well-state character and less image-state character. In the limit of a very thick film, the bulk band structure of the surface is reached, and the well-image states form image–state resonances. The wavefunctions of a thin film are discussed in more detail in section 6.1.

1.6.2 Experimental studies probing image-states

Surface and image charge states have been studied experimentally for a number of materials using various techniques including time-resolved photoemission (TRPES), inverse photoemission and scanning tunnelling spectroscopy.

Inverse photoemission or bremsstrahlung spectroscopy in the ultraviolet probes the surface with a beam of constant energy electrons. Photons are emitted as the electron transitions from a free-electron-like incoming state, into an unoccupied state above the Fermi level of the investigated sample [40]. D. Straub and F. J. Himpsel used inverse photoemission to measure the $n_{\mathrm{img}} = 1$ image-state energy for a series of metallic surfaces, changing both the element and the plane of the crystal [37]. The image-state energies determined, appeared to show no strong dependence on details of the surface, such as crystallographic orientation, corrugation, reconstruction, and material, within the experimental error of the method.

Two-photon photoemission spectroscopy (2PPE) improved the experimental accuracy and allowed more systematic measurement of the low n_{img} image-state energies. Giesen *et al.* used a short pulse resonant excitation from the metallic band to the image-state, to place an electron in the image-state [41]. Then a second photon of the same energy ionised the state and the kinetic energy of the emitted electron was measured using an electron analysis hemisphere [41]. Using this method it was shown that the binding energy does not depend on the material as long as the surface structure remains constant but, that the binding energy changes markedly with the crystal orientation. Using this method the $1 \leq n_{\mathrm{img}} \leq 3$ states of the Cu(100) surface were studied.

Höfer et al [42] used time-resolved 2PPE in combination with the coherent excitation of several quantum states to investigate the electron dynamics in higher order image-states of a Cu(100) surface. Using standard 2PPE the $1 \leq n_{\mathrm{img}} \leq 3$ states are resolvable, but to investigate the electron dynamics of

$n_{\text{img}} \geq 4$ a variant of quantum beat spectroscopy was required to determine the energies of the closely spaced image-states. A UV pump pulse was used to excite electrons into the image-states, and then probe IR pulses are used to emit the photoelectrons. The electron kinetic energy was measured in a electron energy analysis hemisphere. In the zero-delay configuration the $1 \leq n_{\text{img}} \leq 3$ image-states were directly resolvable, and the $n_{\text{img}} \geq 4$ formed a shoulder in the 2PPE spectrum.

For excitation of the $n_{\text{img}} \geq 4$ image-states, the bandwidth of the laser was comparable to the energy spacings of the image-states, such that neighbouring states were excited coherently. Oscillations in the photoelectron yield as a function of pump-probe delay were seen as population flowed between the different excited image-state wavefunctions. The beating period is the difference between the neighbouring image-state energies. The limitation of this method is that higher order image-states are closer in energy and thus more states are coherently excited within the bandwidth of the laser, making the analysis of the quantum beats increasingly more complex.

Other studies have used projectiles to determine the resonant charge transfer behaviour at projected band gap surfaces [43]. However none of these methods have had the tunability required to determine the energy of individual image-states, and have instead confirmed the susceptibility of the resonant charge transfer process to the presence of a projected band gap.

Further experimental studies have used 2PPE to probe the change in binding energy and dispersion of image-state energy levels for a projected band gap metal with an adsorbed dielectric film [44]. Very thin metallic films have hybrid well-image states which have not been measured directly

before. However a variety of photoemission experiments have probed the pure quantum well-states within the thin films [32, 45, 46], determining their energy and spatial distribution [47].

Scanning tunnelling microscopy (STM) and spectroscopy (STS) have been used to investigate the quantum dynamics in the two dimensional image-states of Cu(100) [48]. The energies of the image-states as a function of external field were determined by application of a large bias voltage to the surface. However, this led to the image-state energies moving above the vacuum level, and the electrons only remained bound due to the presence of the scanning probe tip and crystal. Scattering of the electrons bound in an image-state was seen to occur at point defects and step edges, creating modulations in the local density of states through quantum interference. This allowed the dynamics of the states, with some momentum parallel to the surface locally, to be studied. The results suggested that the tip-induced Stark shift of the image-states does not affect the motion of electrons parallel to the surface.

It is shown in this thesis that probing these high-lying image-states with Rydberg atoms results in individual resolution of image-states. Through these experiments it is possible to learn both about resonant charge transfer at a surface and about the image-states themselves.

1.7 Thesis outline

This thesis aims to extend previous Rydberg surface ionisation experiments to surfaces with discrete high-lying image-states, using a combination of theoretical and experimental methods. In chapter 2 the wavepacket prop-

agation method used throughout this thesis is outlined. In chapter 3 the results of several wavepacket propagation studies are described. The velocity dependence of the resonance effects at a projected band gap surface provide an introduction to wavepacket calculations at a flat metal surface, before a wavepacket study to understand resonance-enhanced charge transfer at an isolated nanoparticle provides a model for a fully confined system. In chapter 4 the experimental setup of the Rydberg-surface ionisation experiment and the surface analysis facilities are outlined. In chapter 5 the results of an experimental study investigating surface ionisation of hydrogen Rydberg atoms at a projected band gap surface are presented. Experimental results for the surface ionisation of hydrogen Rydberg atoms at a series of metallic thin films are shown in chapter 6. Finally, in chapter 7 the findings of the thesis are summarised and suggestions for future work are made.

Chapter 2

Theoretical methods

Several different theoretical methods have been used to investigate surface ionisation of Rydberg atoms at metallic structures [6, 8, 21, 22, 29, 49–60]. In this thesis, a wavepacket propagation method is described to capture the dynamics of the surface ionisation process [6, 58–60]. Such a method has previously been used to model hydrogen Rydberg atoms incident at a flat, metallic surface [6]. Here it is extended to model the surface ionisation dynamics of hydrogen Rydberg atoms at metallic structures with confined potentials.

2.1 Theoretical Approaches

Some previous studies have used perturbation theory to model the long range perturbation of atomic Rydberg states by a metallic surface [49, 50]. Typically these studies investigated the interaction of an atomic alkali–metal Rydberg state with metallic surfaces. They used a perturbing Hamiltonian based on

the classical image-charge potentials, described in equation 1.17, to generate first order shifts in the atomic energies [50]. The energies of the states are very dependent on the exact form of the potential especially at small atom–surface separations meaning that this approach is inaccurate at atom-surface separations where ionisation occurs.

Perturbation theory has been used to more accurately model the potential at small separations, but very high order corrections to the image-charge potential are required. Ganesan and Taylor [21] used a full matrix diagonalisation on the $n = 20$ Rydberg H atom potential surface and an eighth-order polynomial expansion was required to accurately model the potential at atom-surface separations larger than $5.25n^2$. This is still significantly larger than the $D = 3.8n^2$ where ionisation is expected to become significant for surface oriented states [5]. However the major limitation to perturbation theory for the study of ionisation dynamics is that it has the wrong outgoing boundary conditions and as such can only treat bound states.

Nordlander has successfully applied the complex–scaling method to extract the energies and lifetimes of resonant states of Rydberg atoms in front of a metal surface [8, 29, 51–53]. The complex scaling method involves the transformation of the Hamiltonian into a non-Hermitian Hamiltonian, so that a bound–state boundary condition is imposed on the wavefunctions of the resonant state in the continuum. Complex eigenvalues can then be generated if a large complex angle and a square-intergratable basis function are used, where the real part represents the energies and the imaginary part the lifetimes. The computational time for matrix diagonalisation scales as N^3 where N is the number of grid points, whereas matrix multiplication scales

with N^2. The complex scaling method utilises a matrix diagonalisation at each atom-surface separation, so that diagonalising the complex non-Hermitian matrix is computationally demanding.

Many other theoretical approaches to the surface ionisation problem have been used previously. These include classical and semi-classical trajectory approaches using over-the-barrier calculations [55] and close-orbit theory [54], respectively. Coupled angular mode scattering (CAM) calculations [22,56] and implementation of the wide-band diabatic dynamics approach (WBDD) [57] have also been carried out.

A wave packet propagation (WPP) approach has been used in several previous studies into charge transfer between Rydberg atoms and metal surfaces [6, 58–60]. This approach follows the quantum mechanical evolution of the Rydberg electron wavepacket as the atom approaches a surface and allows the dynamics of a system to be followed in real time. The WPP approach includes all dynamical aspects of the charge transfer process, including diabatic effects at the avoided crossings. Another advantage is the reduced computational time, as at each time step the wavepacket is propagated by simple matrix multiplication (computational time for an $N \times N$ matrix is $\propto N^2$) whereas time-independent approaches, such as complex scaling, require a matrix diagonalisation at each atom-surface separation (computational time $\propto N^3$). This thesis applies WPP to the ionisation of Rydberg hydrogen atoms at a projected band gap surface and a nanoparticle.

2.2 Grid based methods

For an $N \times N$ matrix the computational time for matrix multiplication scales as N^2, whereas for matrix diagonalisation it scales as N^3. Therefore calculations involving a large number (N) of basis functions can quickly become very computationally demanding. Modelling the surface ionisation problem using a wavepacket propagation (WPP) method, as described in section 2.3, requires a large number of basis functions. This is even more significant when the surface ionisation problem includes high principal quantum number Rydberg states, molecular Rydberg states, large atom surface distances or three-dimensions. Therefore discrete variable representations (DVRs) [61] and other grid based methods are employed to minimise computational time.

2.2.1 DVR vs FBR

The electronic wavefunction in this thesis is described by a linear combination of an N-dimensional radial and angular coordinate product basis. A Finite Basis Representation (FBR) is a set of N global continuous basis functions. Typically, it is difficult to evaluate the potential energy matrix $\mathbf{V}$ whilst using a FBR and a numerical method is used to approximate the integrals that form matrix elements. Often this numerical method is a Gaussian quadrature rule.

A Discrete Variable Representation (DVR) first described by Lill, Parker and Light [62], transforms the FBR $\{\chi(x_j)\}_N$ into N orthonormal basis functions $\{\varphi(x_j)\}_N$, each of which is localised about one point in coordinate space. The kinetic energy matrix $\mathbf{T}$ within the DVR is easily integrated

analytically. The potential energy matrix $\mathbf{V}$ is diagonal and the matrix elements are given by the potential at the DVR points. This results in high efficiency for calculations as it is no longer necessary to calculate Hamiltonian matrix elements from first principles. The resulting Hamiltonian matrix $\mathbf{H}$ is sparse, making Hamiltonian-vector multiplication very fast and reducing computational time. For multidimensional systems, such as the surface ionisation problem, direct-product DVRs can be implemented.

The FBR and DVR are isomorphic, and, mathematically, the matrix elements of the DVR and the FBR are related by a unitary transform. For a generic operator $\widehat{O}$, the matrix elements in the DVR, $\mathbf{O^{DVR}}$, and FBR, $\mathbf{O^{FBR}}$, are related by a the application of the FBR/DVR transformation matrix $\mathbf{U}$:

$$\mathbf{O^{DVR}} = \mathbf{U}^{\dagger}\mathbf{O^{FBR}}\mathbf{U} \tag{2.1}$$

Linear combinations of the N basis functions $\{\varphi(x_j)\}_N$ form the elements of the transformation matrix U. The main properties of DVRs and their basis functions are described in the following sub-sections, which detail the use of DVRs in this thesis. More detailed analysis can be found in a review by Carrington and Light [61].

2.2.2 Legendre basis

The Legendre basis DVR is used in this thesis to treat the angular degrees of freedom in the electronic wavefunction. The FBR basis set is the normalised Legendre polynomials $P_l^{m_l=0}(\cos\theta)$ which are the eigenfunctions of the angular

momentum operator with a magnetic quantum number $m_l = 0$,

$$\begin{aligned} \chi_j(\cos\theta) = \widetilde{P}_{j-1}(\cos\theta) &= A_j P_{j-1}(\cos\theta) \quad \text{where } j = 1, ..., N \\ A_j &= \sqrt{\frac{2(j-1)+1}{2}} \end{aligned} \tag{2.2}$$

Throughout this thesis, H atom $m_l = 0$ Rydberg states are investigated. A_j is the normalisation constant for the polynomial $P_{j-1}(\cos\theta)$ with $m_l = 0$. The $m_l = 0$ Legendre polynomials are related to the spherical harmonics $Y_{m_l,l}(\theta, \phi)$ for the special case of $m_l = 0$ by:

$$Y_l(\theta, \phi) = (2\pi)^{-\frac{1}{2}} P_l(\cos\theta) \tag{2.3}$$

The surface potential and the electric field potential combine to form the perturbing potential $V_{\text{perturb}}(r, \theta)$, as described in section 2.17. This perturbing potential is diagonal in the Legendre DVR, but the centrifugal potential V_{cent}, as described in equation 2.18, is diagonal in the Legendre FBR used in the initial wavefunction and described in section 2.3.1. Therefore both the Legendre DVR and FBR are utilised in the calculations in this thesis.

2.2.3 CWDVR

Many DVRs based on orthogonal polynomials or trigonometric functions have problems dealing with the Coulomb potential singularity in the radial coordinate and require regularisation of the potential near the origin. However, the Coulomb-wave discrete variable representation (CWDVR) has the necessary properties to treat this singularity without regularisation. Dunseath *et al.* [63]

proposed the CWDVR to deal with problems involving the Coulomb potential and it has been implemented in several Rydberg surface ionisation studies since [6, 64].

The position of the grid points are defined as the positive zeros of the positive energy Coulomb reference function $v(r)$, which is a solution to the radial Schrödinger equation for the hydrogen atom,

$$\left[\frac{d^2}{dr^2} - \frac{l(l+1)}{r^2} + \frac{2Z}{r} + 2E\right] v(r) = 0 \tag{2.4}$$

with angular momentum quantum number $l = 0$, and the positive energy $E \geq 0$. The grid points have a non-uniform distribution. Near the Coulomb singularity there is a high grid point concentration but at large r there is a low concentration of almost regularly spaced grid points. The distribution of the grid points is altered by the parameters $\kappa = \sqrt{2E}$ and Z. κ controls the separation of grid points at large distances and Z controls the concentration near the Coulomb singularity [63]. The radial coordinate for the surface ionisation problem is well-described by the CWDVR, as near the Coulomb singularity the wavefunction is bound by the Coulomb potential, but at large distances after ionisation it behaves as a free wave.

In this thesis the Coulomb wavefunctions and their derivatives are computed by the COULFG subroutine of Barnett [65]. The derivative is required to calculate the quadrature weights. The zeros of the Coulomb wavefunction correspond to the grid points, and are determined by Newton-Raphson iteration [66].

The kinetic energy matrix elements T_{ij}^{DVR} in the CWDVR are given by a

simple analytical expression, as is a general feature of DVRs. The potential energy matrix elements V_{ij}^{DVR} are determined from the value of the potential at the radial grid points, and overall the matrix is diagonal ,

$$T_{ij}^{\mathrm{CWDVR}} = -\delta_{ij}\frac{W(r)}{6} + (1-\delta_{ij})\frac{1}{(r_i - r_j)^2} \tag{2.5}$$

$$V_{ij}^{\mathrm{CWDVR}} = \delta_{ij}V(r_i) \tag{2.6}$$

Where, $W(r) = (\kappa^2 + \frac{2Z}{r})$. The CWDVR is used throughout this thesis as the radial part of the electronic wavefunction during propagation.

2.2.4 Regularised Lagrange-Laguerre grid

The regularised Lagrange-Laguerre mesh is used to describe the radial coordinate during the initial diagonalisation which establishes the initial wavefunction at a chosen distance from the surface. For time-independent calculations, such as the initial diagonalisation, the roughly uniform grid-point distribution at large r of the CWDVR is not required, however a high concentration of grid points near the origin is still needed. Since matrix diagonalisation scales with N^3 it is computationally favourable to use a minimal number of basis functions and so the regularised Lagrange-Laguerre mesh is used in place of the CWDVR.

The basis functions of the regularised Lagrange-Laguerre mesh are given by,

$$\tilde{f}_i(x) = \frac{x}{x_i}f_i(x) = (-1)^i x_i^{-\frac{1}{2}}\frac{xL_N(x)}{x - x_i}e^{-\frac{x}{2}} \tag{2.7}$$

where $f_i(x)$ are the basis functions of the Lagrange-Laguerre mesh, N_x is the

number basis functions and x_i is the position of the ith root of the Laguerre polynomial L_N. N gives the number of DVR grid points, and x_i are the unregularised DVR grid points.

The kinetic energy matrix in the Lagrange-Laguerre mesh is given by,

$$T_{ii}^{\text{Lag}-\text{Lag}} = \frac{1}{24x_i^2}[4 + (4N+2)x_i - x_i^2] \tag{2.8}$$

$$T_{ij}^{\text{Lag}-\text{Lag}} = \frac{(-1)^{(i-j)}x_i + x_j}{2(x_i x_j)^{\frac{-1}{2}}(x_i - x_j)^2} \tag{2.9}$$

$$V_{ij}^{\text{Lag}-\text{Lag}} = \delta_{ij}V(x_i) \tag{2.10}$$

where V_{ij}^{DVR} is diagonal.

Regularisation of the Lagrange-Laguerre mesh allows it to accurately represent the singularities in the Coulomb ($\propto r^{-1}$) and centrifugal potentials ($\propto r^{-2}$) at the Gauss approximation [67]. The regularised Lagrange-Laguerre mesh has been utilised in many theoretical studies such as the generation of Morse potential eigenvalues [68], hydrogen bound energy states [67] and calculations assessing molecular hydrogen in a magnetic field [69]. The most relevant examples, however, are those where it is used, as in this thesis, as the radial coordinate of the initial wavefunction in a Rydberg surface ionisation WPP calculation [6, 64].

2.2.5 Sinc DVR

The Sinc DVR $\{\varphi(x_p)\}_N$, also known as the Fourier DVR, yields an equally spaced grid. The N sinc DVR functions for a one dimensional grid are of the

form [70],

$$\varphi_p(x) = \Delta^{-\frac{1}{2}} \text{sinc}\left(\pi\left[\frac{x}{\Delta} - p\right]\right) \tag{2.11}$$

$$p = 1 \rightarrow N \tag{2.12}$$

$$\text{sinc } x = \frac{\sin x}{x} \tag{2.13}$$

The points of the grid are given by $x_p = p\Delta$ and the weights of the points are $w_p = \Delta$. The kinetic energy matrix elements are [70, 71]:

$$T_{ij} = \begin{cases} \frac{\pi^2}{6\Delta^2} & i = j \\ \frac{(-1)^{(i-j)}}{\Delta^2(i-j)^2} & i \neq j \end{cases} \tag{2.14}$$

Sinc DVRs are useful for dealing with problems where the solution resembles the sinusoidal FBR. In this thesis, the sinc DVR is used to determine the energies and wavefunctions of the thin film well-image-states described in section 6.1.

2.3 Wavepacket Propagation approach

The time evolution of the electronic wavefunction of the Rydberg atom under the influence of the time–dependent potential is governed by the time-dependent Schrödinger equation (TDSE),

$$i\frac{d}{dt}\Psi(t) = \widehat{H}\Psi(t) \tag{2.15}$$

Generally $\Psi(t)$ is the time dependent wavefunction and $\widehat{H} = \widehat{T} + \widehat{V}$ is the Hamiltonian operator, containing the potential $\widehat{V}$ and kinetic energy $\widehat{T}$ operators. The solution of the TDSE is,

$$\Psi(t + \Delta t) = e^{-i\widehat{H}\Delta t}\Psi(t) \tag{2.16}$$

where $\Psi(t)$ is the initial wavefunction and application of the propagator $e^{-i\widehat{H}\Delta t}$ generates the subsequent wavefunction $\Psi(t + \Delta t)$ at the later time of $(t + \Delta t)$. In the WPP approach the matrix elements of the propagator are discretised onto DVRs that describe the radial and angular degrees of freedom within the electronic wavefunction as described in section 2.2. Time evolution of the initial wavefunction on these grids occurs by propagating with timestep Δt. The following subsections describe the implementation of the WPP approach used in this thesis.

2.3.1 Initial Wavefunction

The initial wavefunction is discretised in a two dimensional grid (r, θ) as shown in figure 2.1, with an angular and radial coordinate. As there is cylindrical symmetry about the surface normal, the physical three-dimensional system can be collapsed onto this theoretical two-dimensional system to simplify the calculations. As explained in section 2.2.2, the angular coordinate of the initial wavefunction is described by the Legendre FBR/DVR with n_θ basis functions and grid points. The initial diagonalisation is carried out with the radial coordinate described by the regularised Lagrange-Laguerre grid with N_x basis functions $\{\widetilde{f}_j(x)\}_{j=1}^{N_x}$, while during the propagation the radial

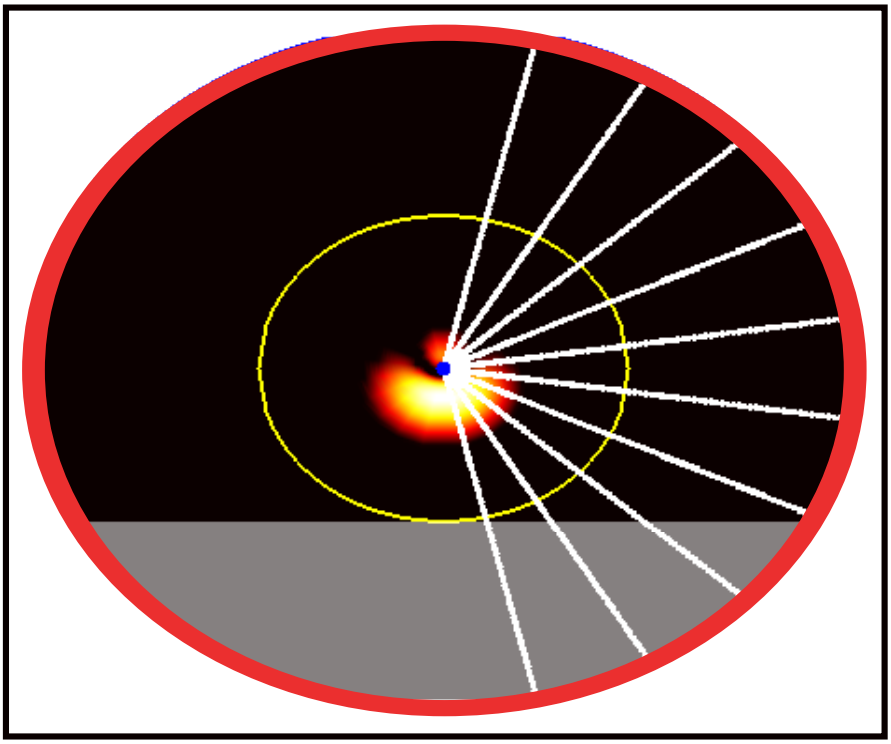

Figure 2.1: A schematic illustration of the initial $k = -1$, $n = 2$ hydrogen electronic wavepacket in orange and yellow; the ion is in blue, the absorbing boundary in yellow, the surface in grey and the edge of the grid in red. The CWDVR radial and angular grid points are shown in white, however they appear as lines due to the dense nature of the radial points. Note a comparably sparse grid has been used here for clarity, and therefore the wavepacket is poorly resolved.

coordinate of the electronic wavefunction is represented by the CWDVR with n_r basis functions, $\{f_v(r)\}_{v=1}^{n_r}$, as described below.

The initial wavefunction is computed by diagonalisation of the full Hamiltonian of the Rydberg atom before propagation. The full Hamiltonian of the

Rydberg atom is,

$$\widehat{H} = \widehat{T}(r) + \widehat{V}_{\text{hydrogen}}(r) + \widehat{V}_{\text{perturb}}(r,\theta) \tag{2.17}$$

$$\widehat{V}_{\text{hydrogen}}(r) = \widehat{V}_{\text{centrifugal}}(r) + \widehat{V}_{\text{Coulomb}}(r) = \frac{l(l+1)}{2r^2} - \frac{1}{r} \tag{2.18}$$

$$\widehat{V}_{\text{perturb}}(r,\theta) = \widehat{V}_{\text{Stark}}(r,\theta) + \widehat{V}_{\text{surface}}(r,\theta) \tag{2.19}$$

where $\widehat{T}(r)$ is the kinetic energy operator and $\widehat{V}_{\text{hydrogen}}(r)$ is the atomic potential energy operator that includes the centrifugal potential operator and the Coulombic potential operator which are caused by the interaction of the Rydberg electron and the ion within the Rydberg atom. $\widehat{V}_{\text{hydrogen}}(r)$ is solely dependent on the radial coordinate r. $\widehat{V}_{\text{surface}}(r,\theta)$ is the cylindrically symmetric surface potential introduced in Sec. 1.3.2. This term is dependent on the radial coordinate r and the angular coordinate θ.

The matrix elements of the kinetic energy operator are given by (Eqn. 2.6) in the CWDVR. The time independent potential energy matrix $\widehat{V}_{\text{Hydrogen}}$ (Eqn. 2.18) in the radial CWDVR or Lagrange-Laguerre DVR/FBR is diagonal. For a given Legendre FBR basis with angular momentum quantum number l the matrix elements are determined by the values of the potential at the radial grid points. However, while the time-dependent potential energy matrix V_{perturb}, from equation 2.19, which depends on both the angular and radial coordinate, is still diagonal in the CWDVR, it is only diagonal in the Legendre DVR but not in the angular Legendre FBR, so, a FBR/DVR transformation is required as described by equation 2.1,

$$\mathbf{V}^{\mathbf{FBR}}_{\text{perturb}} = \mathbf{U}\mathbf{V}^{\mathbf{DVR}}_{\text{perturb}}\mathbf{U}^{\dagger} \tag{2.20}$$

$\mathbf{U}$ is the Legendre FBR/DVR transformation matrix and $\mathbf{V}^{\mathbf{DVR}}_{\text{perturb}}$ is the diagonal matrix with elements evaluated at r and θ.

Full diagonalisation of the Hamiltonian (Eqn. 2.19) leads to the eigenvalues and eigenfunctions of the Rydberg state at $t = 0$ and $D = D_0$, where D is the atom-surface separation. In the Lagrange-Laguerre basis in the radial dimensions the eigenfunction is,

$$\psi_{nl}(r) = \sum_j \widetilde{c}_j^{nl} \widetilde{f}_j(r) \tag{2.21}$$

where $\widetilde{c}_j^{nl}$ is the time-dependent expansion coefficient. This is then projected onto the CWDVR basis before propagation by operation of the projection operator for the CWDVR basis $\widehat{P}$ using the collocation property of DVR's [72] which leads to,

$$\widehat{P}\,|\psi_{nl}\rangle = \sum_v |v\rangle \langle v\,|\psi_{nl}\rangle \tag{2.22}$$

$$\sum_v |v\rangle \langle v\,|\psi_{nl}\rangle = \sum_v |v\rangle\, w_v \psi_{nl}(r_v) = \sum_v |v\rangle\, w_v^{\frac{1}{2}} \widetilde{c}_j^{nl} \widehat{f}_j(r_v) \tag{2.23}$$

where $|v\rangle$ are the CWDVR grids points defined in equation 2.4. Therefore, the wavefunction in the CWDVR basis is given by the value of the wavefunction in the Lagrange-Laguerre grid at the CWDVR points multiplied by the square root of the weights associated with those points.

The initial diagonalisation is carried out at large atom-surface separation to ensure that the Rydberg atom state is bound before it is propagated. The atom surface separation has to be large enough to ensure that negligible surface ionisation occurs early in the propagation, and that the contribution

from the surface potential is too small to cause crossings between states. Experimentally, it has been seen that ionisation is significant at $D \leq 5n^2a_0$, so the initial diagonalisations in this thesis are carried out at $D_0 = 10n^2a_0$.

2.3.2 Modelling the surface potential

As described in section 1.3.2 the classical image-charge model provides a simple representation of the various contributions to the surface potential. However, the classical terms do not adhere to the internal boundary conditions of the metallic surface. Previous studies have focused on flat metallic surfaces, and represented the surface by a semi-infinite slab of jellium.

2.3.2.1 The Jellium model

Jellium is the archetypal model for a free-electron metal. The Jenning-Jones one-electron pseudopotential [23] interpolates from the bulk metal value to the asymptotic potential given by the image-charge model outside the metal. The electron–image electron interaction is given by,

$$V_{ee} = \begin{cases} \frac{-1+\exp(-\beta((z+D)-z_{im}))}{4((z+D)-z_{im})} & \text{if}(z+D) \geq z_{im} \\ \\ \frac{V_0}{A\exp(B((z+D)-z_{im}))+1} & \text{otherwise} \end{cases}$$

with $A = -1 - 4V_0/\beta$ and $B = -2V_0/A$. V_0 is the element-dependent bulk metal parameter i.e. the maximum well depth, z_{im} is the location of the image plane, D is the atom-surface separation, z is the electron's coordinate in the atom frame, as shown in figure 1.3, and β is an interpolation parameter.

The Jellium model is useful as it is straightforward to implement and by

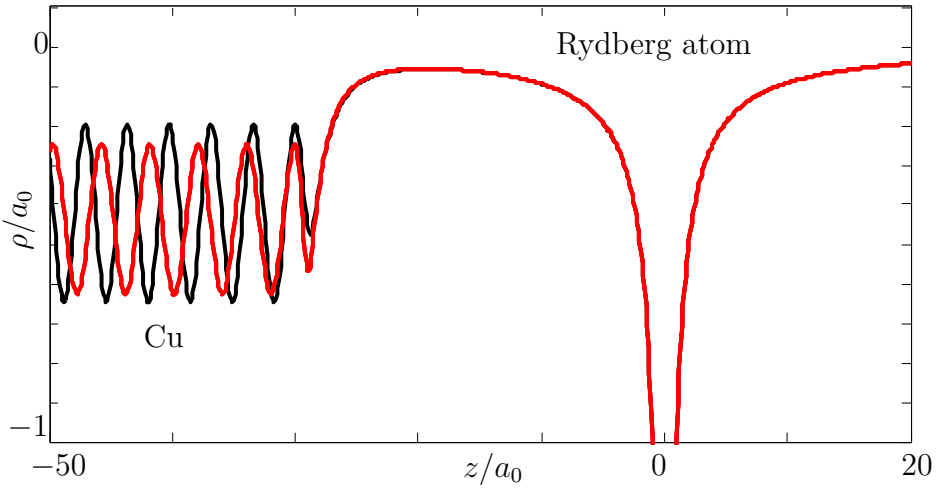

Figure 2.2: The total potential experienced by the Rydberg electron in front of a Cu(100) surface in black and a Cu(111) surface in red, and in the presence of the ion at $z = 0a_0$ calculated using the Chulkov potential described below.

varying the z_0, V_0 and β parameters a wide variety of surfaces can be studied. However, it models the metal as a sea of electrons moving in a background of uniform positive charge which neglects to account for the location of metal ions. The evaluation of some surface properties can be improved by modifying the A and B parameters to be crystal-plane dependent [23], but ultimately a corrugated potential is required to accurately treat these different crystal planes.

2.3.2.2 The Chulkov pseudopotential for Cu(111) and Cu(100)

For surfaces with a projected band gap such as Cu(100) and Cu(111), the energetic location of the projected band gap is sensitive to the arrangement of atoms at the surface. Therefore, a corrugated potential has to be used

	a_s (a.u.)	A_{10} (eV)	A_1 (eV)	A_2 (eV)	β (a_0^{-1})
Cu(111)	3.94	-11.895	5.14	4.3279	2.9416
Cu(100)	3.415	-11.480	6.10	3.7820	2.5390

Table 2.1: Values of the parameters used in the one-electron pseudo-potential given by Eq. 2.24 for the Cu(111) and Cu(100) surface [24].

such as the Chulkov one-electron pseudopotential [24],

$$\begin{aligned} V_{ee} &= V_1 + V_2 + V_3 + V_4 \\ V_1 &= A_{10} + A_1 \cos\left(\tfrac{2\pi}{a_s} z\right) && zz < 0 \\ V_2 &= -A_{20} + A_2 \cos(\beta z) && 0 < zz < z_1 \\ V_3 &= -A_3 \exp(-\alpha(zz - z_1)) && z_1 < zz < z_{\text{im}} \\ V_4 &= \tfrac{\exp(-\lambda(zz - z_{\text{im}}))-1}{4(zz - z_{\text{im}})} && z_{\text{im}} < zz \end{aligned} \tag{2.24}$$

where a_{s} is the copper interlayer spacing, and A_1, A_2, A_{10} and β are the surface-dependent parameters. The potential is defined in terms of $zz = z + D$, such that the surface is at $zz = 0$. This has been used previously to model the projected band gap of Cu(111) and Cu(100) in the direction normal to the surface, while an electron is allowed to move freely parallel to the surface [38, 58, 73, 74] . The total potential is plotted in figure 2.2. The values for the Cu(111) and Cu(100) surfaces are given in Table 2.1. The remaining parameters in Eq. 2.24 are determined by requiring the potential and its first derivative to be continuous,

$$\begin{aligned} A_{20} &= A_2 - A_{10} - A_1 & A_3 &= -A_{20} - \tfrac{A_2}{\sqrt{2}} \\ z_1 &= \tfrac{5\pi}{4\beta} & \alpha &= \tfrac{A_2 \beta}{A_3} \sin(z_1 \beta) \\ \lambda &= 2\alpha & z_{\text{im}} &= z_1 - \tfrac{1}{\alpha} \ln\left(\tfrac{-\alpha}{2A_3}\right). \end{aligned} \tag{2.25}$$

The bulk potential, and the width and position of the projected band gap, are described by V_1 in Eq. 2.24, while the metal-vacuum interpolation potential and the energies of the surface and image-states are described by V_2 and V_3. The V_4 term describes the long range image-potential.

2.3.2.3 The thin film potential

Metallic thin films are modelled as a jellium slab of finite thickness along the surface normal, with infinite size in the dimensions perpendicular to the z axis as shown in figure 1.7. Along the surface normal the thin film behaves as a one-dimensional quantum well of thickness T_{z}.

The form of the electron–image electron interaction V_{ee} and the electron–image proton interaction V_{ep} employed in this chapter are defined in terms of the electron position relative to the surface $zz = |z + T_z/2 + D| - T_z/2$,

$$V_{ee}(zz, d) = \begin{cases} \frac{-1+\exp[-\beta(zz-z_0)]}{4(zz-z_0)} & \text{if } zz > z_{im} \\ \frac{V_0}{A\exp[B(zz-z_0)]+1} & \text{otherwise} \end{cases} \tag{2.26}$$

$$\text{with} \quad A = -1 - 4V_0/\lambda, \quad B = -2V_0/A.$$

where outside of the thin film $zz > 0$ and inside the film $zz < 0$. The form of V_{ee} for the thin film is the same as for the one dimensional well as the image-charge potential is dependent only on the separation between the electron and its image-charge. This form of the potential was used in the calculations of Usman *et al* [9].

However the V_{ep} term is dependent on the separation between the electron

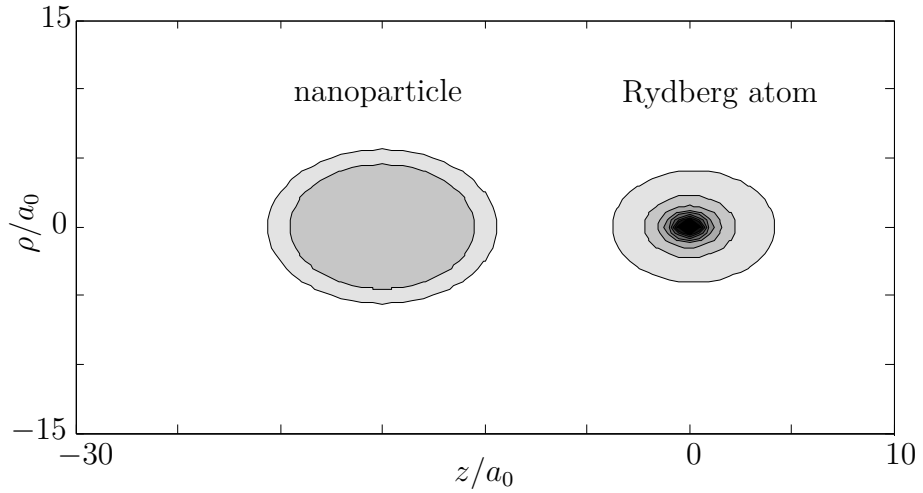

Figure 2.3: The total potential experianced by the Rydberg electron in front of a small nanoparticle and in the prescence of the ion at $z = 0a_0$.

and the proton's image-charge, which depends on both the separation between the ion and the electron , ρ, as well as zz,

$$V_{ep}(zz,\rho) = \begin{cases} \frac{1}{\sqrt{(D+|zz|)^2+\rho^2}} & \text{if } zz > 0 \\ \frac{1}{\sqrt{D^2+\rho^2}} & \text{otherwise} \end{cases} \tag{2.27}$$

where $\rho = \sqrt{r^2 - z^2}$, as shown in figure 1.3.

2.3.2.4 The nanoparticle potential

The image-states of small metallic clusters have been modelled by Rinke *et al.* [33] and their potential is used in this thesis. Like the flat surface case, the explicit form of the potential used to model nanoparticles in this thesis is based on the classical image-charge model. However the image-charges of an isolated-sphere are located at the inverse point of the sphere. This complicates the potential as $V_{ep} \neq V_{pe}$ and V_{pp} does not cancel in the expansion of the full

Rydberg-sphere interaction as would be the case for a flat metal surface. The electron–image electron potential of a metal cluster, or very small nanoparticle is,

$$V_{ee} = \begin{cases} V_{\text{image}} & r > R + d \\ p(r) & R - d < r < R + d \\ V_{\text{bulk}} & r < R - d \end{cases}$$

where r is the distance between the electron and the nanoparticle centre, R is the radius of the nanoparticle and d is an interpolation region such that $V_{\text{image}}(R + d) > V_{\text{bulk}}(R - d)$. The image potential and the bulk metallic sphere potential are approximated as,

$$V_{\text{image}} \approx \frac{-R^3}{2r^2(r^2 - R^2)} \tag{2.28}$$

$$V_{\text{bulk}} = \frac{V_0}{A \exp(B(r - R) + 1)} \tag{2.29}$$

where A and B are the jellium parameters for the bulk metal surface of choice [23]. An interpolation function, $p(r)$, ensures that there are no discontinuities in the potential. The total potential experienced by the Rydberg electron is plotted in figure 2.3.

For larger nanoparticles, such as the ones that have previously been investigated experimentally e.g. if $R = 10$nm, then the surface will behave more as a curved surface than a spherically confined system. In the limit of $R \to \infty$ then $\lim_{R\to\infty} V_{\text{bulk}} \to V_0$ where V_0 is the internal potential for the bulk free-electron metal in question. In effect, within this model, at large radii the nanoparticle forms a continuum of states, and behaves as a curved

semi-infinite slab of jellium.

When modelling a confined potential like this, the edge of the DVR grid must be located sufficiently far from the nanoparticle surface such that it has no effect. The resulting large grid leads to the nanoparticle calculations being computationally very expensive, and restricts the calculations to low principal quantum number Rydberg atoms and very small nanoparticles.

No attempt has been made in the work presented in this thesis to account for the substrate onto which the nanoparticles are deposited, or the presence of surfactants and solvents on the surface due to the deposition process. Finally only the interaction between a single nanoparticle and a single Rydberg atom is considered, i.e. only the one-electron process is investigated and it is possible significant further effects are observed experimentally based on non-monolayer coverage, clustering of nanoparticles or glancing interactions.

2.3.3 Absorbing Boundary

For all the potentials used here the radial coordinate r which defines the CWDVR grid is infinitely large, however, in reality, the DVR grid employed is finite and so has to be truncated at a specific radial point designated $r_{\max}$. The presence of a non-physical boundary may result in wavefunction reflection at the edge of the grid, leading to interference patterns between incoming and outgoing waves and non-physical effects within the wave packet and the ionisation dynamics. To ensure that the electron wavefunction behaves as a purely outgoing wave, and to remove these reflections, the Manolopoulos transmission-free absorbing potential $-i\epsilon(r)$ is included in the Hamiltonian

[75],

$$\mathbf{H} = \mathbf{H} - i\epsilon(r) \tag{2.30}$$

In this equation $-i\epsilon(r)$ is a diagonal matrix with the elements $-i\epsilon(r)h(r-r_{\text{abs}})$ where r_{abs} is the lower bound of the absorbing region and $h(f(r))$ is the Heaviside step function. The complex potential is,

$$-i\epsilon(r) = -i\frac{y(x)}{2}\left(\frac{2\pi}{\Delta r}\right)^2 \quad \text{where } x = \tfrac{c(r-r_{\text{abs}})}{\Delta r} \tag{2.31}$$

The approximate form of $y(x)$ is [76],

$$y(x) = \frac{4}{(c-x)^2} + \frac{4}{(c+x)^2} - \frac{8}{c^2} \tag{2.32}$$

The width of the absorbing region is $\Delta r = r - r_{\text{abs}}$ and the constant $c \approx 2.62206$ [75]. The Manolopoulos absorbing potential is totally transmission-free and is dependent only on Δr, making it easy to implement. The reflection properties improve as Δr is increased [75]. The width of the absorbing boundary are typically chosen to correspond to the de Broglie wavelength of the lowest energy wave for which absorption is required [75]. In the Rydberg-surface system, the lowest energy state of the H atom is 1s. From $E_{kinetic} = \frac{1}{2}mv^2 = \frac{p^2}{2m}$, the de Broglie wavelength of relevance is $\lambda = \frac{2\pi}{\rho} = \frac{2\pi}{\sqrt{2(E_{1s}-\Phi)}}$, where Φ is the work function of the aluminium surface, the archetypal jellium surface. As $E_{1s} = -0.5$ a.u. and $\Phi = -0.574$ a.u., $\lambda \approx 16$ a.u. is the minimum width of the absorbing boundary that should absorb all of the electronic wavefunctions, however it is desirable to set the width much greater due to the effect of the lower density of grid points in the absorbing region. While the work functions

for the iron or copper surfaces used in this thesis are different from the jellium case, the absorbing region is sufficiently large that the results are not affected. Due to the required lower density of points and the minimum width of the absorbing region, in this thesis, unless otherwise stated, is $\Delta r = 30$ a.u..

The absorbing boundary is non-physical, so the absorbing potential needs to be located far away from the physical region of interest. This corresponds to the region in which there is no significant Rydberg surface-ionisation. It has been found experimentally that surface ionisation does not occur at significant levels for atom surface separations of $D > 5n^2 a_0$. Therefore in this thesis the lower bound of the absorbing region is given by $r_{\text{abs}} \geq 10n^2$ and as the width of the absorbing boundary $\Delta r = 30$ a.u., the outer edge of the absorbing boundary is $r_{\text{max}} = (r_{\text{abs}} + 30)a_0$ unless otherwise stated.

2.3.4 Time Evolution

Left-multiplying the time-dependent Schrödinger equation, equation 2.15, by $\langle v'l'|$ and using the orthogonality of the basis function results in a series of coupled equations,

$$i\frac{d}{dt}c^{nl}_{v'l'} = \sum_{vl} \langle v'l'| \widehat{H} |vl\rangle (t) c^{nl}_{vl}(t) \tag{2.33}$$

or in matrix representation,

$$i\dot{\mathbf{c}}(t) = \mathbf{H}\mathbf{c}(t) \tag{2.34}$$

$c(t)$ is a vector of the time-dependent expansion coefficients $c_{vl}^{nl}(t)$ and its first derivative with respect to time $\dot{\mathbf{c}}(t)$. $\mathbf{H}$ is the Hamiltonian matrix composed of the elements $\langle v'l'|\,\widehat{H}\,|vl\rangle$ from Eqn. 2.17. The Hamiltonian can be redefined to include the absorbing potential [75] described in section 2.3.3,

$$\mathbf{H} = \mathbf{H} - i\epsilon \tag{2.35}$$

Here $-i\epsilon$ is a diagonal matrix with elements $-i\epsilon(r) \times h(r - r_{\text{abs}})$ where $-i\epsilon(r)$ is the absorbing potential, r is the electron radial coordinate, r_{abs} is the lower bound of the absorbing region and $h(f(r))$ is the Heaviside step function. This modifies the formal solution shown in equation 2.33 to,

$$\mathbf{c}(t + \Delta t) = e^{-i(\mathbf{H} - i\epsilon)\Delta t}\mathbf{c}(t) \tag{2.36}$$

Time evolution of the wavefunction to time t occurs by multiplication of the initial wavefunction $\frac{t}{\Delta t}$ times by the matrix representation of the exponential propagator.

Here, the exponential operator is approximated by the symmetric split operator [77],

$$e^{-i(\mathbf{H} - i\epsilon)\Delta t} = e^{-i\frac{\mathbf{V}_{\text{perturb}}}{2}\Delta t}e^{-i(\mathbf{T} + \mathbf{V}_{\text{hydrogen}} - i\epsilon)\Delta t}e^{-i\frac{\mathbf{V}_{\text{perturb}}}{2}\Delta t} + O(\Delta t^3) \tag{2.37}$$

$\mathbf{T}$, $\mathbf{V}_{\text{hydrogen}}$ and $\mathbf{V}_{\text{perturb}}$ are matrix representations of the operators in equation 2.17. The convergence parameter in the calculations is the timestep and the smaller it gets the smaller the error term $O(\Delta t^3)$. The symmetric split operator is used as it is straightforward to implement and can be used

alongside the Manolopoulos absorbing potential [75]. The kinetic energy term is combined with the absorbing potential term as it has been shown that this arrangement leads to the smallest error [75].

The hydrogenic term $e^{-i(\mathbf{T}+\mathbf{V}_{\text{hydrogen}}-i\epsilon)\Delta t}$ is evaluated by diagonalisation of the complex matrix $(\mathbf{T}+\mathbf{V}_{\text{hydrogen}}-i\epsilon)$ such that,

$$e^{-i(\mathbf{T}+\mathbf{V}_{\text{hydrogen}}-i\epsilon)\Delta t} = \mathbf{X}\mathbf{D}^{\mathbf{e}}_{\mathbf{T}}\mathbf{X}^{-\mathbf{1}} \tag{2.38}$$

where $\mathbf{D}^e_T$ is the diagonal matrix containing the exponent of the eigenvalues multiplied by $-i\Delta t$ and $\mathbf{X}$ are the eigenvectors. The perturbation term $e^{-i\frac{\mathbf{V}_{\text{perturb}}}{2}\Delta t}$ is computed by application of the FBR/DVR transformation matrix $\mathbf{U}$, which alters the wavefunction from the FBR basis to the DVR basis where the potential energy matrix $\mathbf{V}_{\text{perturb}}$ is diagonal. This leads to,

$$e^{-i\frac{\mathbf{V}_{\text{perturb}}}{2}\Delta t} = \mathbf{U}\mathbf{D}^{\mathbf{e}}_{\mathbf{V}}\mathbf{U}^{\dagger} \tag{2.39}$$

where $\mathbf{D}^{\mathbf{e}}_{\mathbf{V}}$ is a diagonal matrix with $D^e_{Vii} = e^{V^{\text{DVR}}_{\text{perturb},ii}}$. After evaluation of all components of the symmetric split operator, the wavefunction is propagated forwards in time by performing a series of matrix multiplications.

2.4 Mean field calculations

As the Rydberg atom moves towards the surface it accelerates under the attraction of the ion and electron to their image-charges within the surface. Unless otherwise explicitly stated, the wavepacket propagation method ignores this acceleration and treats the Rydberg atom velocity as constant throughout

surface ionisation. A mixed quantum-classical approach known as the mean-field approach is implemented to account for the acceleration of the ion due to interaction with its image-charge [78].

This approach calculates an expectation value for the electronic Hamiltonian of the whole system, such that the force on the ion is given by,

$$M\ddot{D} = -\left\langle \Psi_{el} \left| \frac{\hat{H}_{el}}{dD} \right| \Psi_{el} \right\rangle - \frac{1}{4D^2} + F \tag{2.40}$$

$$= -\left\langle \Psi_{el} \left| \frac{dV_{\text{Surface}}}{dD} + F \right| \Psi_{el} \right\rangle - \frac{1}{4D^2} + F \tag{2.41}$$

where Ψ_{el} is the time-dependent electronic wavefunction, and $\hat{H}_{el}$ is the time-dependent electronic Hamiltonian with electron-independent terms taken out. V_{Surface} is the time-dependent surface potential as described in 1.3.2. The forces arising from the potential between the proton and its image-charge, $V_{pp} = -1/4D$ and the applied electric potential, $V^{p}_{Stark} = -FD$ are treated explicitly. Effectively the partial charge on the Rydberg atom during the surface ionisation process is calculated. All of the terms are distance and time dependent, such that during propagation of the wavepacket with time, the potentials are calculated at each time step.

The Rydberg classical orbital period is $\Omega_n = n^3/2\pi$, and gives a measure of the response time of the electronic wavefunction [12]. Comparison of the classical orbital period and the ion velocity allows assessment of the validity of the Born-Oppenheimer approximation, and the extent to which nuclear and electron motion are decoupled. The inclusion of mean field effects results in significant acceleration of the atom, but for the experimentally accessible hydrogen atom Rydberg states with the greatest collisional velocity,

this nuclear motion will still be three orders of magnitude slower than the classical orbital period, when measured over the time taken to pass through one orbital radius, i.e., $\Delta D = n^2$. For the low principal quantum number studied theoretically, Ω_n is far smaller and the nuclear motion is five orders of magnitude slower. Therefore, for all the systems studied in this thesis a Born-Oppenheimer approach is valid to describe the Rydberg-surface interaction. The electron wavefunction can be assumed to respond instantaneously to nuclear motion.

Chapter 3

Theoretical studies of hydrogen Rydberg atoms at confined structures

Previously the surface ionisation dynamics of hydrogen Rydberg atoms incident at flat metallic surfaces have been investigated by wavepacket propagation calculations [6] . The work presented in this chapter, is an extension of my Oxford M.chem part II thesis [79], which itself extends this method to confined systems.

3.1 Velocity effects in the ionisation dynamics of hydrogen Rydberg atoms at a projected band gap surface

The Cu(100) and Cu(111) surfaces have a projected band gap as described in section 1.5.1. When the Rydberg electron energy is in the energy range of this projected band gap, the induced image-states are long-lived as described in section 1.6 and resonance-enhanced charge transfer is expected when the Rydberg atom and the copper-localised image-state are degenerate. A wavepacket propagation study has previously been carried out to determine the effect of this projected band gap on the surface ionisation dynamics at a single velocity [25, 64]. Experimentally, as shown in chapter 5, unusual effects were seen when the Rydberg collisional velocity was varied. The calculations in this section extend the study to include collisional velocity and mean field effects.

3.1.1 Cu(100) and Cu(111)

The projected band gap of the Cu(100) and Cu(111) surfaces are at different energies due to their differing crystal structures at the surface. Therefore the long-lived image-states are at different energies, and the projected band gap is degenerate with some of the Rydberg energies.

Figure 3.1 compares the energies of the H atom Rydberg states with the Cu(111) and Cu(100) electronic states. Figure 3.1 suggests that there might be 2-3 resonances between the image or surface states and the H atom levels

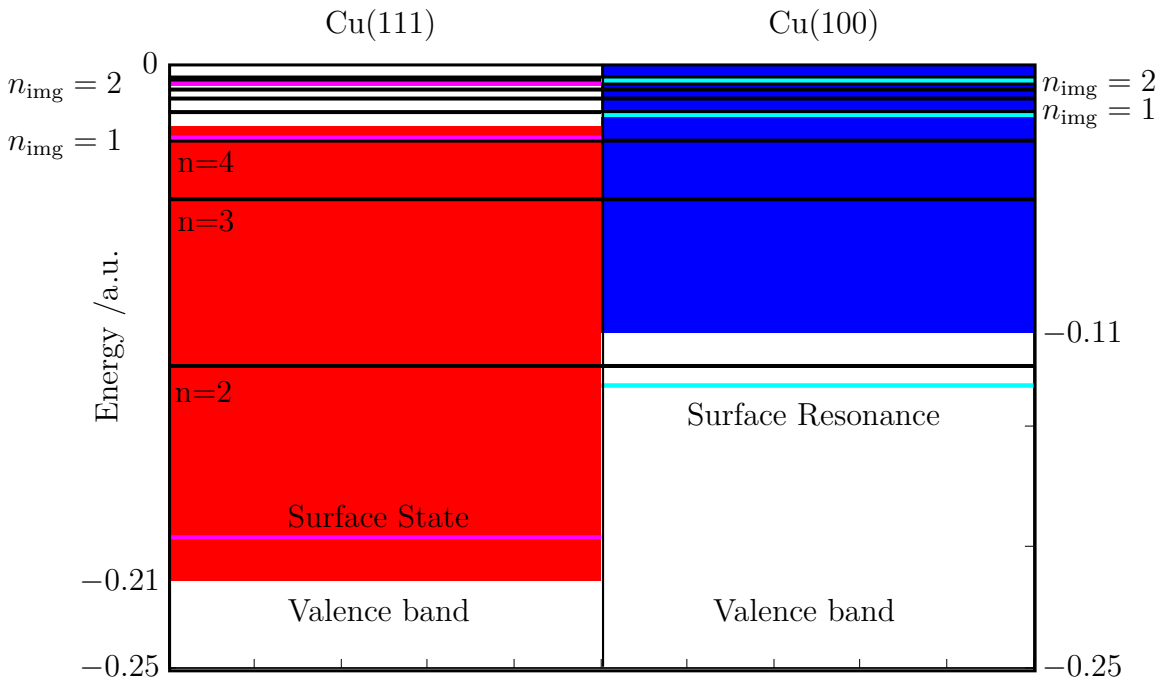

Figure 3.1: Table of energies from −0.25 a.u. to the vacuum level. The band gap of the Cu(111) surface is shown in red and the Cu(100) surface in blue. The valence band is for each surface lies in energy below the band gap and is labelled. The $n = 2 - 9$ hydrogen atom Rydberg states are shown in black. The surface states, surface resonances and image-states for the Cu(111) are shown in maroon and for Cu(100) in cyan. The image-states are labelled with the image-state quantum number.

in the range $n = 2 - 9$.

3.1.2 Previous studies

Borisov *et al.* investigated resonance effects in the charge transfer of H^- ions at a Cu(111) and free-electron metal surface using a wavepacket propagation method [58]. A strong blocking of resonant charge transfer was seen when the H^- was incident at the projected band gap Cu(111) surface, compared to the free electron metal surface.

The advantage of studying a Rydberg system compared to ground state H^- is that the resonance effects in charge transfer can be explored over a wide energy range by varying the principal quantum number. Additionally, high energy image and surface states which lie in the energy range of experimentally accessible Rydberg hydrogen atoms can be probed. Such states have been previously inaccessible. So *et al.* investigated the charge transfer of the Rydberg hydrogen atom, with principal quantum number $n = 2 - 8$, at the projected band gap surfaces Cu(100) and Cu(111) [64]. My calculations presented in this section are included in that work.

3.1.3 Wavepacket propagation study at a single velocity

The surface ionisation probabilities, as determined using the wavepacket propagation method, of the $n = 2 - 4$ hydrogen Rydberg atoms incident at a Cu(111) and Cu(100) surface, with a fixed perpendicular collisional velocity of $v_\perp = 1000\mathrm{m\,s^{-1}}$, are shown in figure 3.2. The surface ionisation probability is the flux of the Rydberg electron wavefunction into the metal surface as a function of atom-surface separation, or equivalently (for constant velocity) time. The evolution of this single electron wavepacket can be thought of in one of two ways; as a partial charge developing on a single Rydberg atom during surface ionisation, or as the statistical distribution of instantaneous surface ionisation distances for a large sample of Rydberg atoms.

The charge transfer of the Rydberg electron to the surface is enhanced for principal quantum numbers at which there is a near-degeneracy between the

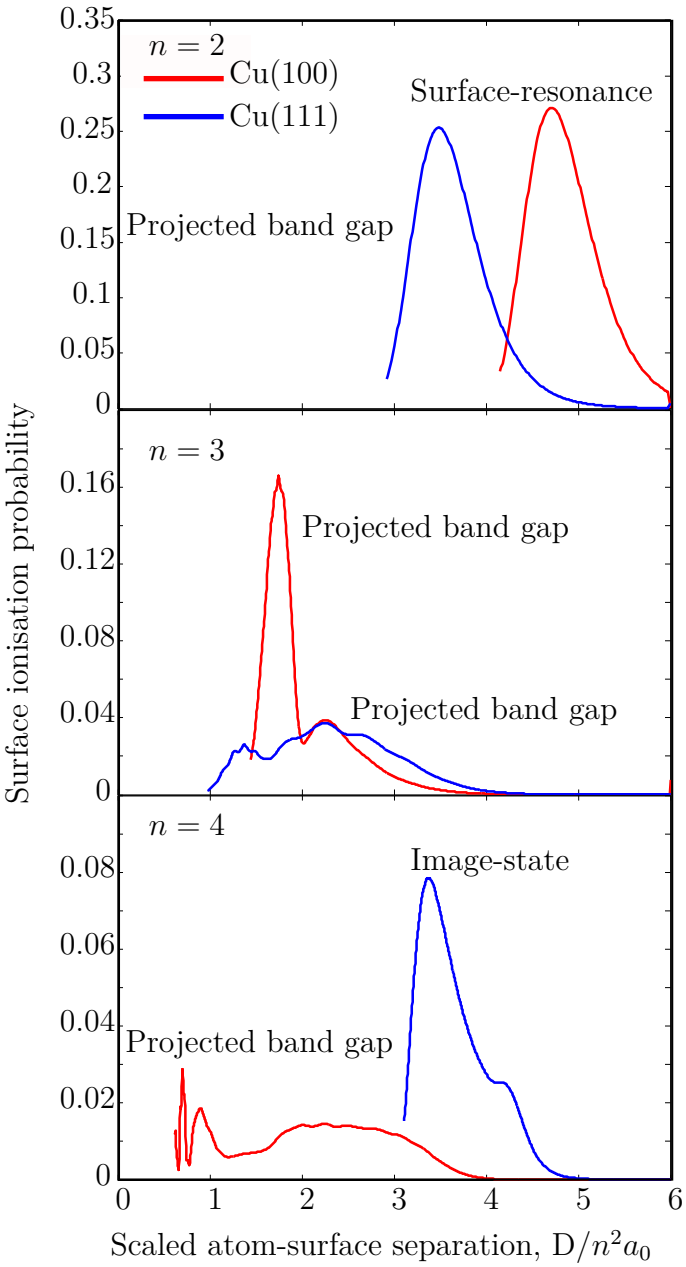

Figure 3.2: The surface ionisation probability of the $n = 2, 3, 4$ H atom Rydberg states at a Cu(100) and Cu(111) surface, calculated using a wavepacket propagation method. The constant perpendicular collisional velocity is $1000\mathrm{m\,s^{-1}}$. Each line is labelled as either surface-resonance, image-state or projected band gap to denote the type of the copper-localised state the Rydberg wavefunction is near to in energy.

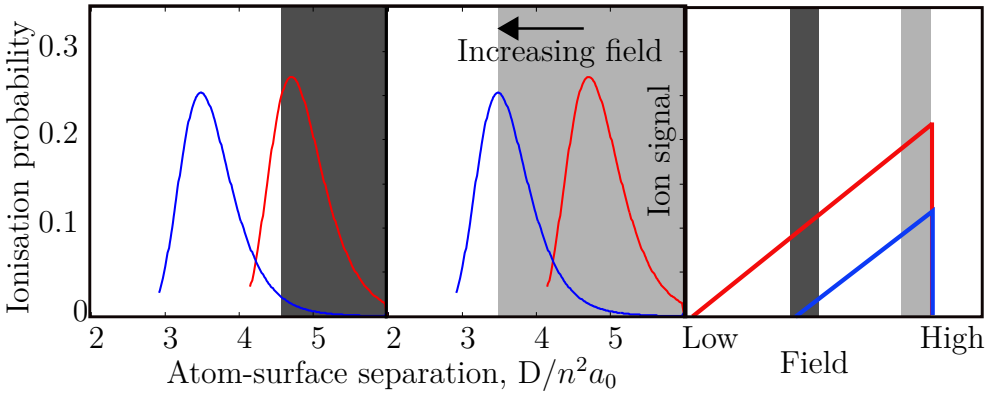

Figure 3.3: The surface ionisation probability of a Rydberg atom as a function of atom-surface separation incident at a surface with an off-resonance state in blue and on-resonance state in red. The application of a field will extract ions from the region shaded in dark grey on the left hand side. As the field is increased in magnitude ions nearer the surface will also be extracted as depicted in light grey in the middle figure. On the right hand side a 'surface ionisation profile' is plotted schematically. The shaded regions correspond to the region measured at a given applied field. Note that this figure is intended to be illustrative, as opposed to quantitative.

Rydberg energy level and an image-state or a surface-state. The enhancement is facilitated by the strong overlap of the surface image-state orbital lying outside the surface and the orbital of the incoming Rydberg atom. Resonance-enhanced charge transfer manifests itself as an increase in the integrated surface ionisation probability, and more commonly in the case of the copper surfaces investigated here, as a shift in the mean surface ionisation distance to larger atom-surface separations. As is shown in figure 3.2, resonances occur at several values of n and at different values for the two surfaces.

Any shift in the mean surface ionisation distance can be seen in the experimental surface ionisation profiles. By rearranging equation 1.21 the applied field F, can be converted into a minimum ionisation distance D_{min}

for extraction,

$$D_{\min} = \frac{T_\perp + \sqrt{F} + \sqrt{T_\perp^2 + 2T_\perp\sqrt{F}}}{2F} \tag{3.1}$$

where $T_\perp$ is the kinetic energy of the Rydberg atom. Effectively as the applied field increases ions formed at smaller atom-surface separations can be detected. The surface ionisation profile is the integral of the surface ionisation probability over the range of atom-surface separations from which the ion can be extracted by the applied field. This integral forms one point in the surface ionisation profile. This process is then cycled over the experimental range of applied fields to form the full surface ionisation profile. For example in figure 3.3 application of the field will result in extraction of the ions formed within the dark grey shaded region, resulting in a single point in the surface ionisation profile, shown on the left hand side by the dark grey stripe. As the field is increased, as shown in light grey, the detection region increases so there is more signal in the surface ionisation profile as shown by the light grey stripe on the right hand side. Increasing the field, as occurs during the recording of a surface-ionisation profile, shifts the detectable region, from where ions can be successfully extracted, towards the surface.

For a Rydberg atom incident at a surface with a degenerate surface-localised state, depicted in red in figure 3.3, surface ionisation occurs further from the surface than for the off-resonance case shown in blue. When a small field is applied in the left hand picture, over half of the ions produced by surface ionisation at the on-resonance surface, depicted in red, will be detected, but only a very small fraction of ions from the off-resonance surface will be detected. This results in far more signal for the on-resonance surface at

low fields than the off-resonance surface. As the field is increased all of the on-resonance ions are detected, as are a larger fraction of the off-resonance ions. Therefore both surface ionisation profiles increase in intensity at high field. However the field can only be increased until the field ionisation threshold is reached. If the whole range of distances over which surface ionisation occurs is not accessible by the field range, then there will also be an overall difference in intensity at the field ionisation cutoff as depicted in figure 3.3. Effectively surface ionisation occurring further from the surface, is more detectable over any given field range, than surface ionisation occurring close to the surface.

The Cu(100) has a surface resonance close in energy to the $n = 2$ hydrogen atom Rydberg state energy, as shown in figure 3.1. In comparison, the Cu(111) has a band gap with no surface or image-states nearby. The mean atom-surface separation, for surface ionisation is calculated to be $\Delta D = 1.5n^2$ further from the surface for Cu(100) than Cu(111), demonstrating resonance-enhanced charge transfer for the $n = 2$ H atoms incident at Cu(100), as shown in figure 3.2. This would result in more signal at lower extraction fields in the surface ionisation profile for the on-resonance versus off-resonance state.

For both copper surfaces, the $n = 3$ Rydberg energy level is in the band gap, energetically far away from any surface or image-states. Figure 3.2 shows that, surface ionisation occurs closer to the surface for both $n = 3$ systems, than for the off-resonance $n = 2$. Surface ionisation close to the surface, requires larger extraction fields, and so is less detectable, resulting in overall less surface ionisation signal in the surface ionisation profile. The slightly different behaviour between the surface planes in figure 3.2 can be attributed to the smaller energetic gap between the $n = 3$ Rydberg state and the Cu(111)

image-state, compared to the Cu(100). Therefore the mean atom-surface separation for surface ionisation is seen for the Cu(111) system at $D = 3n^2$, whereas for the Cu(100) it is at $D = 1.8n^2$.

Finally the $n = 4$ and the Cu(111) first image-state are very close in energy so that resonance-enhanced charge transfer occurs at a large mean ionisation distance of $D = 3.8n^2$. The mean ionisation distance for the Cu(100) surface is $D = 2n^2$, because the first image-state is significantly higher in energy than the $n = 4$ Rydberg state, resulting in less surface ionisation signal.

To focus on the resonance effects of the projected band gap embedded surface states and image-states, the calculations are performed here on the most surface-oriented state (the most red-shifted state) of the n-manifold, which has the largest overlap with the surface. Additionally, only calculations for low principal quantum number hydrogen Rydberg atoms are feasible due to the larger grids required for larger atoms leading to increasing computational time. This combination means that the red-shifted low n Rydberg atoms investigated in this chapter, are different to the $k = 0$, higher n Rydberg atoms used in the experimental chapter, i.e. the results in this chapter are illustrative, rather than quantitative.

3.1.4 The effect of collisional velocity

There are two ways in which the collisional velocity of the hydrogen Rydberg atom may affect the surface ionisation behaviour. Firstly, as shown by equation 3.1, the collisional velocity determines the detectable region from which ions produced via surface ionisation can be successfully extracted. Secondly

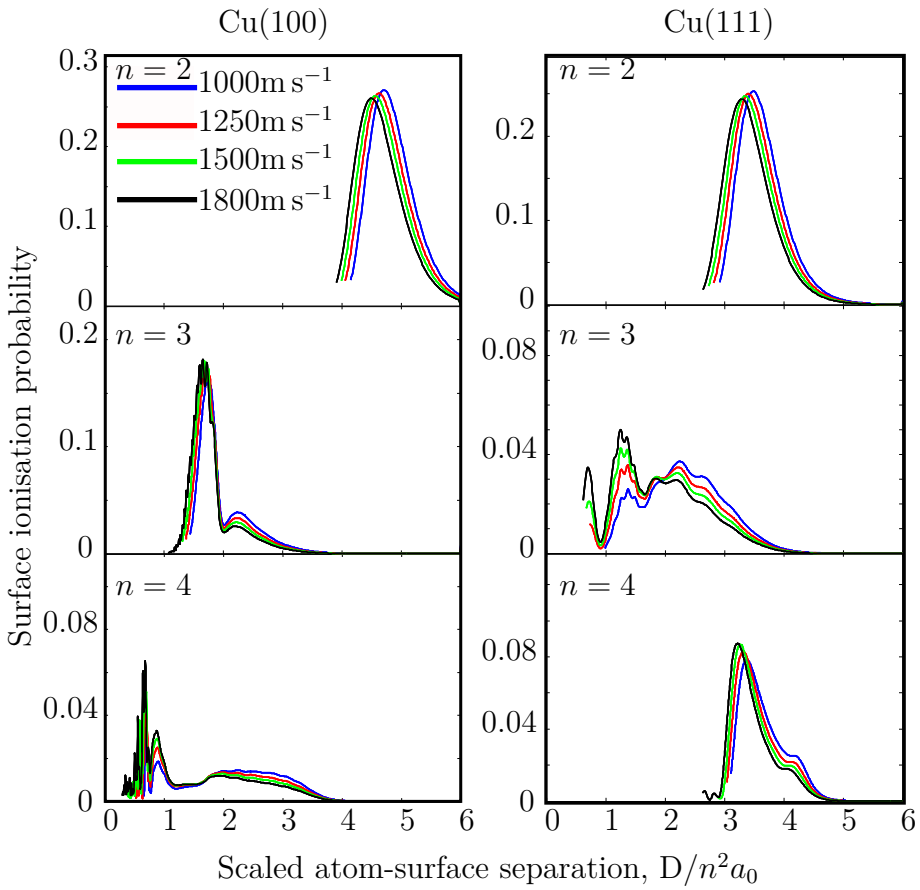

Figure 3.4: The surface ionisation probabilities for the $n = 2 - 4$ incident at the Cu(111) and Cu(100) surfaces, for perpendicular collisional velocities 1000m s^{-1} to 1800m s^{-1}, calculated using the wavepacket propagation method and the constant velocity approximation.

increasing the collisional velocity gives the Rydberg atom less time to ionise at a given position in space, as fundamentally electron transfer occurs at a finite rate. This results in the maximum in the surface ionisation probability shifting to smaller atom–surface separations with increasing collisional velocities.

3.1.5 Constant Velocity

The wavepacket calculations presented in this subsection model the incident velocity of the hydrogen Rydberg atom as a constant throughout the surface ionisation process. Figure 3.4 shows the surface ionisation probabilities of the $n = 2 - 4$ hydrogen atom Rydberg states incident at a Cu(111) or Cu(100) surface for a range of collisional velocities from $1000\mathrm{m\,s^{-1}}$ to $1800\mathrm{m\,s^{-1}}$. Increasing the incident H-atom velocity shifts the mean ionisation distance to smaller atom–surface separations for all principal quantum numbers. For the $n = 2$ hydrogen Rydberg states, the shift with velocity is similar for both the on- and off-resonance Cu(100) and Cu(111) surface localised states. For the on-resonance $n = 4$ Cu(111) the peak surface ionisation probability shifts to a smaller atom-surface separation as the velocity is increased, whereas the $n = 4$ hydrogen Rydberg atom at the Cu(100) surface still surface ionises primarily within an atom-surface separation of $1n^2$.

The minimum ionisation distance for extraction, for a given applied field is dependent on the Rydberg atom's collisional velocity as shown in equation 3.1. Figure 3.5 schematically shows the shift in detection region away from the surface as the collisional velocity of the Rydberg atom is increased. This shift occurs for the whole range of fields scanned during the recording of a surface ionisation profile, such that the integrated intensity of the whole surface ionisation profile is reduced for both on- and off-resonance states.

Both the shift in ionisation probability to smaller mean atom-surface separations and the movement of the detection region away from the surface with increasing collisional velocity, causes a reduction in the intensity of a

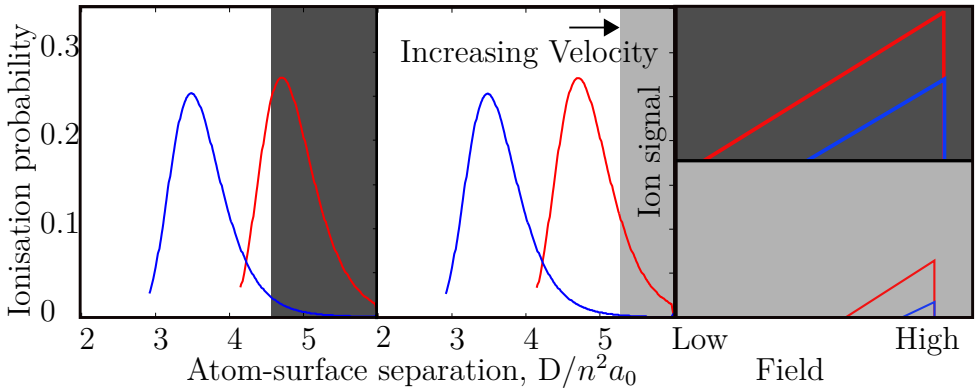

Figure 3.5: The surface ionisation probability of a Rydberg atom as a function of atom-surface separation incident at a surface with an off-resonance state in blue and on-resonance state in red. The application of a field will extract ions from the region shaded in dark gray on the left hand side. As the perpendicular collisional velocity is increased the region from which ions can extracted moves further from the surface, as shown in light grey. On the right hand side two 'surface ionisation profiles' are plotted schematically. The profile shaded in dark grey shows the larger signal for H atoms with lower collisional velocities. Note that this figure is intended to be illustrative, as opposed to quantitative.

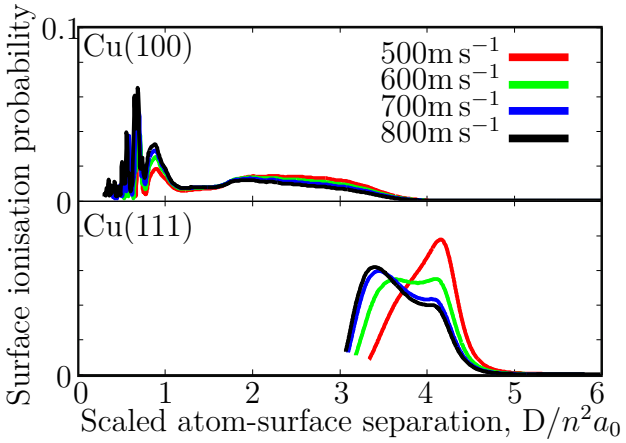

Figure 3.6: The surface ionisation probabilities for the $n = 4$ H atom Rydberg states incident at a Cu(100) (top) and Cu(111) (bottom) surface. The wavepacket propagation calculations are carried out at the experimentally accessible constant perpendicular collisional velocities of 500m s^{-1} in red, 600m s^{-1} in green, 700m s^{-1} in blue and 850m s^{-1} in black.

surface ionisation profile. Experimentally as the surface ionisation profiles are recorded for a variety of collisional velocities, the integrated intensities of the profiles are seen to decrease with increased collisional velocity, as shown in chapter 5.

Experimentally, we can alter the velocity of the incident H atoms by changing the delay between the excimer laser and the excitation lasers, and additionally by altering the seeding gas. Using unseeded ammonia in our pulsed valve we can access a range of perpendicular collisional velocities from 500m s^{-1} to 850m s^{-1} whilst maintaining a reasonable molecular beam density. For a given Rydberg atom state, the experimental range of velocities is expected to cause measurable changes in the surface ionisation probability.

Figure 3.6 shows the variation in the $n = 4$ surface ionisation probabilities for Cu(111) and Cu(100) over this range of experimentally accessible velocities.

The larger fractional change in collisional velocity at these lower velocities results in a larger change in surface ionisation probability with collisional velocity than seen in figure 3.4. Here much more significant changes are seen for the Cu(111) surface than the Cu(100), as the maximum in the surface ionisation probability shifts by $\Delta D \approx n^2$ for the Cu(111) case but not for the off-resonance Cu(100) case. This larger change in surface ionisation probability for the on-resonance Rydberg state with collisional velocity, coupled with the greater detectability of ions ionising further from the surface, leads to much greater variation with collisional velocity in the surface ionisation profile of the on-resonance $n = 4$ at a Cu(111) surface than for the off-resonance $n = 4$ at Cu(100). Additionally the experimental surface ionisation profiles would be much more intense for the on-resonance case, than the off-resonance case. Therefore these results suggest that by tuning collisional velocity experimentally any resonance effects in the surface ionisation profiles will be enhanced.

3.1.6 Mean field calculations including atomic acceleration

On approaching the surface the ion and the electron which make up the Rydberg atom are attracted to their own image charges causing an acceleration of the atom towards the surface. This effect is explicitly neglected in the constant velocity calculations but can be included by the addition of a mean field term [78]. This used the instantaneous electronic wavefunction to calculate the mean field due to the electron on the fly and hence the

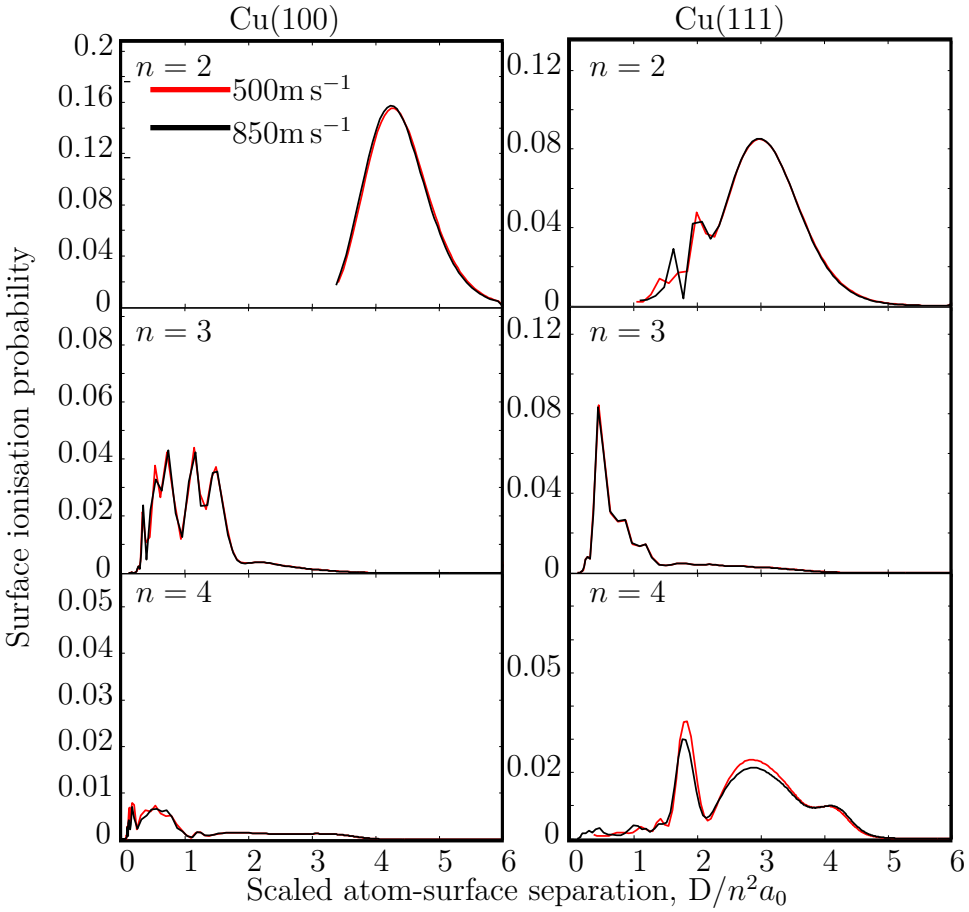

Figure 3.7: The surface ionisation probabilities for the $n = 2 - 4$ H atom Rydberg states incident at a Cu(100) and Cu(111) surface with perpendicular collisional velocity of 500m s^{-1} in red and 850m s^{-1} in black. The surface ionisation probabilities have been calculated using a wavepacket propagation method which accounts for the mean field acceleration of the atom on approaching the surface.

forces on the ion, as described in section 2.4. Previous mean field wavepacket propagation studies with Rydberg atoms and a gold surface found that the inclusion of acceleration effects was required for quantitative comparison of the theoretical and experimental results, however the constant velocity calculations gave a good qualitative understanding [25].

There are two components to the acceleration felt by the atom, whose centre of mass is essentially at the position of the ion. At large distances a small Van der Waals type interaction is experienced which scales with atom-surface separation, D, i.e. $a_{VdW} \propto D^{-4}$, and closer to the surface a much larger acceleration occurs whilst the atom is stripped of its electron during the surface ionisation process leading to a partially charged species. This second acceleration dominates the final velocity. The magnitude of the acceleration effect, computed for low principal quantum numbers, is hard to scale with n to the experimentally-accessible higher principal quantum number Rydberg atoms. This is because the second acceleration is dependent on the exact form of the surface ionisation probability for a given system. Therefore the results presented here are expected to be qualitative predictions rather than quantitative.

Figure 3.7 shows the surface ionisation probability for the $n = 2 - 4$ hydrogen Rydberg states with Cu(111) and Cu(100) surface at an initial collisional velocity of $500\mathrm{m\,s^{-1}}$ or $850\mathrm{m\,s^{-1}}$, calculated using the wavepacket propagation method including mean field acceleration effects. In all cases, inclusion of the mean field term causes a reduction in the mean atom-surface separation upon ionisation and an acceleration of the ion on approach to the surface. This results in a shift in the detectable region away from the

surface, such that the ions become less detectable. Additionally, the mean field acceleration dominates the variation in the initial velocity, such that the atom-surface separation at which surface ionisation occurs is less sensitive to the initial velocity. Therefore tuning the initial velocity is expected to have less of an effect on the surface ionisation probability when calculated using the mean field approximation. However, this effect of the acceleration is less for on-resonance states, such as the image-charge resonance at Cu(111) n=4, resulting in a larger atom-surface separation for the maximum of the surface ionisation probability. In this case the terminal velocity of the ion is more than an order of magnitude smaller than the off-resonance case. This is because the ionisation occurs at greater distances where the image-charge acceleration is less. Coupling these effects leads to a greater variation of the ionisation probability curves with initial incident velocities for on-resonance states, than off-resonance states. However as there is no extraction field present in these calculations, none of the ions produced via surface ionisation would be extracted, and ultimately the calculations do not represent a physically useful system.

3.1.7 Mean field with electric field

Under experimental conditions, the extraction field is applied before surface ionisation occurs, such that the Rydberg electron's wavepacket evolves under the presence of a large field. This applied field reduces the ion acceleration, especially during the deshielding of the ion during surface ionisation. The presence of an applied negative field attracts the partially charged ion away

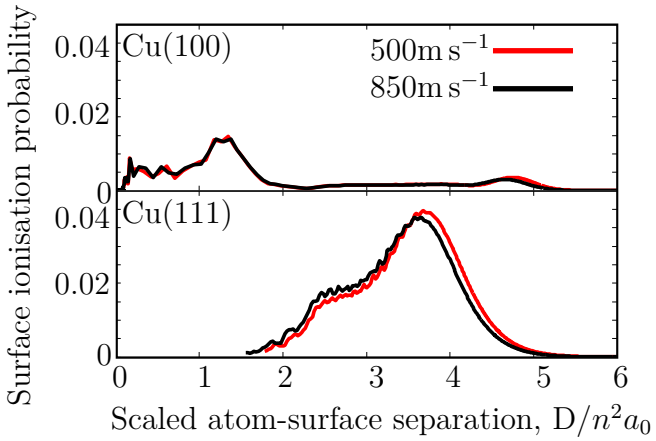

Figure 3.8: The surface ionisation probabilities for the n=4 hydrogen atom Rydberg state incident at a Cu(111) and Cu(100) surface with an initial experimental velocity of 500m s^{-1} or 850m s^{-1} and in the presence of an external field of 770000V cm^{-1}.

from the surface, and opposes its attraction to its image charge, such that the amount of acceleration experienced during the surface ionisation process is significantly decreased. The size of this effect increases with the size of the applied field, such that a large field results in both a larger range of distances over which ions are detected, and the formation of more ions within that detection region as the maximum in the surface ionisation probability moves away from the surface. When the applied field is reduced during the measurement of a surface ionisation profile, the effect is a reduced detection efficiency, or zero detection efficiency, and therefore a loss of surface ionisation signal.

Figure 3.8 shows the surface ionisation probability for the $n = 4$ hydrogen atom Rydberg state at a Cu(111) and Cu(100) surface including mean field effects, and with a 770000V cm^{-1} applied field. This is the field that would be required to extract an ion formed at position $D = 3.2n^2$ for a constant

collisional velocity of $650\mathrm{m\,s^{-1}}$. When compared to the surface ionisation probabilities presented in figure 3.6, which show the same $n = 4$ hydrogen atom Rydberg states at the same initial collisional velocities but calculated using the constant velocity approximation, surface ionisation occurs closer to the surface when mean field effects are included. In both sets of calculations a partial charge begins to develop on the Rydberg atom at $D = 4.8n^2$ for the on-resonant Cu(111) case, however once mean field acceleration effects are included the atom remains partially charged for a greater distance than at constant velocity. Additionally the terminal velocity at the point of full ionisation is far larger when mean field acceleration effects are included, such that any ions produced will be less detectable.

From figure 3.8 it is clear that the surface ionisation probability for the on-resonance system is more sensitive to collisional velocity than the off-resonance case. Additionally the terminal velocities are far lower for $n = 4$ Rydberg atoms ionising in front of a Cu(111) surface, such that these ions are more detectable. Coupling these effects results in a greater expected sensitivity for on-resonance systems, than off-resonance systems as collisional velocity is tuned, even when mean field effects and the presence of large applied fields are considered. Therefore it is expected that such effects should be observable experimentally.

Generally the mean field acceleration effects seen in these calculations are very large, but this is exacerbated by the low principal quantum numbers used throughout this theory work. The Van der Waals acceleration is dependent on atom-surface separation, such that the low n Rydberg atoms which ionise closer to the surface, are accelerated significantly before ionisation starts. Once

surface ionisation is occurring, the secondary acceleration term dominates, which is due to unshielding of the ion as the electron is stripped away. This term is dominated by whether the state is on- or off-resonance; in effect the longer the time taken for the electron to be stripped off the ion, the greater the acceleration. However this effect cannot be easily scaled with principal quantum number.

The wavepacket propagation calculations determine the evolution of a single Rydberg electron wavepacket as a function of time, such that the Rydberg atom is not fully ionised until the electron population outside the metal has fully depleted, i.e., the short atom-surface separation end of the surface ionisation probability curve. In this interpretation all the ions formed under a given set of conditions will be detected, or not depending on whether the field is large enough. Effectively the calculated surface ionisation profile would look like a step function, however the gradual rise in surface ionisation signal with applied field has experimentally been attributed to the presence of patch charge stray fields which are not accounted for in these calculations [11, 30].

In the constant velocity case, the surface ionisation probability curves, such as in figure 3.6, can also be interpreted as a statistical distribution of instantaneous ionisation distances in a sample of Rydberg atoms. In this interpretation ions are formed instantaneously over the range of atom-surface separations where there is a non-zero probability of surface ionisation. However using the semi-classical mean field approximation makes this interpretation invalid. The acceleration on the atom, which leads to the shift in ionisation probability curve, is calculated by developing a partial charge on the atom,

which does not occur if ionisation is assumed to be instantaneous at a specific position. In order for the effect of nuclear motion to be fully determined on the surface ionisation system a full quantum treatment of the nuclear wavefunction is required which is beyond the scope of this thesis.

3.1.8 Convergence

The computation of the wavepacket propagation for the electronically structured Cu(111) and Cu(100) surfaces is much more demanding than the Jellium surface. This is due to the periodic nature of the pseudo-potential inside the metal, which requires a large number of radial grid points, and the large components of the electron momentum parallel to the surface in the resonance charge transfer, which requires a large angular momentum basis.

Typically, for the calculations carried out above, the numerical grid consists of $\sim 1000 \times 200$ (radial $\times$ angular) grid points. For equivalent wavepacket propagations involving a jellium surface convergence can be reached using $\sim 200 \times 80$ grid points. This means that the number of basis functions, N, for the copper calculations is an order of magnitude larger than for jellium, and the computation speed over three orders of magnitude slower.

Even using such a large basis set, for the charge transfers that are restricted by the band gap and unaided by the resonance effects of surface or image-states, high frequency oscillations are superimposed on the ionisation probability profiles, and increasing the number of radial and angular points would alter the *form* of the detailed profiles.

However, it was found that for the results presented in this section, the

calculations are sufficiently converged that the average ionisation distance, and the range of atom-surface separations spanned by the ionisation probability profiles, do not change significantly with a larger radial or angular basis, and so are acceptable for the comparison carried out.

Furthermore, it has been shown by So *et al.* [64] that resonance charge transfer to band gap embedded surface and image-states can be observed directly from plots of the electronic wavefunction density in the wavepacket propagation, confirming that the different onset of ionisation distances is not an artefact of the unconverged calculations.

3.1.9 Experimental Measurement

In chapter 5 experimental results investigating the resonance-enhanced charge transfer of $k = 0$, $n = 25 - 34$ hydrogen atom Rydberg states at a Cu(100) surface are presented. The hydrogen Rydberg atoms with principal quantum numbers $n = 2-4$ investigated in this section are not experimentally accessible due to lifetime effects. Therefore the Cu(100) surface, where the projected band gap extends above the vacuum level as shown in figure 3.1, is investigated as it is expected the $n = 25 - 34$ hydrogen atom Rydberg states will overlap with the Rydberg series of surface localised image-states. Based on the qualitative conclusions about the resonance effects described in this chapter, these are expected to play an important role in the charge transfer dynamics of the system.

3.2 Theoretical study of the hydrogen Rydberg atom and nanoparticle interaction

In its simplest form, a single nanoparticle can be described as a fully isolated three-dimensional sphere. In this section the potential is modelled as a three-dimensional spherical well as described in subsection 2.3.2.4, which gives rise to discrete well-localised states. When an electron is placed outside the nanoparticle, image-states are induced, which are long-lived due to the absence of an overlapping conduction band within the nanoparticle. When the image-states and the hydrogen Rydberg energy match, resonance-enhanced charge transfer is predicted by the calculations in this section. These calculations were motivated by the experimental study of charge transfer at nanoparticle coated surfaces by Dethlefsen [80].

3.2.1 The energy levels and wavefunctions of the nanoparticle

Nanoparticles with radius, $R \leq 3$nm, are modelled in this work as an isolated jellium sphere. The fully confined nature of the potential leads to the presence of discrete spherical-well localised states. Analogous to the simplistic particle–in–a–box model, as the radius of the nanoparticle increases there are more energy levels of the well, which are closer together in energy. A nanoparticle of small size does not have a metallic continuum. Ultimately as the radius increases a continuum of states forms, tending towards the limit of a curved metallic surface of a bulk material.

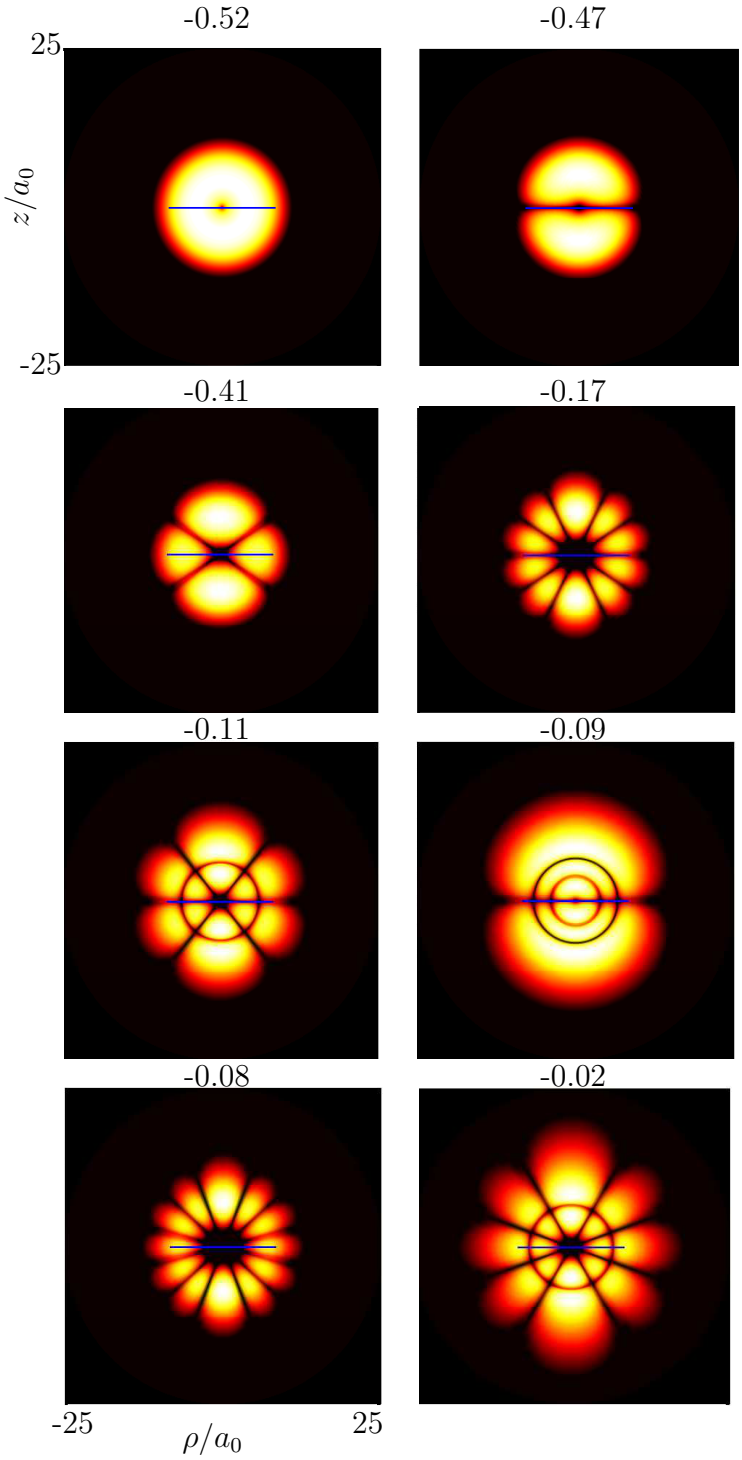

Figure 3.9: The probability density of a selection of nanoparticle wavefunctions for the $r = 10a_0$ nanoparticle. The energy of the wavefunction is noted above each figure in a.u.. The blue horizontal line depicts the radius of the nanoparticle.

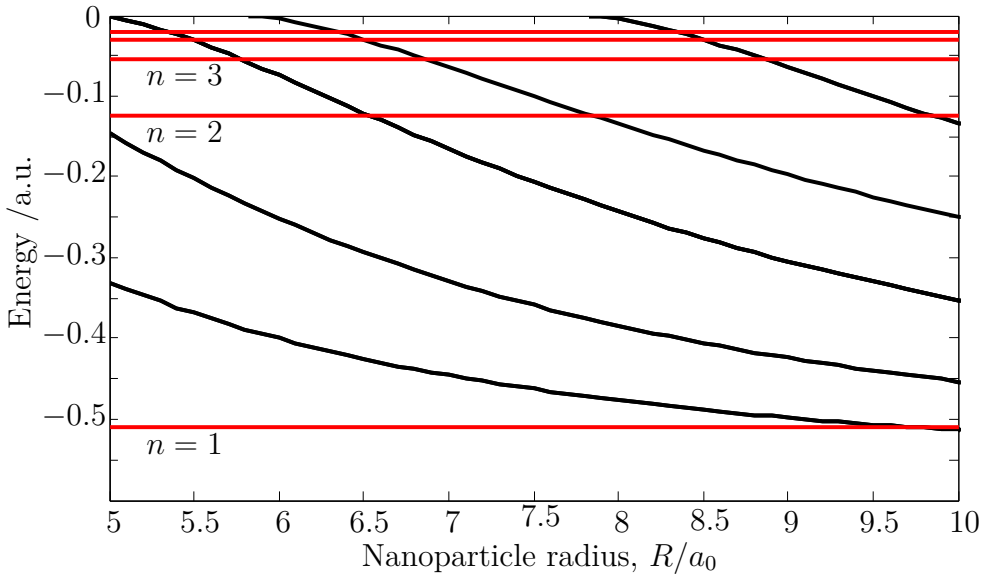

Figure 3.10: The well-image state energy levels of the nanoparticle as a function of nanoparticle radius in black, and the $n = 1 - 5$ hydrogen atom Rydberg energy levels as determined from equation 1.13 in red at $D = 3n^2$. At the intersection of the black and red lines resonance-enhanced charge transfer is expected.

As shown in figure 3.9 the probability density of the nanoparticle wavefunctions, calculated by diagonalisation, have at small radii, atom-like character. It is possible to attribute n, l and m_l quantum numbers to them. The pure spherical-well localised states are fully confined by the edge of the nanoparticle. The probability density of the first two wavefunctions in figure 3.9 are almost pure spherical-well states, as can be seen by the small amount of probability density extending beyond the blue line, which depicts the physical boundary of the nanoparticle.

When there is an electron outside the nanoparticle, as in Rydberg surface ionisation, the lack of a conduction band leads to long-lived image-states, with significant amplitude extending into the vacuum. The overlap of these spherical-well states and the image-states, leads to so called 'well-image

states'. Individual wavefunctions have differing amounts of spherical-well state character or image-state character, but the wavefunction of an electron occupying a hybrid well-image state would both occupy the nanoparticle itself, and protrude into the surrounding vacuum. All of the wavefunctions in figure 3.9 have mixed well-image character, but the first two have very little image-state character, whereas the higher n, l states have significant image-state character and extend well into the vacuum. At very low energies, near the bulk-metal value of the well, pure well-localised states are found, however higher in energy when the spacing between image-states becomes smaller, hybrid well-image states dominate.

As the radius of the nanoparticle increases, there are more well-states, but the same number of image-states, such that there are more pure well-states at low energies, and the hybrid well-image states typically have more well-state character. The electron wavefunction contracts to the nanoparticle surface as the radius of the nanoparticle increases [33], ultimately forming a conduction band within the nanoparticle, and the well-image states become image resonances.

The potential used to model the nanoparticle is described in section 2.3.2.4. A Hamiltonian is built by considering an electron outside this nanoparticle potential, and discretising it onto a Sinc DVR as described in section 2.2.5. The well-image state energies and wavefunctions are determined by diagonalisation of this Hamiltonian. Figure 3.9 plots the probability density for each wavefunction using $|\psi\psi^*|$.

For the smallest nanoparticles investigated in this section, the jellium model is no longer applicable, as clusters of just a few atoms are not nec-

essarily spherical. However it is used throughout this section to enable the investigation of physical trends and size matching using low-n Rydberg atoms.

Sequential diagonalisations of the sphere Hamiltonian, in the absence of the Rydberg ion core, yield the well-image energy levels of the nanoparticle as a function of sphere radius, as shown by the black lines in figure 3.10. The Rydberg energies shown in red are determined using equation 1.13, for a Rydberg atom at $D = 3n^2$ from the nanoparticle. At the intersection of the black and red lines resonance-enhanced charge transfer is qualitatively predicted. For example for the $n = 2$ hydrogen Rydberg atom resonance-enhanced charge transfer is expected when it collides with a $R = 6.7, 7.8, 9.7a_0$ nanoparticle.

3.2.2 Previous studies

Rinke *et al.* theoretically investigated the image-states of metal clusters, or small nanoparticles [33]. Finite numbers of wavefunctions were determined due to the confinement of the potential and a contraction to the bulk of the wavefunction with increasing radius was also found as in my work. The nanoparticle potential used in this thesis, was derived from their potential.

Kasperovich *et al.* have experimentally investigated electron capture by the image-states of metal nanoparticles [81]. A beam of electrons is produced by an electron gun and crosses a beam of sodium nanoclusters. Electron capture by the image-states of nanoparticles charges the nanoparticle and gives it a magnetic moment, which allows its to be steered off course by a large applied magnetic field. Neutral nanoparticles are fragmented and ionised by

UV light and counted by an ion detector. Ultimately the electron capture cross-section between the nanoparticle and the electron is determined by the signal depletion when the electron gun is turned on. The electron capture cross-section gives an indication of the size of the nanoparticle to within 20%.

The only experimental study investigating Rydberg surface ionisation at nanoparticles occurred in our lab [80]. Extreme red-shifted, blue-shifted and mid-manifold $n = 26-34$ hydrogen Rydberg atoms were fired at nanoparticles of diameter $\phi \approx 10$nm laid down on a Si wafer. The clearest finding from this work was a k-state change for the extreme blue-shifted Rydberg atoms, i.e. the surface ionisation profiles of the $n, k = n - 1$ resembled the $n + 1, k = -n + 1$ surface ionisation profiles. This was attributed to the electrostatic curvature of the field lines near the nanoparticle and the resultant state-mixing as the Rydberg atom passes through this inhomogeneous field. No resonance-enhanced charge transfer was seen, but surface analysis revealed large areas of exposed substrate and clustering of the nanoparticles on some of the surfaces, such that it is difficult to determine the relative contribution of charge transfer to an isolated nanoparticle or the silicon substrate within the measured signal.

The work in this section represents, to the best of our knowledge, the first theoretical study investigating the surface ionisation dynamics of a hydrogen Rydberg atom at a nanoparticle. No other previous theoretical or experimental studies have been carried out to investigate the charge transfer of ions or Rydberg atoms at a nanoparticle.

3.2.3 Ionisation probability in the static-atom calculations

The three-dimensional confinement of the nanoparticle potential means that a Rydberg atom held static in front of a nanoparticle cannot be fully ionised. At atom-surface separations where surface ionisation is significant for bulk materials the overlapping wavefunctions of the Rydberg atom and the nanoparticle form a non–stationary state, whereby the electron flows back and forth between the nanoparticle and localisation on the Rydberg atom.

The electron population within the nanoparticle oscillates in time as the system is in a non-stationary state formed by a linear combination of the Rydberg state and the nanoparticle-localised well-image state. In the near resonant case this can understood by considering the populations of a two-level system under the influence of a time independent perturbing potential $V_{\mathrm{perturb}}(r,\theta) = V_{\mathrm{surface}}(r,\theta)$, where $\psi(0)$ is the initial wavefunction localised on the atomic core ($a_{\mathrm{Ryd}}(0) = 1$),

$$\psi(t) = a_{\mathrm{well}}(t)\psi_{\mathrm{well}} + a_{\mathrm{Ryd}}(t)\psi_{\mathrm{Ryd}} \tag{3.2}$$

$$E_{\mathrm{well}} - E_{\mathrm{Ryd}} = \omega_0 \tag{3.3}$$

$$P_{\mathrm{well}} = |a_{\mathrm{well}}|^2 = \left(\frac{4V^2}{\omega_0^2 + 4V^2}\right) \sin^2 \frac{1}{2}(\omega_0^2 + 4V^2)^{\frac{1}{2}} t \tag{3.4}$$

Here $V^2 = H_{i,j}^2$, where i is the Rydberg state and j is the well-image-state, and equation 3.4 is the Rabi formula. P_{well} is the probability of the electron occupying the well-image-state as a function of time. The mathematical form shows that the probability of the electron being within the nanoparticle

will oscillate in time sinusoidally and has an amplitude which is inversely proportional to the energy gap between nanoparticle and Rydberg states, and a frequency which is linearly proportional to the same gap. This is seen in the probability oscillations from the wavepacket propagation calculations where non-degenerate states that are close in energy are characterised by large amplitudes and low frequencies, and the larger the energy gap between the states the higher the frequency and the lower the amplitude. P_{well} can be used to approximate the surface ionisation probability for a non-stationary state, by either measuring the amplitude or frequency of the nanoparticle-localised population oscillation.

Static-atom calculations with the atom at a fixed position allow any resonance effects to be seen clearly without the complicating factor of a time-dependent wavepacket evolution on approach to the surface. However the static-atom situation is clearly an unphysical system and tells us nothing of the dynamics of the surface ionisation process. The measurement of a large amplitude and low frequency is indicative of a high probability of charge transfer, and in the following section the maximum amplitude of the population oscillation will be denoted as the surface ionisation probability.

3.2.4 Results of the static-atom calculations

Figure 3.11 shows the surface ionisation probability for the $n = 2$ hydrogen Rydberg atom held at a constant atom-surface separation in front of a small nanoparticle of variable radius between $R = 4 - 8a_0$. Clear resonance-enhancement of charge transfer is seen for a nanoparticle of radius $R =$

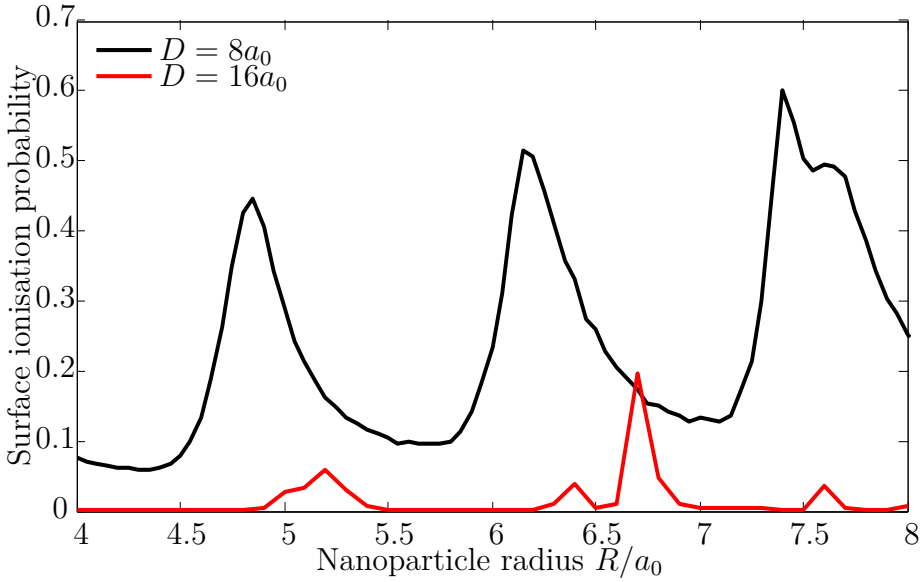

Figure 3.11: The surface ionisation probability determined using a static-atom propagation for the $n = 2$ hydrogen atom Rydberg state and a nanoparticle of radius $R = 4a_0 - 8a_0$. The red line shows the results from the static-atom propagations at an atom-surface separation $D = 16a_0$, and the black line at $D = 8a_0$. Note that the magnitude of the surface ionisation probability for the $D = 16a_0$ praopagations has been increased three fold to aid comparison.

$4.7a_0, 6.3a_0, 7.6a_0$ and a low rate of charge transfer for a nanoparticle of radius $R = 4.3a_0, 5.5a_0, 7a_0$ at a fixed atom-surface separation of $D = 8a_0$. The field-free and static-atom nature of these calculations means this variation with nanoparticle radius must be due to the energy matching between the Rydberg atom and the well-image-state, i.e., at $R = 4.7a_0, 6.3a_0, 7.6a_0$ the well-image-state and $n = 2$ Rydberg atom are degenerate.

The red line in figure 3.11 depicts the static-atom wavepacket propagations carried out at $D = 4n^2 = 16a_0$. These Rydberg atoms, further from the nanoparticle, have a much smaller probability of surface ionisation than those held at $D = 2n^2 = 8a_0$, as shown by the black line. At smaller atom-surface separations, greater wavefunction overlap between the well-image-state and

the Rydberg state results in an increase in the rate of charge transfer. Also the R at which resonance occurs is shifted as the Rydberg atom moves closer to the surface with these static-atom calculations showing resonance-enhanced charge transfer at $R = 5.3a_0, 6.7a_0, 7.5a_0$. This is because as the Rydberg atom approaches the surface it is raised in energy and so is degenerate with a well-image-state in a slightly different sized nanoparticle.

Figure 3.10 depicts the energy level diagram for the $R = 5 - 10a_0$ nanoparticle at $D = 3n^2 = 12a_0$. It predicts resonance-enhancement for the $n = 2$ hydrogen atom incident at an $R = 6.7, 7.8a_0$ radius nanoparticle, which is slightly different from the maxima seen in figure 3.11. This is because figure 3.10 predicts the energy shift for a Rydberg atom approaching a flat metal surface, rather than for a Rydberg atom approaching a nanoparticle. Additionally the energy level diagram will change with atom-surface separation. However the spacings between resonances and the number of resonances match well.

3.2.5 The effect of the nanoparticle dimensions on the surface ionisation probability

The low density of states in a sphere of small radius gives a clear picture of the resonance-enhancement of charge transfer, but in reality they would be clusters just a few atoms wide, so it is necessary to carry out wavepacket propagations at larger radii, in the nanometer range. This presents a theoretical challenge, as the DVR [61] grids required to model such a system are much larger and so converging the results becomes computationally much more challenging.

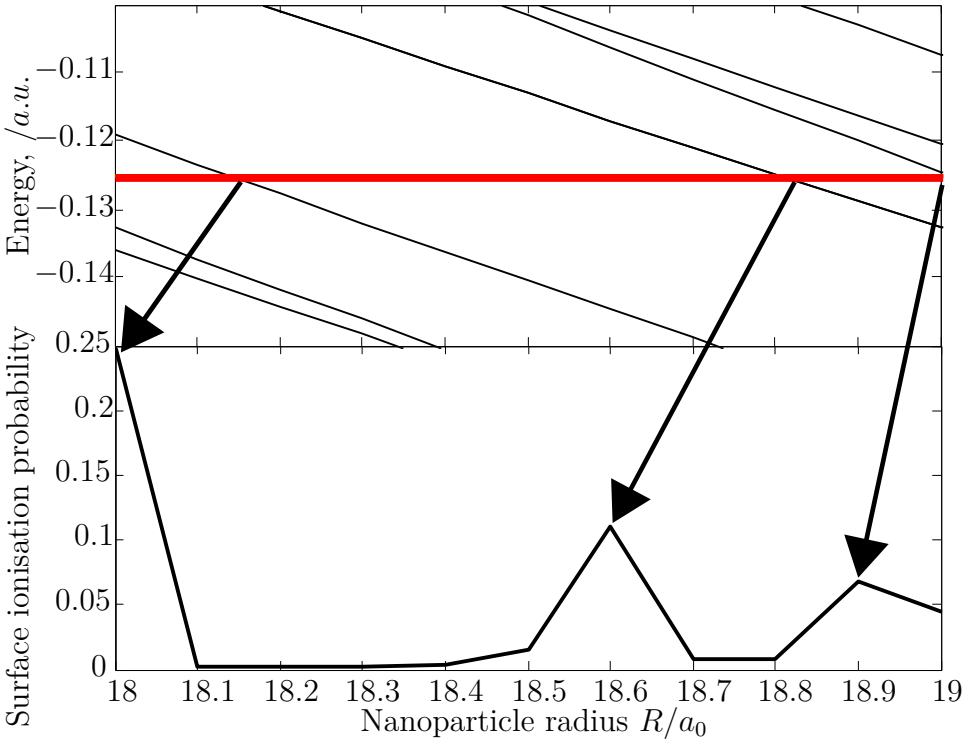

Figure 3.12: The energy level diagram and the surface ionisation probability of the $n = 2$ hydrogen atom Rydberg state and a $\phi \approx 2$nm nanoparticle calculated using a static wavepacket propagation. The arrows indicate the matching between the predicted resonances from the diagonalisations, and the positions of resonance-enhanced charge transfer from the surface ionisation probabilities.

Diagonalisations have been carried out on spheres up to $\phi = 6$nm in diameter in the absence of the Rydberg atom to show the density of states as a function of sphere radius. Figure 3.12 shows the energy level diagram and the calculated surface ionisation probability for a $n = 2$ hydrogen atom Rydberg state incident at a nanoparticle of $R \approx 1$nm. The energy level diagram predicts three resonances as the radius is finely tuned, and three peaks are seen in the surface ionisation probability. All are slightly shifted due to the change in Rydberg energy on approaching a nanoparticle.

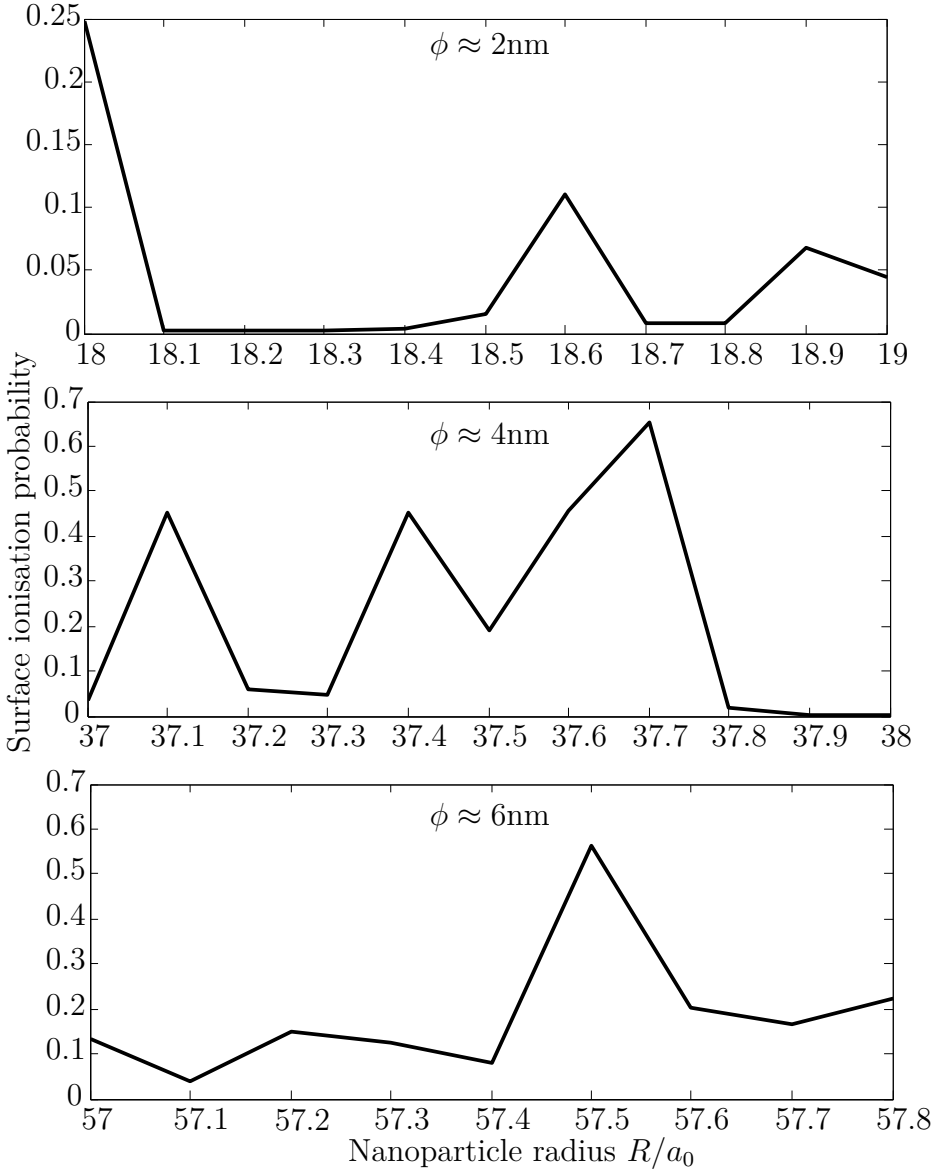

Figure 3.13: The surface ionisation probability for an $n = 2$ hydrogen Rydberg atom incident at a nanoparticle with a variable diameter around 2nm, 4nm and 6nm calculated using a static propagation method.

As shown in figure 3.13, additional static-atom propagations have been carried out in the absence of a field for jellium spheres in the range of $R = 1$nm, $R = 2$nm and $R = 3$nm. All the surface ionisation plots show resonance-enhancement of charge transfer for these nanometer scale nanoparticles. In this size range it is still possible to see resonance-enhanced charge transfer due to the degeneracy of an individual nanoparticle well-image-state and the Rydberg atom. However it is also clear that for this to be experimentally measurable, the dimensions of any sample of nanoparticles must be uniform and very well defined.

In the limit of very large nanoparticle radius the nanoparticle ceases to behave as a discrete structure and starts to behave as a bulk curved surface. As can be seen from figure 3.10 the density of the well-image states in the nanoparticle and the density of Rydberg states for a hydrogen atom are comparable, when the size of the nanoparticle and the Rydberg atom are comparable. Therefore it is expected that for larger nanoparticles resonance effects could be measured, but higher principal quantum number Rydberg atoms would be needed.

3.2.6 Dynamic-atom Calculations

The static-atom calculations are useful for elucidating pure resonant effects, but holding a Rydberg atom at a fixed atom-surface separation, where significant surface ionisation is occurring, is clearly unphysical. In the experiments described in this thesis the Rydberg atom has a velocity, and as described in the first half of this chapter, this can have a significant effect on the resultant

surface ionisation dynamics.

Once the Rydberg atom has a velocity, the perturbing surface potential evolves in time, as the magnitude of its constituent parts is dependent on the atom-surface separation, D, as described in section 1.3.2. The result is that the system no longer forms an oscillating non-stationary state in the same sense as the static-atom calculations, and the surface ionisation probability can be determined as the electron flux into the nanoparticle. The energy of the Rydberg atom changes as it approaches the surface such that resonance-enhancement will be optimal at a specific atom-surface separation. Then as the Rydberg atom continues towards the surface it will move out of resonance with the well-image state, the flow of electron back into the Rydberg atom will be minimal. In effect in the dynamic simulations actual surface ionisation can be seen. The calculations presented in this section were all carried out at $v_{\perp} = 650\mathrm{m\,s^{-1}}$.

3.2.7 Results of the dynamics calculations

Figure 3.14 shows the surface ionisation probability in black for the $n = 2$ H atom Rydberg state incident at small nanoparticles of a various selected sizes. As was the case with the propagations involving Cu(100) in the section 3.2.4 the surface ionisation probability is the flux of electron density into the surface, or in this case the jellium sphere. In the copper case, for on-resonance states the surface ionisation probability maximum is at a much larger atom-surface separation than the off-resonant case. This results in more surface ionisation occurring, and the ions produced through surface ionisation being

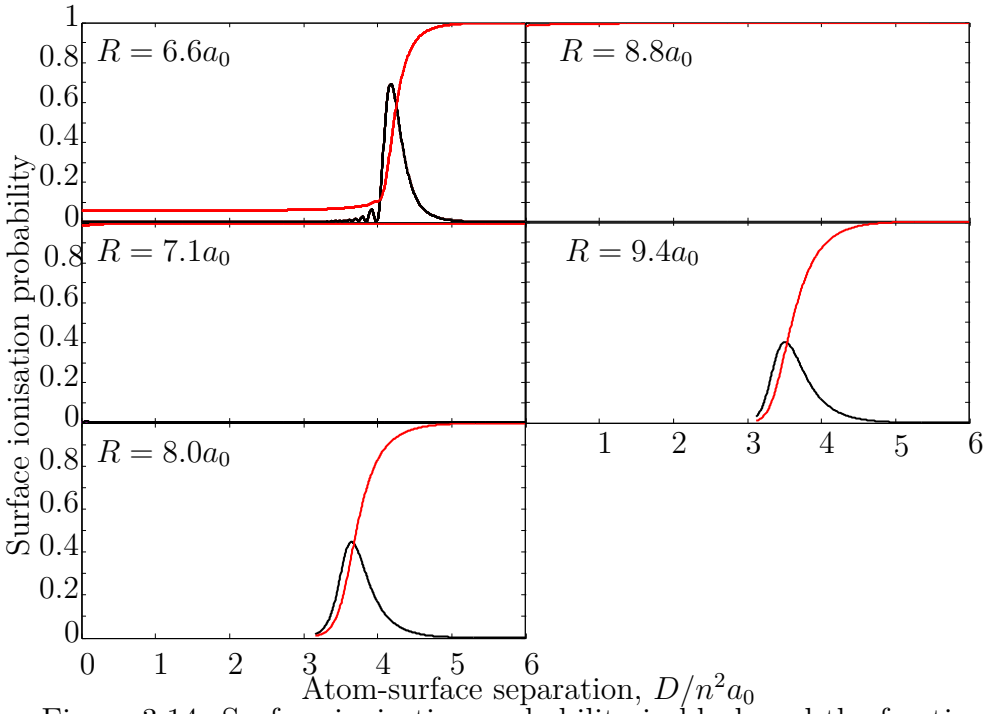

Figure 3.14: Surface ionisation probability in black and the fraction of the electron localised on the atom in red for a small nanoparticles between 0.25nm and 0.5nm in radius. These radii have been selected as they represent the minima and maxima in the plot of surface ionisation probability as a function of radii. Note that $7.1a_0$ and $8.8a_0$ have very low surface ionisation probability and so the ionisation fraction is very small.

more detectable. In the nanoparticle case however there is an additional effect, in that the total surface ionisation probability is far smaller for off-resonant states, than on-resonance. In effect the non-degenerate Rydberg atoms do not surface-ionise closer to the surface as in the copper case, but actually do not surface ionise at all. The propagation at $R = 7.1a_0$ and $R = 8.8a_0$ show this very characteristic off-resonance behaviour. In the nanoparticle case, unlike the projected band gap surface case, there are no higher angular momentum (parallel momentum) states in perpendicular metallic continuum, and so when the Rydberg atom is off-resonance the electron cannot penetrate

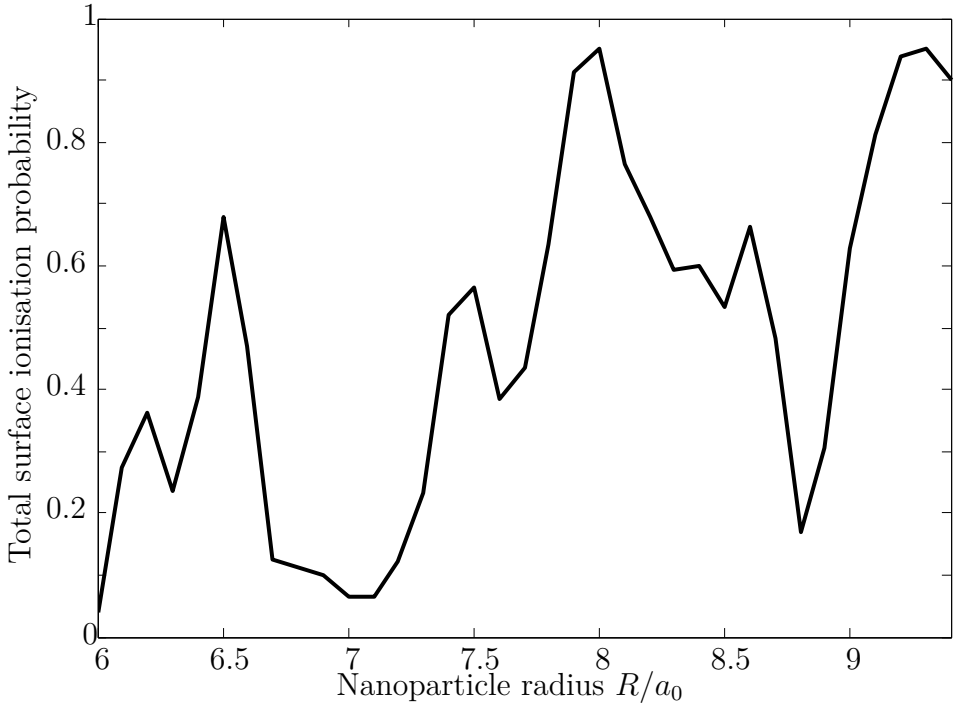

Figure 3.15: The total surface ionisation probability of the $n = 2$ hydrogen Rydberg atom at a small nanoparticle of variable radius, determined by integrating the surface ionisation probability over all possible atom-surface separations.

into the nanoparticle at all.

The red lines in figure 3.14 depict the fraction of Rydberg electron density localised on the Rydberg atom, such that a value of one indicates no surface ionisation, and a value of zero represents full surface ionisation. For a metallic surface, even one with a projected band gap, ultimately this measure would show significant surface ionisation when the atom gets close enough to the surface, whereas in the fully confined nanoparticle that is not the case. As can be seen from the unchanged fraction of ionisation of the $n = 2$ hydrogen Rydberg atoms propagated at nanoparticles with radius $7.1a_0$ and $8.8a_0$ there is no surface ionisation and the fully localised Rydberg wavepacket crashes

into the nanoparticle. The lack of surface ionisation can be understood as there is no state degenerate in energy with the Rydberg atom localised in the nanoparticle, even a higher angular momentum state.

Figure 3.15 shows the total surface-ionisation probability, calculated by taking the integral of the surface ionisation probability over all atom-surface separations. Resonance-enhanced charge transfer is seen at $R = 6.5a_0, 8a_0, 9.5a_0$. The same size-range of nanoparticles are used in these dynamic calculations, as in the static-atom calculations in section 3.2.4, so figure 3.15 is directly comparable with figure 3.10. However resonance-enhanced charge transfer from the $n = 2$ hydrogen atom Rydberg state to the nanoparticle occurs at slightly different radii for the two sets of calculations. This is due to the energy change of the Rydberg atom as it approaches the nanoparticle as described in section 1.3.3. The situation in the dynamic case is complex, as the Rydberg energy changes with atom-surface separation such that at different times in the wavepacket evolution the energy gap between the Rydberg and the well-image-state is different. The atom-surface separation tunes the hydrogen Rydberg atom energy, and the nanoparticle radius tunes the well-image-state energy, such that resonance-enhanced charge transfer can occur for different sized nanoparticles at different atom-surface separations. However ultimately this effect is limited, as the energy shift on approaching a surface is small, and the greater the atom-surface separation required for optimal energetic overlap, the worse the spatial wavefunction overlap is.

For on-resonance Rydberg atoms, where the energy of the electron matches the energy of the nanoparticle localised well-image state, the electron can surface ionise and pass into the metal. However for the off-resonance states

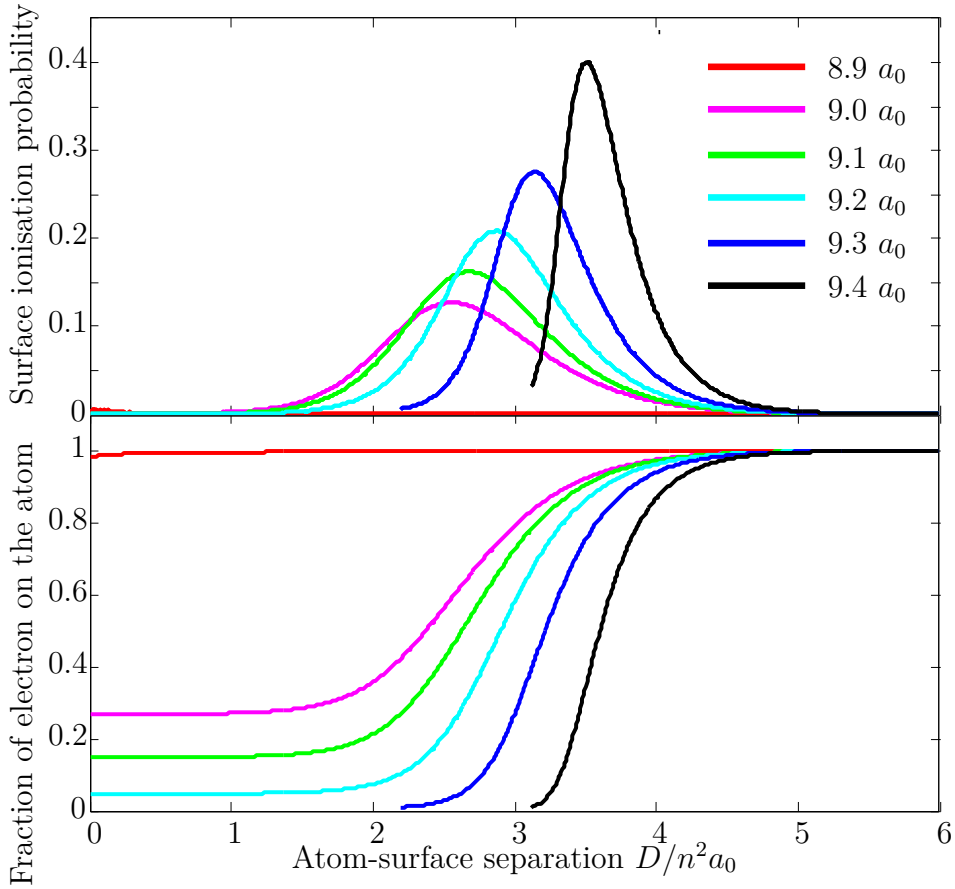

Figure 3.16: Surface ionisation probability and fraction of the electron on the atom for $n = 2$ hydrogen atom Rydberg states and a nanoparticle of variable radius of $R \approx 0.5$nm. $8.9a_0$ is off-resonance and $9.4a_0$ is on-resonance.

the electron wavepacket does not deplete on approach to the surface and so the Rydberg atom crashes into the surface. This behaviour is characteristic of a totally confined system, and has not been seen before in theoretical Rydberg-surface studies.

Figure 3.16 depicts the surface ionisation probability and fraction of electron on the Rydberg atom of a $n = 2$ hydrogen atom incident at a small nanoparticle of approximately 0.5nm radius. The radius is tuned in steps of

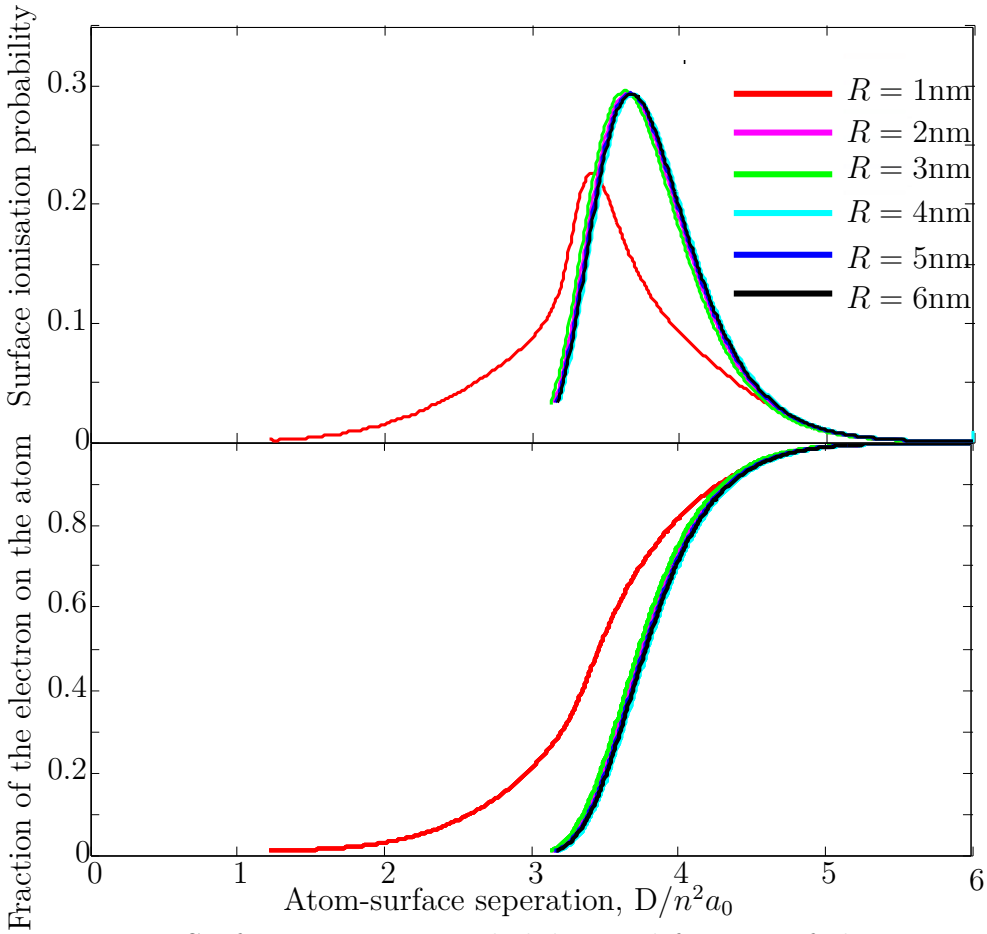

Figure 3.17: Surface ionisation probability and fraction of electron on the Rydberg atom for $n = 2$ hydrogen atom Rydberg states incident at a series of nanoparticles with experimentally accessible diameters. The given nanoparticle dimension is the diameter.

$0.1a_0$ to show the evolution of a resonance with radius, and therefore with the nanoparticle well-image-state energy. The increased surface ionisation probability, at larger atom-surface separations, for the $R = 9.4a_0$ nanoparticle is due to the better energy matching of the Rydberg state and the well-image-state, than in the other propagations.

Like in the static-atom case, the nanoparticles investigated so far using dynamic wavepacket propagations have been too small to be experimentally

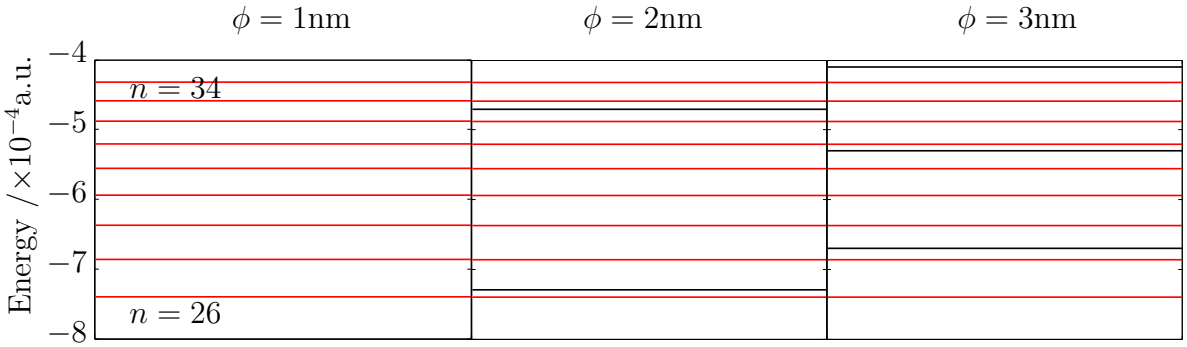

Figure 3.18: Energy level diagrams for a nanoparticle of $\phi = 1$nm, 2nm, 3nm with the experimentally accessible $n = 26 - 34$ Rydberg energy levels calculated from equation 1.13. The red lines depict the Rydberg atom energies and the black lines the well-image-state energies.

viable as spherical particles. Therefore dynamic propagations were carried out with a $n = 2$ incident at series of nanoparticles with diameters on the nanoscale. The $\phi = 2, 3, 5, 6$nm propagations all show resonance-enhanced charge transfer at $D = 3.8n^2$ and full surface ionisation of the electron wavepacket. However the $n = 2$ Rydberg atoms incident at the $\phi = 1$nm nanoparticle, shows a lower rate of surface ionisation, and appears to be more off-resonance. However in this case, there is still some significant depletion of the wavepacket, suggesting that due to the greater density of states in these larger nanoparticles, not only is it less likely to find an off-resonance nanoparticle, but the neighbouring well-image states will still be significantly closer in energy than in the small nanoparticle limit. The $n = 2$ H atom Rydberg state is far smaller than the nanoparticles investigated here, such that the density of states in the nanoparticle at the appropriate energy level are likely to be closely spaced.

3.2.8 Comparison to Experiment

In the Softley group, experiments have previously been carried out to investigate the interaction of H atom Rydberg states with a principal quantum number of $23 < n < 35$ and a monolayer of gold nanoparticles of radius $5\text{nm} - 10\text{nm}$ laid down on a silicon wafer [80]. These experiments showed a tendency for blue shifted Rydberg atoms of the n manifold to switch k states to the red shifted $(n+1)$-manifold. However these experiments also outlined the difficulty in working with nanoparticles, whereby surface preparation is difficult to control. The solvents required for deposition modify interaction potentials, a uniform coverage was not achieved such that clustering of nanoparticles and exposed substrate was seen and the nanoparticles were not of a uniform size. Ultimately the preparation of nanoparticle surfaces outside the vacuum lead to sample degradation and uncertainty which caused repeatability issues in the measurements. In these calculations no evidence has been seen for the k state change on approaching a nanoparticle, which would be expected to manifest itself as a change in localisation of electron density as the Rydberg atom approaches the surface. However it is possible that the k-state change is a result of glancing collisions between the Rydberg atom and the nanoparticle which have not been studied here.

In an attempt to circumnavigate the experimental difficulties of the nanoparticle measurements, but still looking for the confinement effects described in this chapter, the interaction of Rydberg atoms and thin films was investigated experimentally instead. In such a system there is one-dimensional confinement as opposed to three-dimensional but work from my part II thesis

suggested such a system should yield resonance effects in charge transfer [79]. By installation of an evaporator onto the surface-analysis chamber thin films can be prepared cleanly in situ and characterised before Rydberg-surface experiments occur, so that the high level of surface control required to observe the resonance effects described in this section is possible.

Figure 3.18 shows the energy level diagram for the experimentally accessible hydrogen atom Rydberg states $n = 26-34$ and three experimentally viable nanoparticles. Experimentally instead of tuning the radius of an individual nanoparticle, a range of Rydberg atoms with different principal quantum numbers would be scattered from the same nanoparticle surface. These calculations predict no resonant principal quantum numbers in the $\phi = 1$nm case, $n = 33, 26$ resonant when incident at a surface of $\phi = 2$nm nanoparticles and $n = 34, 31, 27$ resonant at the $\phi = 3$nm nanoparticle surface.

3.2.9 Conclusions

To conclude, the calculations presented in this section show resonance-enhanced charge transfer between a hydrogen Rydberg atom and a degenerate well-image-state in a nanoparticle. Diagonalisations show that as the nanoparticle increases in size its well-image states become closer together in energy, and have greater well-state character. Ultimately with infinite radius, the limit of a flat metallic surface is reached. Due to the computational expense of the wavepacket propagation calculations involving a confined potential, the calculations in this section are limited to $n = 2$ hydrogen Rydberg atoms and small nanoparticles. However it is expected the predicted effects will occur in

larger nanoparticles and experimentally accessible Rydberg atoms, but that the control required over the size and distribution of the nanoparticles would make this difficult to measure.

Chapter 4

Experimental details

4.1 Investigating the Rydberg surface interaction

The experimental setup to measure the H atom–surface interactions is described in this chapter. In brief, H atoms are formed by photolysis of a supersonic beam of NH_3 at 193nm, in a capillary mounted on a pulsed nozzle. Using a pure NH_3 beam, the H atoms travel 46cm to the laser excitation point where the high-n Rydberg states are populated by two-colour ($\lambda_1 = 121.57$nm, $\lambda_2 = 365.75$ to 366.75nm) two-photon excitation via the 2p intermediate level. The excitation occurs in a large enough field to allow selection of a particular Stark state of the n-manifold. The Rydberg atoms then travel 3mm to interact with the surface which is mounted at a 15° incidence angle with respect to the atom beam. The surface can be moved under vacuum to a surface-analysis chamber where Low Energy Electron Diffraction (LEED) and

X-ray Photoelectron Spectroscopy (XPS) are used to determine the elemental composition, crystal plane and presence of impurities on the surface.

Figure 4.1 depicts the experimental setup of the main experimental chamber. Within this chamber, the hydrogen Rydberg surface ionisation experiments are carried out. The following subsections describe the experimental setup in this chamber. It is crucial that the surfaces used in the Rydberg surface ionisation experiment are well prepared and characterised. Therefore the experiment has a second vacuum chamber, described in section 4.2, dedicated to surface preparation and analysis. The surface can be moved under vacuum between the surface analysis chamber and the main experimental chamber by an xyz rotatable manipulator.

4.1.1 Production of the Hydrogen atomic beam

Hydrogen atoms are produced by photodissociation of ammonia using an ArF excimer laser (GAM Ex5, 193nm, 10Hz, $\sim$ 8ns pulse width, $\sim$ 5mJ per pulse). The molecular beam has a backing pressure of $\sim$ 2bar and can be either pure ammonia or seeded in a rare gas, depending on the velocity range of interest. The beam of Ammonia is pulsed at 10Hz using a pulsed-solenoid valve (General Valve, Series 9) giving an initial gas pulse duration of $\sim$ 100µs. The pressure of pure ammonia in the source chamber is $\approx 5 \times 10^{-6}$mbar. As shown in figure 4.1 the molecular beam then passes through a 15mm long, 1mm inner diameter quartz capillary (Vitrocom CV1012S) attached to the face plate of the valve, where photodissociation occurs. The 193nm laser pulse is weakly focused by a fused silica spherical lens with $f = 200$mm

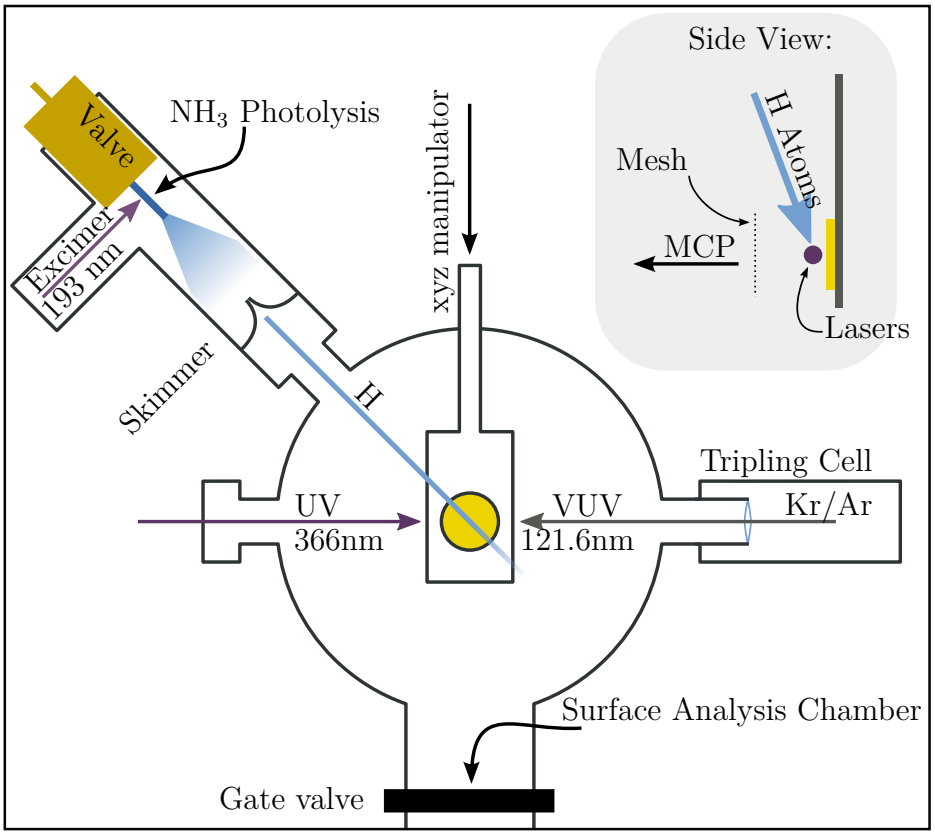

Figure 4.1: Schematic experimental setup of the main experimental chamber of the hydrogen Rydberg surface ionisation experiment.

onto the middle of the quartz capillary to photodissociate $NH_3 \rightarrow NH_2 + H$. Photodissociation occurs in the capillary so that the high energy fragments are collisionally cooled. After exiting the capillary, the gas packet expands, and $\sim$ 3cm later it passes through a skimmer, of diameter 1mm, into the main chamber. The advantage of using the photodissociation method of Willitsch *et al* to produce the radical beam, as oppose to say a microwave discharge, is that the H atoms produced are collisionally cooled in a supersonic jet [82]. This cold beam allows better velocity discrimination during the Rydberg surface ionisation experiments.

4.1.2 Making hydrogen Rydberg atoms

Once the hydrogen radical beam has passed into the main chamber there is a free flight region of ~ 46cm. The hydrogen atoms are excited to the desired Rydberg state using two tuneable, side-pumped Nd:YAG (Continuum Surelite III, 532nm, ~ 430mJ, ~ 9nm pulse width, 10Hz) Sirah Cobra-Stretch dye lasers. The first beam (pyradine 2 dye, ~ 8mJ per pulse) is focused into a tripling cell by a $f = 150$mm fused silica lens. The tripling cell contains a rare-gas mixture of 25% (250mbar) Krypton and 75% (700mbar) Argon, at a pressure of ~ 950mbar. The frequency tripling process is inefficient, with the ratio of UV:VUV photons approximately $1 : 10^{-5}$ [83]. Four wave mixing of the 364.8nm doubled dye laser light produces a VUV beam at 121.6nm (Lyman-α), which is focused onto the hydrogen atom beam by a $f = 150$mm lithium fluoride lens. This excites a hydrogen atom from the ground state to the 2p state. A second counter-propagating frequency-doubled UV laser (Styryl 8 dye, ~ 8mJ per pulse) then excites to any Rydberg state up to the ionisation limit by tuning over the range $367\text{nm} \geq \lambda \geq 365.5\text{nm}$. The upper limit of the density of Rydberg atoms is $\approx 3 \times 10^5$, calculated using a one photon cross-section for the $1\text{s} - 2\text{p}$ transition of $8 \times 10^{-17}\text{cm}^2$ [84], a photon-beam interaction length of 0.1cm, a hydrogen beam density of 10^{11}cm^{-3} and a VUV photon density of 4×10^{10}.

4.1.3 Velocity control

As described in section 3.1 the perpendicular collisional velocity of the incident atomic beam of H atoms has a significant effect on the surface ionisation

dynamics. The resonance effects seen in the experimental results presented in chapters 5 and 6 have been enhanced by varying the collisional velocity of the atomic beam. After the atomic beam has expanded out of the capillary there is a free flight region 46cm in length. In the laser excitation volume, at the end of the free flight region, the molecular beam is sufficiently expanded such that the fastest atoms arrive first. By altering the firing time of the Rydberg excitation lasers, with respect to the excimer laser trigger pulse, a different velocity of hydrogen Rydberg atoms can be sliced out. Experimentally, the delay between the excimer trigger and the Q switch can be changed by up to a 300µs. The velocity resolution is approximately 1%, and this is due to the width of the excimer pulse.

In all of the experimental work presented in this thesis unseeded ammonia is used. This allows a perpendicular collisional velocity along the surface normal of between $850\mathrm{m\,s^{-1}}$ and $500\mathrm{m\,s^{-1}}$, as the angle between the hydrogen beam and the surface is 15°. By seeding the ammonia in heavier or lighter noble gases this velocity range can be increased significantly [25]. The time between excitation and interaction with the surface is approximately 0.5µs, which is significantly less than the lifetime of the experimentally accessible Rydberg atoms [12].

As shown in figure 1.6, the beam of hydrogen Rydberg atoms arrives at 15° from the surface. By varying the delay between the excimer and the Q switch by $180 - 300$µs, the longitudinal hydrogen beam velocity is $2800 - 1600\mathrm{m\,s^{-1}}$ and the perpendicular collisional velocity along the surface normal is $850 - 500\mathrm{m\,s^{-1}}$. Therefore the velocity dependence of the ionisation dynamics could also be investigated by varying the hydrogen beam angle with

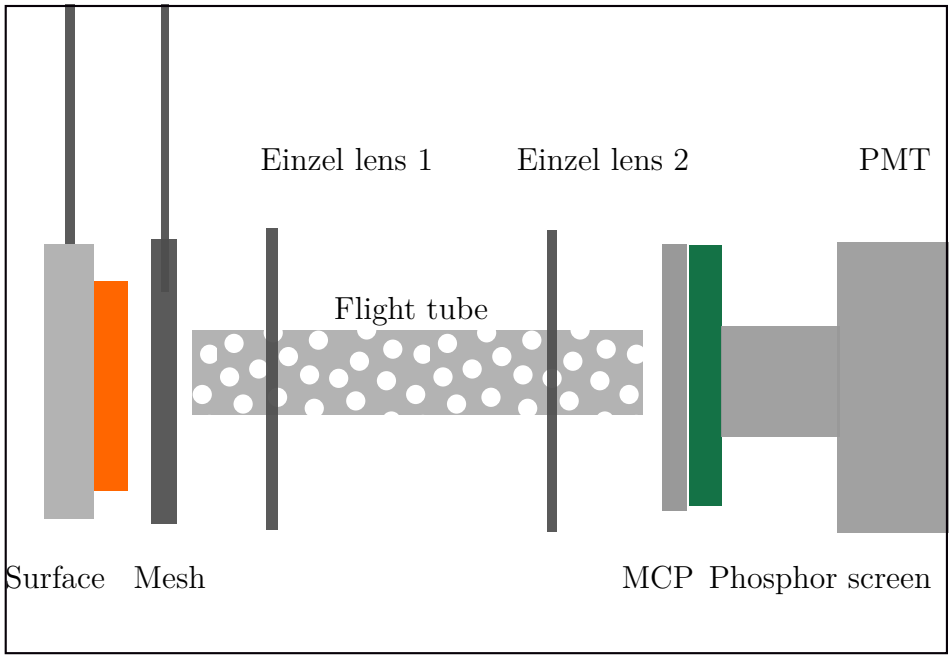

Figure 4.2: Schematic of the detection setup for ion extraction and detection.

respect to the surface. This is possible as the whole surface and detection setup can be rotated with respect to the beam, such that the perpendicular velocity component can be changed without altering the delay between the excimer and the excitation lasers. Furthermore, current experimental work in the laboratory is underway to put a Rydberg-Stark decelerator in the atomic beam path to increase the velocity range further.

4.1.4 Ion extraction and detection

The surface ionisation signal is measured by extracting the ions produced via surface ionisation as described in section 1.3.4. In the standard ion-extraction mode the surface is grounded and a negative voltage is applied to the mesh. The detection setup is shown in figure 4.2. The mesh and the surface are

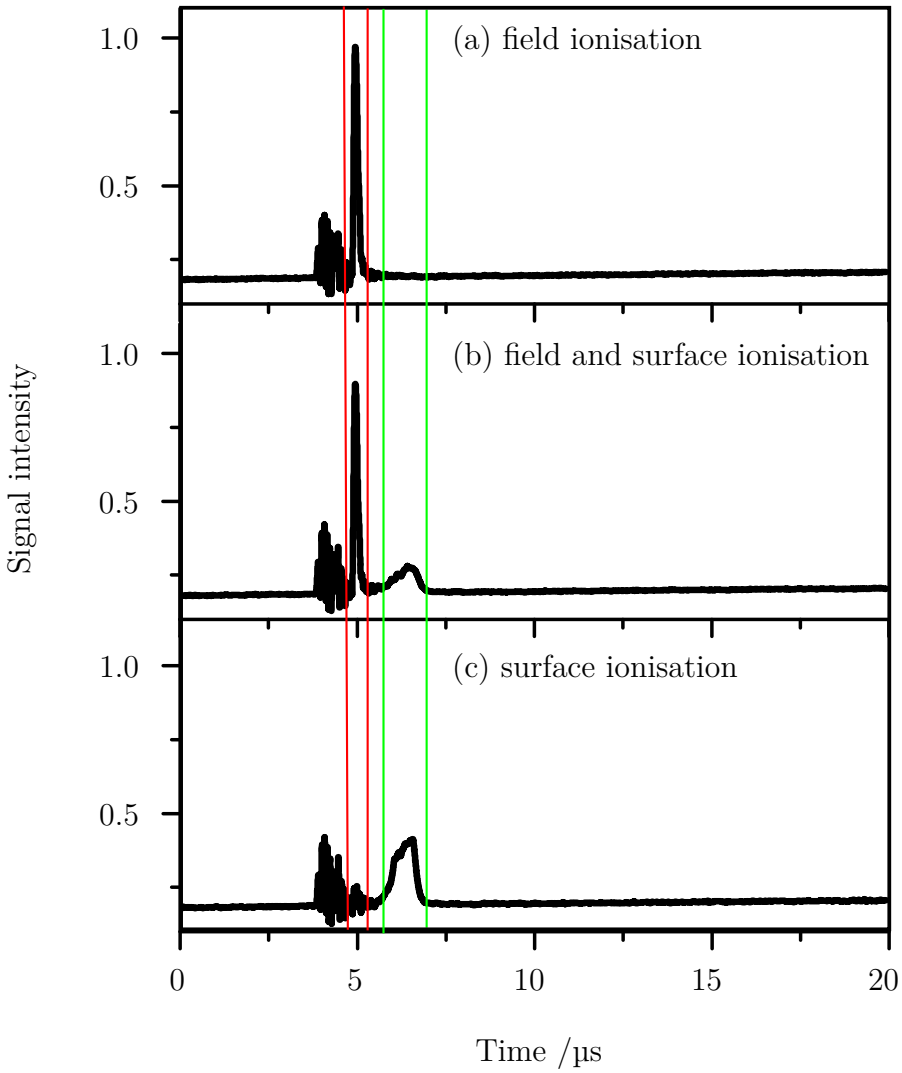

Figure 4.3: Typical time of flight traces showing the field ionisation signal in red gates and the surface ionisation signal in green gates for the $n = 30$ hydrogen atom Rydberg state. The applied field is (a) 1200V cm^{-1}, (b) 800V cm^{-1} and (c) 600V cm^{-1}.

approximately 1.5cm apart, and this can be calibrated by fitting the Stark manifold spectra of a given Rydberg atom. Electron detection is also possible, but not used in this thesis [25, 85]. A flight tube at a potential of −1300V, with two Einzel lenses guides the beam of ions onto the microchannel plate stack at −1200V, and the resulting amplified electron signal is imaged by a phosphor screen at −3000V. A photomultiplier tube converts this light to the time-dependent signal recorded on the oscilloscope. Optimisation of the detection setup is described in the following subsection.

A typical time of flight trace is shown in figure 4.3. Ions resulting from field ionisation arrive earlier on in the time-of-flight trace as a sharp feature, and those from surface ionisation arrive later in time as a broader feature. This is because field ionisation produces ions instantaneously, whereas at lower fields the Rydberg atom continues towards the surface before being surface ionised, and ultimately extracted at a later time and over a range of distances. The figure also shows that the magnitude of the applied field determines whether Rydberg atoms are field or surface ionised, with a small intermediate region where both signals are observable. The red and green lines in figure 4.3 show the time gates over which the field- and surface-ionisation signal are integrated, respectively.

The whole experiment is pulsed at 10Hz and the integrated field and surface ionisation signals are recorded over a series of extraction fields. The magnitude of field applied to the mesh is decreased by 10V every 10 shots, and over the same time period the oscilloscope records the average of the integrated ion signal between the gates. The measurement of the surface ionisation signal as a function of extraction field produces the 'surface ionisation profile'.

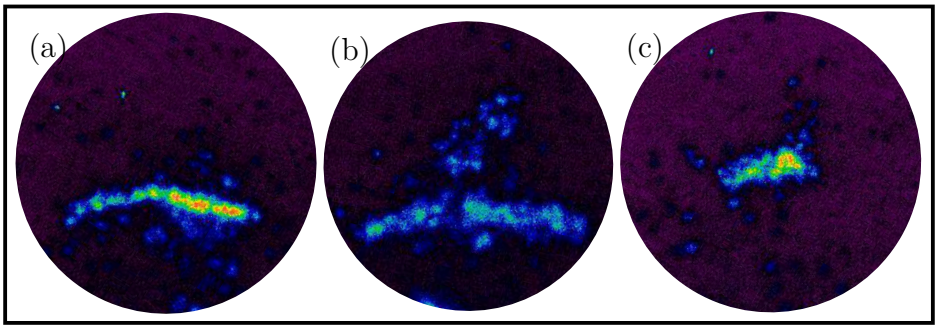

Figure 4.4: The spatial distributions of the ions extracted from (a) field ionisation and (b) both field and surface signal and (c) surface signal. The detectable area shown is determined by the presence of a shield in front of the MCPs. The applied field is (a) 1200V cm^{-1}, (b) 800V cm^{-1} and (c) 600V cm^{-1}.

Alternatively, a CCD camera in place of the PMTs can be used to image the location of the detected ions at the MCP plates. This allows the field and surface signals to be resolved by their distinct spatial location, as opposed to in the time of flight mode which provides temporal resolution.

4.1.5 Focusing the ion beam

The ions formed by surface and field ionisation are produced at different locations, as shown in figure 1.6. The detection setup consists of two Einzel lenses [86] and a Wiley McLaren time of flight setup [87] which needs to be optimised to capture the ions produced at these distinct locations. Typically Wiley McLaren time of flight is used to optimise the mass resolution for time-of-flight mass spectrometry. In this case it is implemented to optimise the differentiation between our field- and surface-ionisation signals. Additionally the detection setup has to be able to compensate for the presence of different

extraction fields without changing the detection efficiency.

The first ion lens can focus and deflect, depending on the applied voltages and the alignment of the experiment. Such that if ions are being produced on the edge of the detection region because of poor laser alignment, changing the voltage applied to first ion optic can result in a signal being measured or not. Once all other experimental parameters have been optimised a CCD camera is used to find the optimal voltage on the first ion lens to focus the surface-generated ions onto the centre of the detector, whilst monitoring the size of the time-of-flight signal. This process is repeated for all the extraction voltages, to determine a linear ramp in the voltage of the first ion optic as a function of extraction field. For example if the applied voltage is given by F_{ext}, and the voltage applied to the first ion optic is F_{O1}, then the ramp is typically $F_{\mathrm{O1}} = (800 + 0.05F_{\mathrm{ext}})\mathrm{V\,cm^{-1}}$. This linear ramp is put into the control program and the first ion optic voltage is changed automatically as the extraction field is ramped.

The second ion optic is fixed at the flight tube voltage. This is because using the second optic as an Einzel lens has resulted in preferential detection of ions produced by one-colour hydrogen atom signal, which masks the field ionisation signal. This one-colour hydrogen signal is likely to be from a VUV photon and a UV photon of untripled laser-light.

Figure 4.4 shows the field and surface ionisation signals on the aperture. The Einzel lens is optimised so the surface ionisation signal is more focused, and using the same voltages a 'stripe' of field ionisation signal is seen. However the field ionisation signal, which is measured in order to provide a normalisation factor for the molecular beam density and laser power fluctuations, is

sufficiently centred and focused to provide a reliable normalisation constant.

4.1.6 Signal optimisation

In order to find a measurable two-colour Rydberg hydrogen atom surface ionisation signal several steps were first necessary. Acetone is a strong and broad absorber in the VUV [88]. Initially $(1+1)$-REMPI of acetone seeded in helium beam was carried out. Optimisation of the one-colour signal resulted in optimisation of the tripling cell gas concentration, the internal UV dye laser alignment and the beam position through the silica lens and into the tripling cell. Afterwards a beam of hydrogen was produced as described above, and a one-colour signal was optimised at the Lyman-α. This signal was sensitive to both the VUV wavelength and the relative positioning of the radical beam and VUV beam in both time and space. After optimisation for the maximum one-colour hydrogen signal, the second UV laser is introduced to excite to a Rydberg state. Optimisation of the ion optic voltages and alignment of the UV laser to give the best possible field ionisation signal is required before looking for surface signal. Primarily moving the surface, and optimising the ion optics should allow the surface ionisation signal to be found, after which optimisation the final optimisation of all the other parameters can occur.

4.2 Surface analysis facilities

The second chamber, as shown in figure 4.5, allows surfaces to be produced, prepared and analysed in situ. This is advantageous as the elemental composition, plane, flatness and the presence of any impurities on the surface

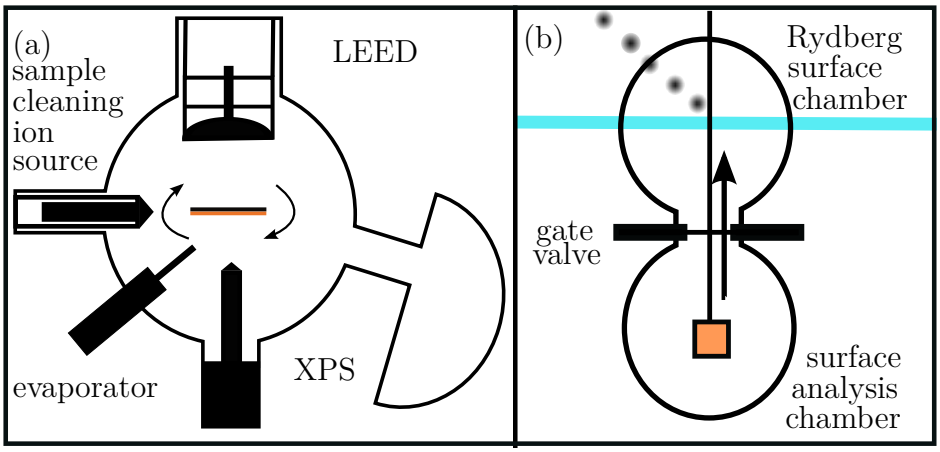

Figure 4.5: (a) Schematic of the surface analysis chamber. (b) The xyz manipulator allows the surface to be moved between the surface analysis chamber and the Rydberg surface experiment under vacuum.

have a significant effect on the surface ionisation dynamics observed in the Rydberg surface experiment as shown in chapter 5.

As shown in figure 4.5b, the two chambers are connected with a gate valve, and the surface is mounted on an *xyz* rotatable manipulator (2cm x-axis translation range, 70cm y-axis translation range, 2cm z-axis translation range, 360°, manufactured by PSP Vaccum) that can pass into either chamber and position the surface at the required position for the particular experimental technique.

The surface analysis equipment (LEED, XPS) is calibrated using an air cleaved Mica crystal, known as muscovite. In this thesis two distinct types of surface are used: the first a single-crystal Cu(100) surface and the second a series of iron thin films on a muscovite base.

4.2.1 Sample cleaning ion source

After a single crystal has been prepared externally and placed into the vacuum it is likely to be covered with adsorbates. From XPS, it can be determined that these adsorbates predominantly contain carbon and oxygen, however a large background in the XPS signal supports the presence of additional impurities. In order to remove these impurities and produce a clean metallic crystal, sputtering is required. A voltage is applied to a beam of argon atoms until a discharge is struck and then a beam of argon ions is accelerated at 500eV towards the metal, knocking adsorbates off and producing a clean, if cratered, surface. The spot size of the ion gun is $\approx$ 1cm, as determined by XPS. The ion source is the ISIS3000 as supplied by PSP vacuum.

4.2.2 Sample heater

Annealing a metallic single crystal involves heating it up to two–thirds of its melting point, allowing thermodynamic restructuring of the crystal plane into an atomically flat surface. However, annealing pushes impurities out from within the bulk crystal and onto the surface such that cleaning is required and the process has to be repeated numerous times. These repeated sputtering and annealing cycles prepare flat and clean metallic surfaces from a single crystal prepared out of vacuum [89]. The duration and number of cycles required depends on the composition and condition of the single-crystal, however sputtering for 20min, annealing for 30min and repeating the whole cycle twenty times is typical.

A resistive heater mounted under the surface comprises of five fingers

formed of four strands of 0.125mm diameter tantalum wire, coated in a insulating ceramic. Passing a maximum current of 4.5A heats the surface up to a maximum of 750°C and the temperature is monitored via a thermocouple attached to the sample mount. An external controller allows the desired temperature to be set, and provides a feedback loop to maintain a given temperature. Initially the current is slowly ramped up over a period of several hours to prevent burning of the wires, as the cool wires have large resistance. The heater was custom built by PSP Vacuum.

4.2.3 Low energy electron diffraction

Low energy electron diffraction (LEED) is surface sensitive as the slow electrons which are scattered from the metallic surface have a low penetration depth. The resulting diffraction pattern arises from electrons which have penetrated typically tens of monolayers only. LEED patterns are only measurable from a clean and flat surface.

An electron gun produces a beam of electrons with energy between $5\text{eV} - 750\text{eV}$ that diffract within the metallic crystal and form a characteristic diffraction pattern on a phosphor screen. This diffraction pattern allows the plane of the crystal to be determined, or in the case of a prepared single crystal, to be confirmed.

LEED is more complex to model than x–ray diffraction (XRD) due to the large free–atom electron scattering cross sections, which can be 10^{10} times the size of free–atom x–ray cross sections [90]. This means multiple scattering events and inelastic collisions have to be accounted for, and a

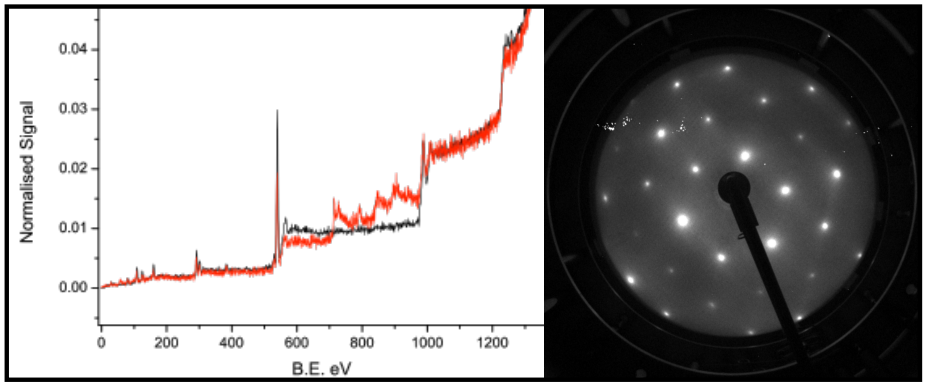

Figure 4.6: Mica characterisation of the LEED and the XPS

kinematic theory, similar for that used in XRD, is not suitable. Even for elemental single crystals the situation is complicated, as each symmetrically distinguishable atom within a unit cell requires a different free–atom electron cross section to correctly predict the multiple scattering events, and therefore model the experimental diffraction pattern and intensities correctly [90].

However, in the context of the experiments presented in this thesis the LEED pattern is primarily used to confirm the crystal plane of a sample, and the intensity of the spots used to determine the preparation of a clean, flat surface [89]. For both of these purposes comparison of the measured diffraction pattern to one in the literature is sufficient, so intensity modelling of our surfaces has not been carried out. The setup combines a Integraleed BDL600IR, with the LPS075-D control unit which was manufactured by OCI vacuum microengineering and supplied by PSP vacuum.

4.2.4 X-ray photoelectron spectroscopy

X-ray photoelectron spectroscopy (XPS) is used to determine the elemental composition of a sample. A beam of x-rays is fired at a surface, ejecting electrons from within the inner-shell atomic energy levels via the photoelectric effect. The kinetic energy of these electrons is measured using a hemispherical electron analyser.

$$E_{\text{binding}} = \frac{hc}{\lambda} - E_{\text{kinetic}} - \phi \tag{4.1}$$

where E_{binding} is the binding energy of the electron, E_{kinetic} is its kinetic energy, ϕ is the surface–dependent work function and λ is the wavelength of the x-rays used to irradiate the surface. The elemental composition is determined by comparing the experimental binding energies to tabulated values. As these involve core-level ejection the energies involved are largely independent of the material, but dependent on the elements present. The stoichometry can be determined by intensity analysis as outlined in section 6.3.2, by approximating the escape depth of the electrons. The x-ray source has twin anodes to allow XPS spectra to be measured at the Mg k_α (1254eV) and the Al k_α (1487eV). On a binding energy scale, XPS peaks are constant as the filament is changed. Auger peaks move, as they measure the kinetic energies of electrons ejected after relaxation of higher energy electrons into atomic core holes. The CTX400 twin anode x-ray source, with Mg and Al anodes is used in conjunction with a hemispherical electron analyser, all provided by PSP vacuum.

4.2.5 Electron beam evaporator

For production of thin films in situ, an EF3 omnicron GMBH electron beam evaporator with an integrated flux monitor is used. The evaporator uses a flux of electrons to heat up an evaporant rod, and produces a significant flux of evaporant atoms towards a substrate. The integrated flux monitor measures the flux of evaporant out of the evaporator and removes the need for a quartz microbalance. Due to space constraints in the surface analysis chamber, the evaporator had to be mounted on the central axis, such that only rod evaporants can be used. Rod evaporants require a metal with a high vapour pressure such that a measurable ion flux can be produced whilst maintaing the rod's structural integrity. This limits the materials we can use in the current setup, and is the main reason thin films of iron were produced as described in chapter 6.

4.2.6 Characterisation with Muscovite

Muscovite, a mica derivate, cleaves in air to produce a perfect (001) crystal plane. Once placed in vacuum, the crystal can be used as a test substrate to characterise the surface analysis chamber. without requiring preparation of a clean and flat surface. Figure 4.6 shows the XPS spectrum and LEED pattern of muscovite. The black XPS line shows all the characteristic muscovite peaks with a spectrometer-dependent work function of $\phi = 7$eV. The red line shows the XPS with additional iron peaks, after evaporation of an iron film. Again, a work function $\phi = 7$eV is required to fit the curves to the tabulated values [91]. The LEED pattern at 83eV shows the characteristic

six-fold symmetry of a muscovite surface. The pseudo-hexagonal diffraction pattern with alternating spot intensity matches literature diffraction patterns well [92].

4.3 Maintaining operating pressures

The surface analysis chamber operates at a pressure of 1×10^{-9}mbar or better (Pfeiffer HiPace 300M turbomolecular pump backed with a Pfeiffer Duo 5M rotary pump), and is baked after opening at 150°C. At higher pressures the rate of surface degradation rapidly increases and the LEED diffraction patterns have a larger background contribution.

The pulse valve is in a source chamber at 2×10^{8}mbar (Pfeiffer TMU521 turbomolecular pump backed with a Pfeiffer Duo 20M rotary pump) and the hydrogen atom beam is produced and skimmed in a differentially pumped system (Pfeiffer TMU0071P turbomolecular pump backed with a Pfeiffer Duo 20M rotary pump). The radical beam passes into the main chamber which is at a base pressure of 1×10^{-8}mbar (Pfeiffer TMU521 turbomolecular pump backed with a Pfeiffer Duo 20M rotary pump).

Chapter 5

Ionisation of Rydberg atoms at a Cu(100) surface

As described in section 3.1 the Cu(100) surface has a projected band gap at the energy range of the $n = 25-34$ hydrogen Rydberg atoms. The $n = 25-34$ hydrogen atom Rydberg states are chosen for study as they have radiative lifetimes longer than the duration of the experiment, and are stable enough with respect to field ionisation that a broad range of external fields may be applied to extract the ions from surface ionisation. In this chapter the role of the electronic structure of the surface on the resonant charge-transfer process is investigated. In particular we probe the extent to which degeneracy between the Rydberg energy level and the image-states of the surface affects the charge transfer dynamics.

Unlike fully metallic surfaces, where the Rydberg electron energy is degenerate with the conduction band of the metal, in the Cu(100) surface only discrete image-states are available through which charge transfer can take

place.

5.1 Previous studies

Surface and image charge states have been studied experimentally for a number of materials using various techniques including two-photon photoemission [41], inverse photoemission [37] and scanning tunnelling spectroscopy [48] as described in section 1.6.2. The $4 \leq n_{\text{img}} \leq 9$ image-states of the Cu(100) surface have been studied using time-resolved two-photon photoemission to create a coherent superposition of neighbouring image-states [42] as described in section 1.6.2.

This work in this chapter extends the theoretical and experimental studies of Kazansky et al [43, 58, 73] who investigated charge transfer between cesium atoms, lithium atoms and H^- with a Cu(111) surface. The Cu(111) surface has a projected band gap at the electronic energy of the projectiles, and a strong blocking of resonant charge transfer is seen experimentally and theoretically. Experimentally H^- is scattered from the surface, and the resulting ion yield after interaction is measured. Resonant transfer of the electron to the surface would result, in this case, in a neutral H atom. The ion yield is significantly larger for the band gap containing Cu(111) than the free-electron metal Cu(110), suggesting that less of the electrons passed into the image-state and the metal, forming the neutral H atom. In effect that the presence of the band gap in Cu(111) blocks the resonant charge transfer process.

For ion and ground-state atomic projectiles the electronic energy of the

projectile is fixed. By extending this work to Rydberg atoms however, many more quantum states are selectively accessible such that a larger energy range of the surface electronic structure can be probed.

Theoretical work, described in section 3.1 used a wavepacket propagation method to determine surface ionisation rates versus distance for a moving Rydberg H atom ($n = 2 - 8$) incident at Cu(111) and Cu(100) surfaces [64]. This predicts an enhancement of the surface ionisation rate when the Rydberg energy is resonant with an image-state [64]. Some of the results from that paper are presented in section 3.1.

Previous experimental studies in our laboratory have struggled to resolve the resonance-enhancement of charge transfer in the hydrogen Rydberg atom, Cu(100) system, above the noise level [25, 80]. Here, a clean and flat Cu(100) surface is used in this study such that the signal to noise ratio is clearly improved, allowing the resonance-enhancement of charge transfer to be observed unambiguously at hydrogen principal quantum numbers for which the Rydberg energy matches the energy of one of the image-states.

5.2 Energy levels of the Cu(100) and hydrogen Rydberg system

As described in section 3.1, both the Cu(111) and Cu(100) surfaces have projected band gaps and therefore discrete image-state levels. Only the Cu(100) surface is studied here experimentally because the $n = 25 - 34$ hydrogen Rydberg levels fall within the projected band gap of this surface,

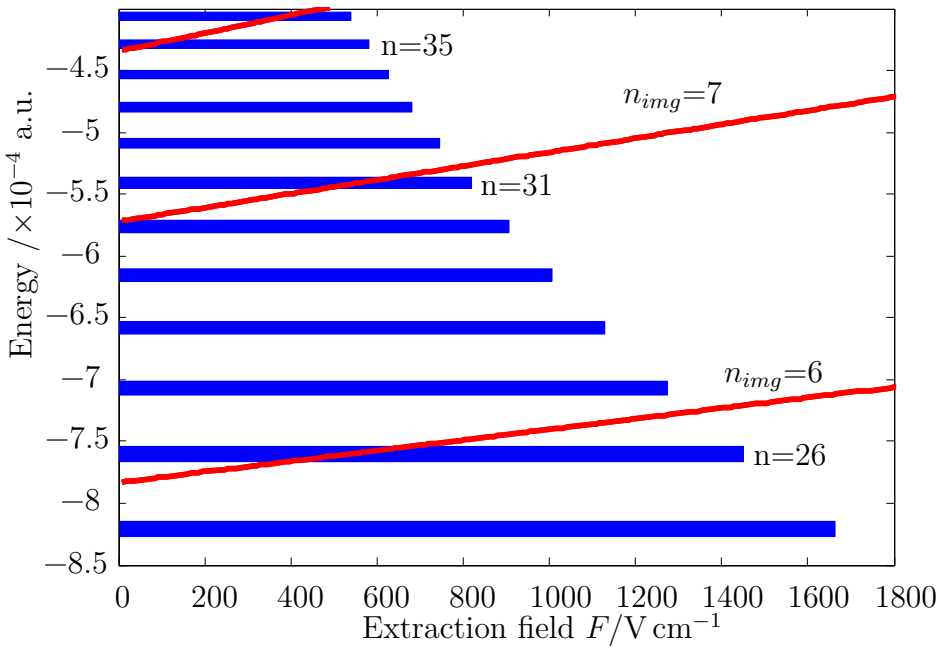

Figure 5.1: The energy levels of the $n = 25$ to $n = 35$ $k = 0$ hydrogen atom principal quantum numbers, and the image-state ($n_{img} = 5$ to $n_{img} = 9$) energies of the Copper(100) localised states. At intersections, resonance-enhancement of charge transfer is expected. The widths of the H atom levels lines represent the change in energy of the Rydberg atom on approaching the surface $D = 3n^2a_0$ and $D = 6n^2a_0$. The lengths of the blue lines represent the field ionisation threshold for the Rydberg state as measured experimentally.

whereas the projected band gap of the Cu(111) surface falls at an energy below the region of the experimentally accessible H atom Rydberg states.

Figure 5.1 shows the predicted energy levels of the $n = 25 - 35$ $k = 0$ H-atom Rydberg states and the surface-localised image-states as a function of applied external field. The mid-manifold $k = 0$ Rydberg states are selected for study, as their energies are approximately field independent and provide the greatest region of crossing with the field-dependent image-state energies.

All of the energies in figure 5.1 are determined by the diagonalisation of

a Hamiltonian discretised onto a Sinc DVR as described in subsection 2.2.5. In the case of the Cu(100) image-state energies, the potential describes the system as a semi-infinite slab of the corrugated Chulkov potential from section 2.3.2.2. No atom is included in this set of simulations and the diagonalisations are repeated over the range of experimentally applied fields, to determine the image-state energy as a function of field. The Rydberg atom energies are determined from two sets of diagonalisations, the first with the hydrogen atom at $D = 6n^2a_0$ and the second at $D = 3n^2a_0$ in front of a jellium surface. The corrugated potential used to model the Cu(100) surface requires a high density of grid points within the surface, whereas the resolution of high principal quantum number hydrogen atom states requires a large atom-surface separation and a small spacing of grid points within the atom itself. Therefore it was only computationally viable to determine the two sets of energies in figure 5.1 independently.

The differences in the energies caused by calculating the Rydberg atom energies in the presence of the Cu(100) surface, or of the image-states calculated in the presence of an atom, are expected to be minimal. However in order to determine the energy level diagram of this system exactly such calculations need to be undertaken, but would only be possible by utilising significant additional computational resources, or finding a DVR grid which converges the energies more efficiently. Additionally, in such a simulation, it should be possible to calculate the energies of the Rydberg states on approaching the surface, up to the limit of the overlapped Rydberg-image-state in which charge transfer occurs.

In figure 5.1 the width of the blue lines represents the perturbation of

the Rydberg energy due to the surface interaction over the typical range of atom-surface separations that surface ionisation occurs, $6n^2a_0$ to $3n^2a_0$. The lengths of the blue lines represent the experimentally observed field ionisation threshold for a given principal quantum number. Resonance-enhanced charge transfer is expected at applied fields corresponding to the crossing of the Rydberg and the image-state energy levels.

5.3 Surface production and characterisation

Previous attempts in our group to measure resonance-enhanced charge transfer at a projected band gap surface have used a highly polished Cu(100) single crystal without any in situ vacuum preparation [25, 80]. My subsequent surface analysis showed that this surface was considerably rough as indicated by the absence of a LEED pattern and the XPS revealed high concentrations of carbon and oxygen impurity on the surface. In the experiments presented in this chapter, the surface has been prepared in situ to remove contaminants and defects from the single crystal plane. This leads to a significant improvement in the signal to noise ratio of the data.

As described in section 4.2, the surface can be moved under vacuum to a surface analysis chamber, where LEED and XPS, are used to determine the plane of the crystal, its elemental composition, and the presence of any impurities on the surface. The $\phi = 2.5$cm single crystal Cu(100) surface was supplied by Mateck GmbH and was mounted with epoxy to a xyz rotatable manipulator. In this same chamber there is an ion gun and sample heater for surface preparation as described in chapter 4.2. Argon-ion bombardment at

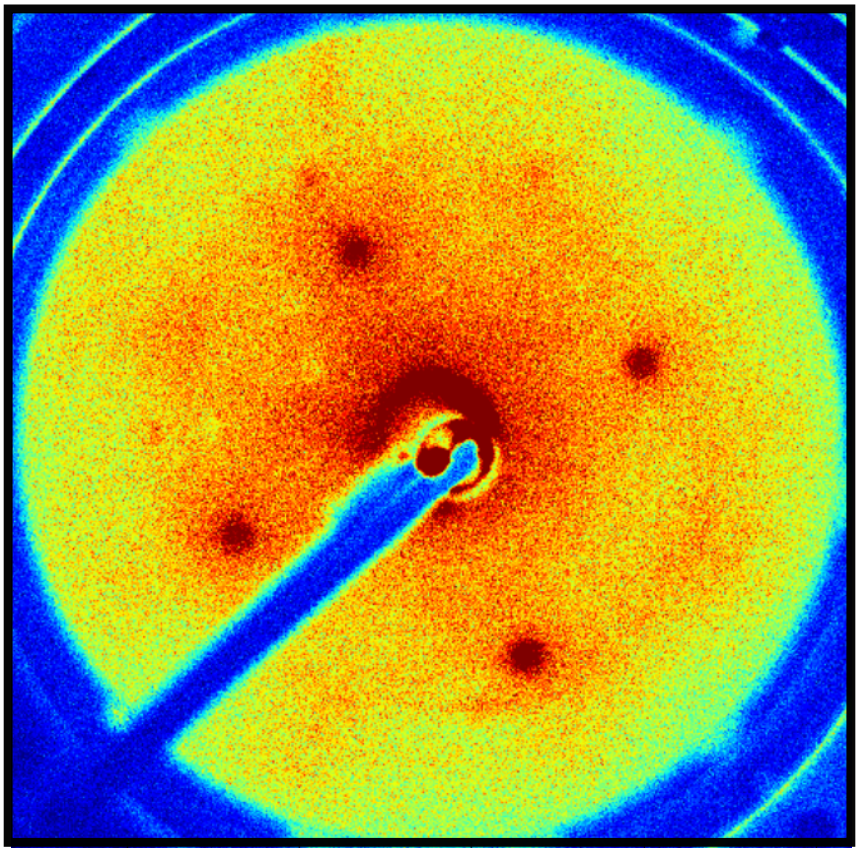

Figure 5.2: LEED pattern of the clean and flat Cu(100). The expected four fold symmetry of the (100) crystal plane is seen.

500eV sputters impurities from the surface and thermal annealing at 700 °C recrystalises the surface [89].

After twenty repeated sputtering and annealing cycles, the clean flat surface produces the LEED pattern shown in figure 5.2. The pattern displayed the expected four-fold symmetry [93] and is classified as a $(\sqrt{2} \times \sqrt{2})R45°$ [90]. This pattern in characteristic of (100) face centred cubic crystal lattices, such as Cu(100) [90].

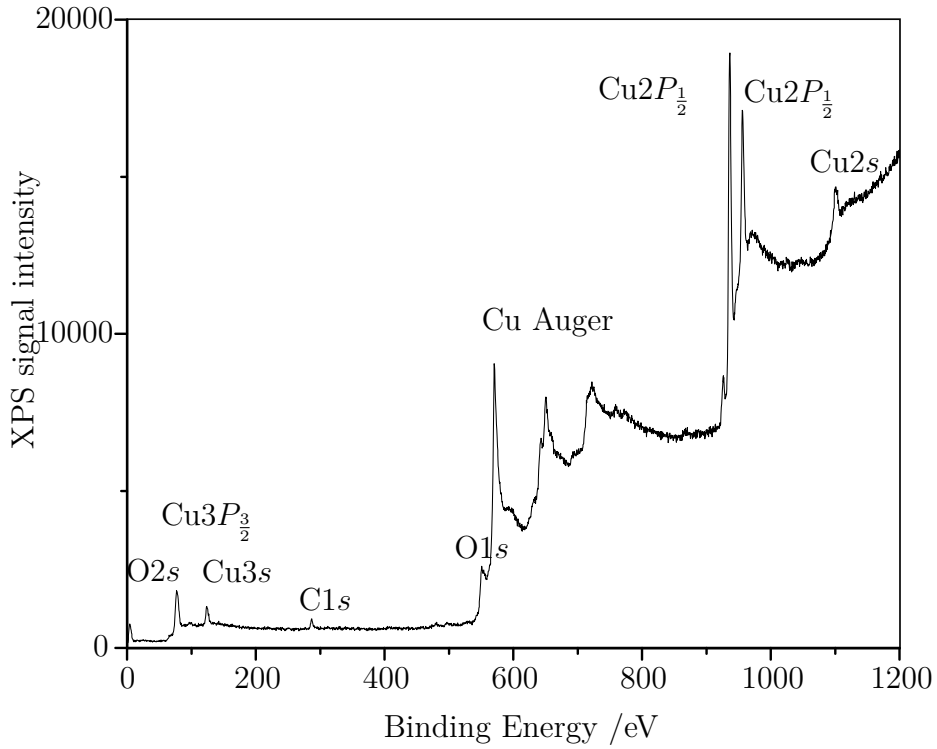

Figure 5.3: XPS of the Cu(100) surface after twenty sputtering and annealing cycles, using Al x-rays.

Figure 5.3 shows the XPS spectrum of the prepared surface measured using Al x-rays. The relative composition of the sample can be determined by the height of the XPS peaks, normalised using an element and orbital dependent sensitivity factor as described in section 6.3.2. Therefore the far greater intensity of the copper peaks compared to the oxygen and carbon peaks, and the resolution of the Cu 3s and 3$P_{\frac{3}{2}}$ which have very low sensitivity factors, demonstrate the high chemical purity of the sample with only trace levels of carbon and oxygen impurity. There are seven copper Auger peaks at 548eV, 568eV, 628eV, 640eV, 648eV,712eV, 719eV which appear as two broad features [91]. The large background is a result of inelastic scattering,

as discussed in section 6.3.2, which is very prevalent in metallic samples.

Monitoring the surface quality using LEED shows some degradation of the crystal plane over the course of a week under vacuum. Annealing the surface for twenty minutes restores the LEED pattern to its former state and the low backing base pressure means that no further sputtering is required due to the presence of few background contaminants.

5.4 Experimental results

As a hydrogen Rydberg atom approaches the surface, the height and width of the barrier in the electronic potential between the atom and surface decreases, increasing the probability of charge transfer as discussed in section 1.3.3. The bare positive ion will then accelerate towards the surface, attracted by its negative image charge. The minimum external field required to extract this ion from ($\vec{F}_{min}$) a given surface separation (D) is dependent on that distance and on the kinetic energy of the originally incident H atom along the surface normal ($T_\perp$). For a perfect conductor in (a.u.),

$$\vec{F}_{min}(D, T_\perp) = \left[\frac{1}{2D} + \sqrt{\frac{T_\perp}{D}}\right]^2 \tag{5.1}$$

as derived in section 1.3.4. At the same time, the ionisation distance is also dependent on the applied extraction field, as this also affects the potential barrier as discussed in section 3.1.7. Experimentally, we observe 'surface ionisation profiles' as shown in Fig. 5.4. Each records the intensity of ion signal resulting from surface ionisation of the Rydberg atom as a function of

extraction field. The profiles shift to higher field as n decreases, because the ionisation occurs closer to the surface as discussed in section 3.1 so a greater field is required to extract the ion from equation 1.21. The gradual increase of the signal with increasing field above F_{min} reflects the range of distances over which ionisation takes place, but also reflects the distribution of surface charges that affect primarily the extraction probability [30, 94]. Localised stray fields associated with surface inhomogeneities modify the height of the barrier to surface ionisation, leading to changes in the atom-surface separation at which surface ionisation occurs. A positive stray field lowers the barrier to surface ionisation and so increases the atom-surface separation for surface ionisation, whereas a negative stray field leads to a surface ionisation closer to the surface. Ultimately at low applied fields, the presence of positive stray fields leads to a small amount of measurable surface ionisation signal.

At sufficiently large applied fields the Rydberg atom is field-ionised before reaching the surface. Ions produced via this process arrive at the detector earlier than ions produced via surface ionisation and so are separated in time; the field ionisation signal is used here to normalise the surface ionisation profiles, to account for fluctuations in laser power and molecular beam density. It is valid to use the field ionisation signal for normalisation as the field ionisation signal is independent of the surface characteristics. All the surface ionisation profiles show a high-field cut off where field ionisation begins to dominate over surface ionisation.

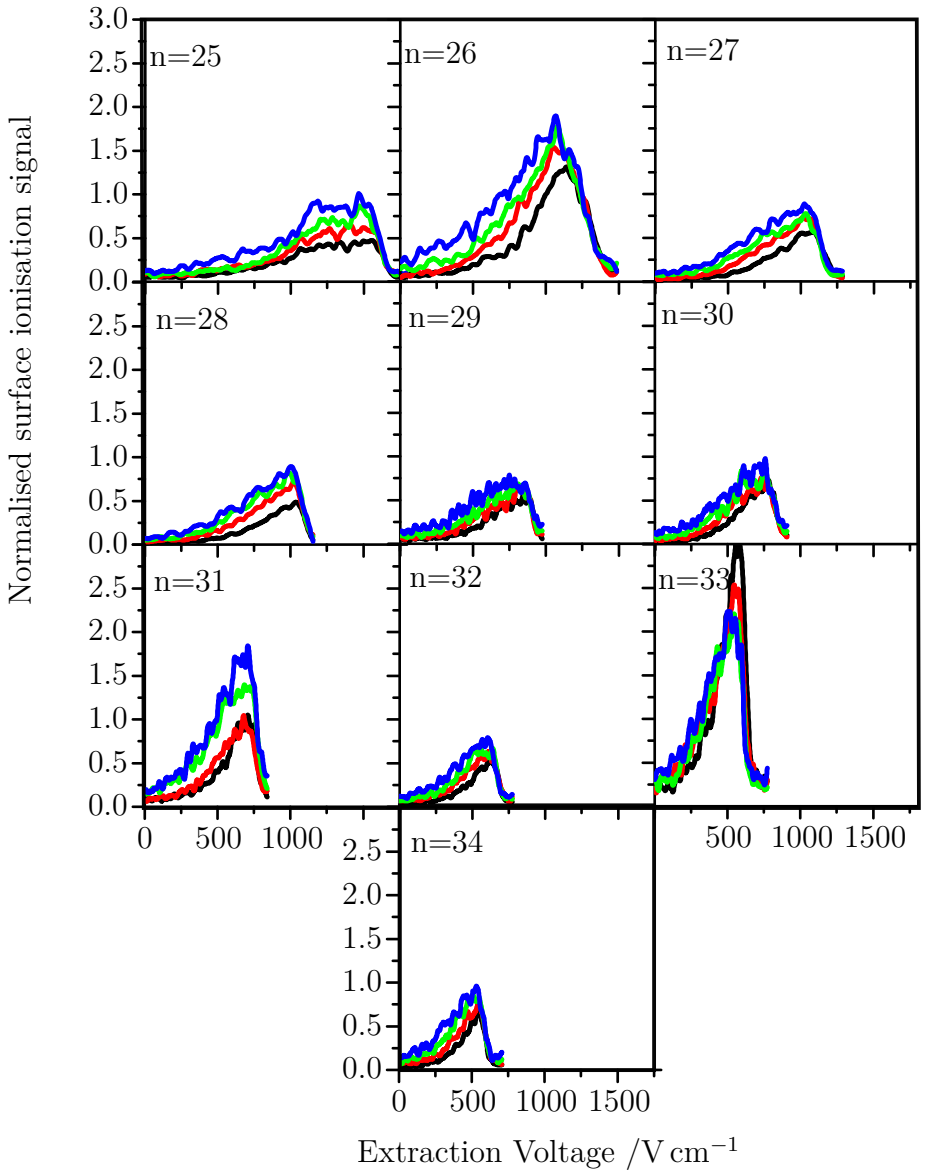

Figure 5.4: Surface ionisation profiles for the hydrogen Rydberg atoms $k = 0$ with principal quantum numbers $n = 25 - 34$ at various collisional velocities. Black profiles are 850m s^{-1}, red 700m s^{-1}, green 600m s^{-1} and blue 500m s^{-1}.

5.4.1 Clean Cu(100) and hydrogen Rydberg atoms

Figure 5.4 plots the surface ionisation profiles for $n = 25 - 34$, $k = 0$ hydrogen atom Rydberg states and a Cu(100) surface, at four different perpendicular collisional velocities. Figure 5.5 plots the integral of these surface ionisation profiles as a function of n.

The surface ionisation profiles in figure 5.4 show some similarities to those measured for H atoms incident at a gold surface [5]. At a gold surface the Rydberg electron energy is always degenerate with the conduction band of the metal, so resonant charge transfer occurs for all principal quantum numbers. In figure 5.5 the yellow line plots the integrated surface profile for a gold surface, and the integrated signal decreases monotonically as n increases. This is because the range of applied fields over which ions, formed by surface ionisation, are extracted, decreases, with increasing n, i.e., higher n Rydberg atoms have a larger radius and so surface ionise further from the surface, and higher n Rydberg atoms field ionise more readily.

In the case of Cu(100) however there are large variations in the intensity of the surface ionisation signal as a function of n. As figure 5.4 shows, the maximum surface ionisation signal (normalised to field ionisation) for $n = 26$ is twice that for $n = 27$, a much larger variation than observed for gold, and the low-field part of the profile is also raised in intensity. Other high intensity profiles are seen at $n = 31$ and $n = 33$. The increased intensity at lower extraction fields implies a greater propensity for ionisation to occur at a greater distance from the surface

The integrated surface ionisation signal shows clear non-monatomic vari-

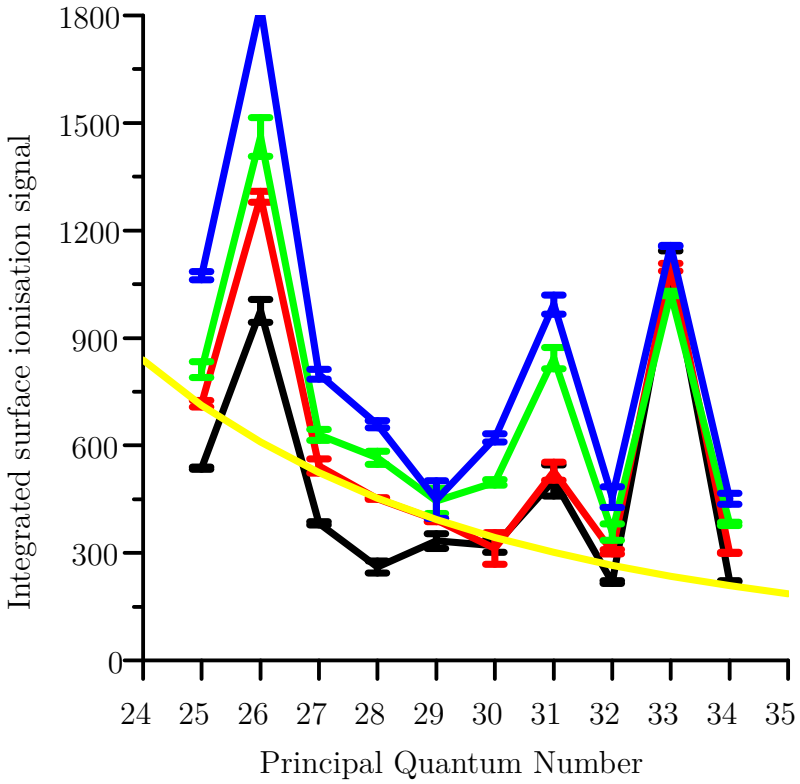

Figure 5.5: The integrated surface signal at a Cu(100) surface as a function of hydrogen principal quantum number. Clear non-monotomic bahviour is seen, indicating resonance-enhancement of charge transfer. Black profiles are $850\,\mathrm{m\,s^{-1}}$, red $700\,\mathrm{m\,s^{-1}}$, green $600\,\mathrm{m\,s^{-1}}$ and blue $500\,\mathrm{m\,s^{-1}}$. The yellow line shows the integrated surface ionisation signal for hydrogen Rydberg atoms incident at a a gold surface at a velocity of $650\,\mathrm{m\,s^{-1}}$ [5].

ation with n, and we attribute this to the energies of the Rydberg states coming in and out of resonance with the image-states. In Fig. 5.5 clear resonances are seen at $n = 26$ and $n = 33$, and an additional smaller effect at $n = 31$. This non-monotonic behaviour arises from energy matching between the H atom Rydberg electron and the copper-localised image-charge state.

The locations of the resonances in Fig 5.5 coincide with the level crossings predicted in Fig. 5.1, except that there is a crossing at $n = 33$ rather than 35. As discussed in section 5.2 the calculations are approximate as the energies of the image-states and the Rydberg atoms are determined separately, such that this seems to indicate good agreement between theory and experiment.

However, the good match between experiment and theory implies that the enhancement in charge transfer is a result of resonances between the Rydberg energy levels and the image-states. This result implies that the Rydberg electron preferentially penetrates the surface along the surface normal. This is predicted by the location of the saddle point in the total electron potential, as described in section 1.3.3 and the wavepacket propagation calculations described in section 3.1. Additionally these experiments show that Rydberg atoms can be used as a direct probe of high lying image-states, otherwise accessible only by the TRPES [42]. Such a method uses coherent excitation of several image-states, resulting in a quantum beat spectrum, which can be complex to decouple.

It is interesting to note that the integrated signal at the off-resonance n values follows the same trend as the purely resonant gold surface, as illustrated by the yellow line in figure 5.5. This indicates that at the resonances a true enhancement of charge transfer is seen, rather than a depletion for the off-

resonance states. This is due to pure image-state penetrating further into the vacuum than the image resonance, formed when the image-states overlap with the conduction band of a metal, as is the case for a gold surface. Effectively overlap is better for an on-resonance Rydberg atom and a pure image-state, than for a Rydberg atom and an image resonance.

5.4.2 Experimental velocity dependence of the interaction

The velocity dependence of the surface ionisation dynamics is also investigated experimentally. As is discussed in section 3.1, decreasing the velocity of the incident H atom leads to a surface ionisation further from the surface and therefore a lower field is required to extract the ion from equation 1.21. Therefore more surface ionisation signal is seen at lower perpendicular collisional velocities of the hydrogen Rydberg atoms. The surface-ionisation profiles (signal versus applied field) for on-resonance n values show a changing shape as the velocity is changed, reflecting the restriction of the resonance to a certain range of applied field.

As discussed in section 3.1 and [64], measuring surface ionisation profiles for different velocities will give us an extra handle on resonance-enhancement of charge transfer. Experimentally, the velocity can be varied by changing the delay between the photodissociation excimer laser pulse and the two-colour Rydberg excitation lasers. As explained in chapter 4 over the 46cm distance between the positions of photolysis and Rydberg excitation, the atoms spread out in the longitudinal direction according to their velocity;

hence changing the delay picks out a different velocity component, and this is variable between $500\mathrm{m\,s^{-1}}$ and $850\mathrm{m\,s^{-1}}$ for an unseeded H atom beam, with a velocity resolution of 1%.

Each connected set of points in figure 5.5 represents the integrated surface signal for different incident velocities of hydrogen. In general there are two contributing factors to the velocity dependence of the signals: ion-extraction efficiency and ionisation distance. The first effect, shown by equation 1.21, is that the minimum extraction field required to extract a particular ion is dependent on its incident velocity, i.e., it requires a smaller applied field to pull the ion away from the surface if its initial velocity is lower. The second effect is that more slowly moving atoms will have more time to be ionised at greater distances from the surface even though the ionisation rate is slow, and hence the mean ionisation distance increases, reducing the minimum extraction field required for ion extraction.

For the off-resonant n values there is an overall increase in signal amplitude as the velocity decreases, and the increase is a little greater at lower field values - e.g, for $n = 27$ the signal at $500\mathrm{V\,cm^{-1}}$ for a velocity of $1000\mathrm{m\,s^{-1}}$ is around 4 times its value at $1800\mathrm{m\,s^{-1}}$. At $1000\mathrm{V\,cm^{-1}}$ the difference is only a factor of 1.5. For the resonant n values, the signal enhancement occurring as the velocity is lowered tends to lead to a change in shape of the profile. For example for $n = 33$ the $850\mathrm{m\,s^{-1}}$ signal (black) lies above the $500\mathrm{m\,s^{-1}}$ signal (blue) at $550\mathrm{V\,cm^{-1}}$ but lies below it at $300\mathrm{V\,cm^{-1}}$ as shown in figure 5.6. The shape change with velocity reflects the fact that the energy levels are field dependent so that the resonance only occurs over a certain field range, and the velocity effects are likely to be different when the system is in the

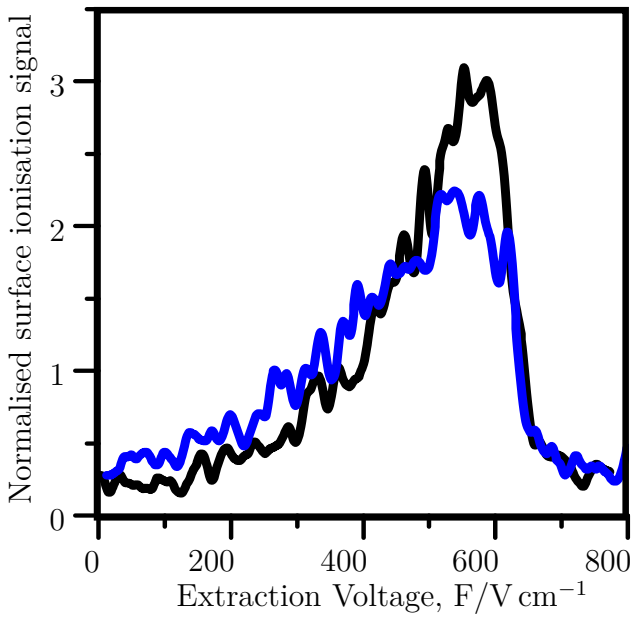

Figure 5.6: The surface ionisation profile for the $n = 33$ hydrogen atom Rydberg state and the Cu(100) surface with an incident velocity of 850m s^{-1} in black and 500m s^{-1} in blue.

resonant field range compared to the off-resonant field range.

5.4.3 Effect of the surface cleanliness

The measurements presented in this chapter using a clean Cu(100) surface show far clearer resonance-enhancement effects than any previous attempts to measure this system [25, 80]. Therefore the presence of any impurities or roughness on the surface has a large effect on the ionisation dynamics. Figure 5.7 shows the evolution of the surface ionisation profiles of $n = 26$ and $n = 28$ over the course of two days.

The on-resonance $n = 26$ profiles always have significantly more surface ionisation signal than their off-resonance counterpart, but this difference is reduced over time. After one day $n = 28$ gives significantly more signal than

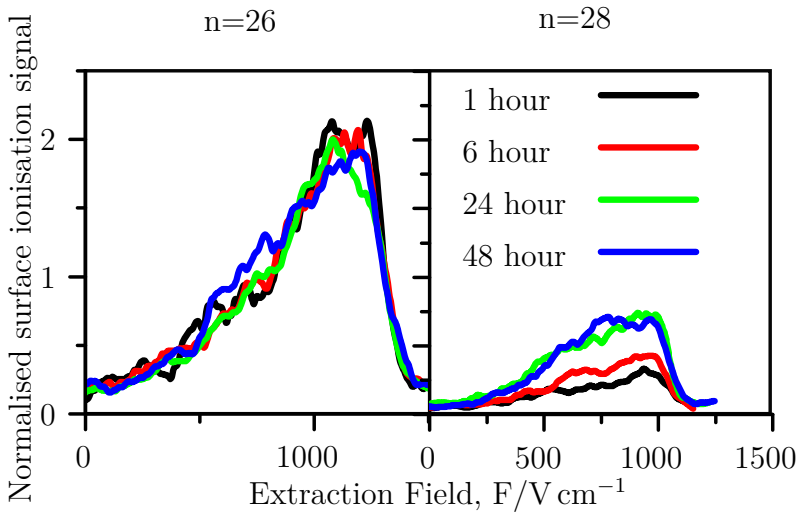

Figure 5.7: The on-resonance $n = 26$ and the off-resonance $n = 28$ surface ionisation profiles measured over two days from surface preparation.

when ionising in front of a freshly prepared surface. There is no change in the ionisation behaviour of the on-resonance case for which the Rydberg orbital already has a good overlap with the copper image-states. However for the off-resonance case any additional states arising from the adsorbate layers and protruding into the vacuum, allow for the possibility of alternative mechanisms for surface ionisation, and therefore a small increase in signal is seen. This can possibly be attributed to background gas in the chamber absorbing on to the surface, producing additional adsorbate layer localised states into which the hydrogen Rydberg can ionise [95]. Alternatively the presence of adsorbates on the surface will give rise to larger stray fields which would increase the amount of surface ionisation signal measured [11]. After approximately two days the surface ionisation profiles seem to become more constant.

These results suggest that in the limit of a partially unclean surface the

amount of surface ionisation for the off-resonance case increases towards the on-resonance surface ionisation profiles, reducing the effects seen in figure 5.5. However it is expected that in the limit of a very rough or impure surface ultimately the (100) plane is lost, and the image-states form a broadened continuum of image resonances, washing out any resonance effects.

5.5 Conclusions

This work has demonstrated that the predicted resonances between hydrogen atom Rydberg states and the image-states within the projected band gap of a copper(100) surface are experimentally observable. A theoretical model can be used to explain the presence of resonances in terms of energy crossings. Varying the velocity of the incoming beam provides a useful additional diagnostic for the existence of the resonance effects, but as described in section 3.1 the velocity dependence of the surface ionisation profile in such a system is complex to understand. This work is the first to directly measure the $5 \leq n_{\mathrm{img}} \leq 7$ image-states of the Cu(100) system. It is clear that the Rydberg-surface collision experiment can lead to useful information about the electronic structure of the surface, not just the Rydberg atom itself, and this type of experiment may be applicable to other systems where there is quantisation of the surface states, such as thin films in the following chapter.

Chapter 6

Ionisation of hydrogen Rydberg atoms at iron thin films

The ionisation of $n = 26 - 34$ hydrogen Rydberg atoms at a series of iron thin films is investigated experimentally for the first time. Thin films have discrete image-states due to the particle-in-a-box style potential along the surface normal. Overlap between these discrete image-states and the energies of specific principal quantum numbers of hydrogen cause resonance-enhanced charge transfer, similar to the effects seen with the Cu(100) surface in chapter 5. However, in this case, the results are tuneable, as with successive iron depositions the thickness of this one-dimensional well increases.

6.1 Wavefunctions and energy levels of the thin film system

The electronic structure of a thin metallic film can be described as a one-dimensional quantum well along the surface normal, and a continuous free-electron system in the dimensions parallel to the surface. Unlike a truly metallic surface, the discrete quantum well-states form the basis for a series of two-dimensional bands in the metallic thin film.

The one-dimensional confinement along the surface normal results in discrete particle-in-a-box style states, as described in section 1.5.2. These quantum well-states are fully localised within the thin film, and have a nodal structure described by a principal quantum number, n_{well}. The quantum well-states become increasing well spaced with increasing energy, but bunch together near the vacuum level due to the softened boundaries of the thin film potential as shown in figure 6.1. As the film thickness increases the energy of a given quantum-well-state drops, and neighbouring states become closer together. The quantum-well-states form the basis of a series of two-dimensional manifolds which stack on top of each other, such that as the film tends towards infinite thickness, the bulk limit of a three dimensional band is recovered.

Photoemission studies of thin films have focused on determining the energies and spatial distribution [47] of the quantum-well-states within thin films, and their dependence on the substrate and the evaporant [45, 46].

The energy levels and wavefunctions of an electron outside of a thin film are determined via diagonalisation of a one-dimensional Jellium quantum

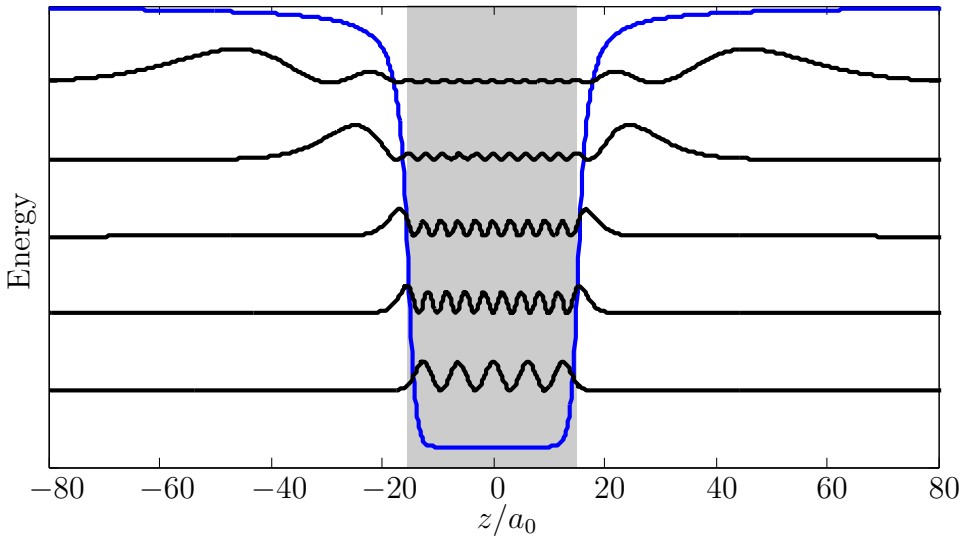

Figure 6.1: A selection of five monolayer wavefunctions ordered according to increasing energy which have been artificially spaced for clarity. The blue line shows the one-dimensional jellium well and the grey box indicates the thickness of the five monolayer film. For the highest energy wavefunctions, near the vacuum level, changing the density of DVR grid points alters the probabillity density of the wavefunction, but not the location of the nodes.

well on a Sinc DVR [70]. This method has previously been used by Usman *et al.* [9], and in our previous work [96].

The thin film projected band structure is not a true projected band gap, as in the Cu(100) case, but has discrete quantum well-states, which terminate at the surface. The overlap between these discrete quantum well-states and surface localised pure image-states, leads to combined 'well-image' states at the surface of the thin film where there is a resonance between the two types of state. As the well thickness changes the quantum-well-states change in energy and density, but the image-state component is solely dependent on the plane of the surface, hence, the nature of the well-image states changes with well thickness. The well-image states have an image-state tail into the

vacuum on both sides of the thin film, and nodes within the surface itself. The Rydberg electron preferentially enters along the surface normal, such that in the thin film case, the well-image states are the most likely state to be initially occupied by the Rydberg electron during surface ionisation.

In order to understand the nature of the well-image state wavefunctions it is necessary to calculate the probability density, such that the location of the nodes and the boundary conditions can be understood. The probability density is given by $|\psi^*\psi|$, where ψ is the electronic wavefunction determined from the time-independent one-dimensional diagonalisation described in the previous section. The only wavefunctions determined are those which can be occupied by a bare electron outside of the surface.

The wavefunctions determined are a linear combination of a quantum well localised particle-in-a-box state, and a surface-localised image-state, which extends into the vacuum. The combined wavefunctions can be thought of as the overlap between the two different discrete ladders of states, where a given total wavefunction has a contribution from both sets, but not necessarily in equal measure as some states have more well-state character than others.

Figure 6.1 shows the probability density for a selection of wavefunctions of the 5ML thin film. In this figure the wavefunctions have been artificially spaced for clarity. The lowest energy wavefunctions, at the bottom of the well have pure particle-in-a-box character, with a well defined number of nodes which can be assigned a principal quantum number n_{well}, and no protrusion into the vacuum. At these lowest energies there is no contribution from the image-states as the Rydberg-like image series is very well spaced. As the wavefunctions increase in energy the well-image states develop increasing

image-state character, protruding into the vacuum and with significant population outside of the surface. At the energy range of our experimentally accessible wavefunctions the wavefunctions have several nodes outside the surface and protrude for nanometers into the vacuum, however there is still well defined particle-in-a-box character and the size of the contribution from each one varies from one wavefunction to the next. Near the vacuum level, the well-image states have almost pure image-state character, with little amplitude in the well region. These high lying wavefunctions protrude for tens of nanometers into the vacuum making it difficult to converge the calculations, without the DVR grid affecting the intensity in each node.

As the film thickness increases the same pattern emerges, however there are more pure-well localised states at the bottom of the well, and the image-state contribution to the total sum of states is smaller. This can be understood as the nature of the surface and the band gap determines the energy and number of pure image-states. The thickness of the film determines the number of pure well localised states, such that the 10ML surface has more pure well-states than the 5ML. This means that the combined wavefunctions determined here, result in more states overall with the image-state character as shown in figure 6.2. In the 10ML case at the experimental energy range of interest the well-image states still have significant well and image-state character, but nearer the vacuum level, the states have more particle-in-a-box character than for the 5ML thin film.

Finally for the 30ML case there are far more well-states in the discrete ladder, than image-states such that the combined wavefunctions are dominated by particle-in-a-box character even at the experimental energy range of interest.

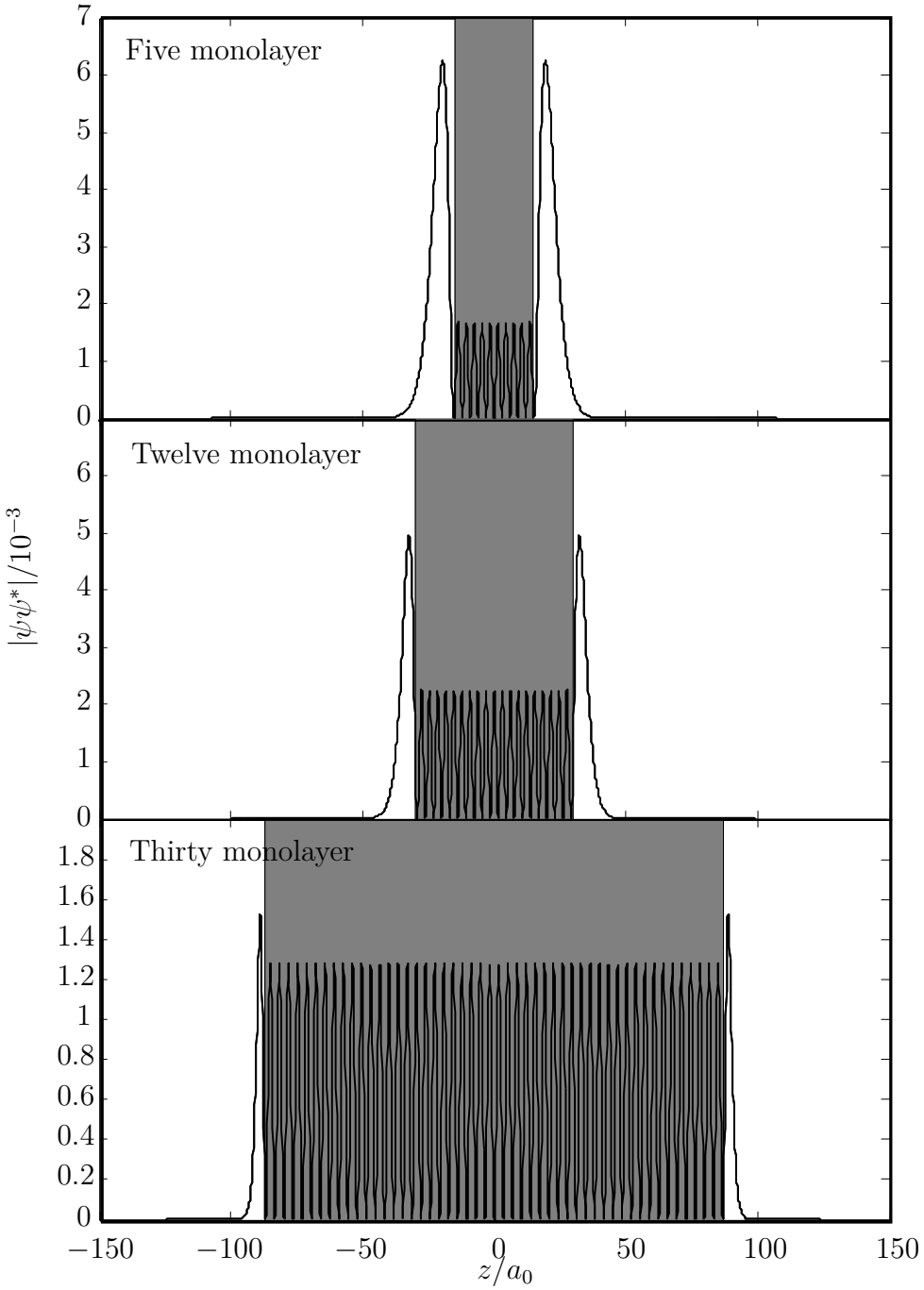

Figure 6.2: The probability density of the well-image state wavefunctions for a five, twelve and thirty monolayer thin film. These wavefunctions were selected because they show the maximum image-state character, for the well-image states associated with the first image-state.

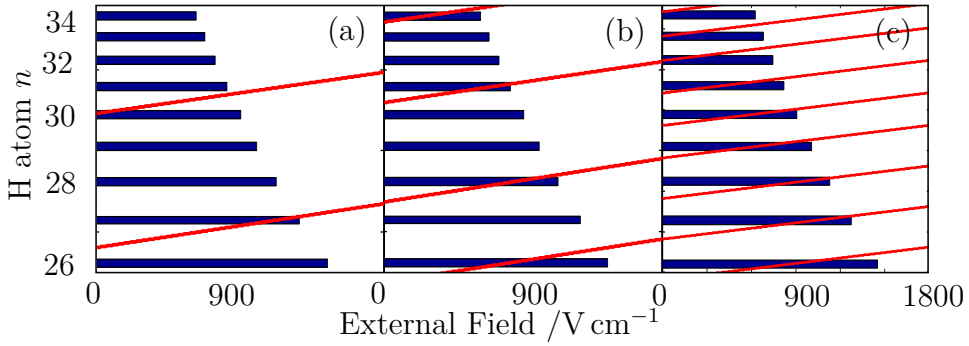

Figure 6.3: The image-state energy levels of the (a) five monolayer, (b) twelve monolayer and (c) thirty monolayer one dimensional quantum well in red, and the $n = 26 - 34$ $k = 0$ H atom Rydberg states as a function of external field in blue.

Effectively the wavefunctions have become more confined to the thin film, and the image-state tail does not extend as far into the vacuum. Ultimately it is expected that as the thin film is increased in thickness, this contraction would result in the wavefunctions tending towards the bulk limit. In the case of a bulk metal surface the discrete image-states overlap with the whole band, mixing and broadening the image-states, such that at all energies the wavefunctions have some image-state character, but the states are more surface localised and when occupied the electron effectively occupies the band state. This is called an image resonance, as described in section 1.6.

The well-image state energy levels, are shown in red in figure 6.3. As pure image-states are susceptible to external fields it is expected that the well-image states are too, and so the diagonalisations are cycled over the experimental applied fields. The blue states in figure 6.3 are the energy levels of a $n = 26 - 34$ hydrogen Rydberg atom on approach to a metal surfaces as a function of external field calculated using equation 1.13. At the

intersection points between the red and blue lines in figure 6.3 there is optimal overlap between the Rydberg electron wavefunction and the well-image state wavefunction due to energy matching, mediated by a specific external field and resonance-enhanced charge transfer is expected.

The energy levels of the image-states are not a continuous variable as the 'allowed' thicknesses are determined in monolayers of iron i.e. only integer multiples of the radius of iron are considered. In this work the ionic radius of iron, $r_{\mathrm{Fe}} = 155\mathrm{pm}$ [97] is assumed, but the assumption that iron will have the same radius in a thin film as in a bulk metal is a possible source of error in the calculations. The resultant energy levels have some particle-in-a-box character, such that thicker films yield closer well-image states, i.e., $E \propto \frac{1}{L^2}$ where L is the thickness. However, the thin film is not an infinite well, and has 'softened' sides, such that there is a greater density of states near the vacuum limit.

From figure 6.3, resonance-enhanced charge transfer is only likely to be distinguished in our experiments when the energy gaps between the well-image states are significantly greater than the Rydberg energies. Once the spacings between well-image states and Rydberg states becomes comparable the system goes below the effective resolution of our experiment, and the thin film becomes indistinguishable from a 'bulk' surface. This loss of resolution is expected to occur around thirty monolayers, or 4nm, as shown in part (c). It is expected that more resonances will be seen in the twelve monolayer case than the five monolayer, and resonant energies will shift between the two thin films. No resonance-enhancement is expected in the thirty monolayer case.

Interestingly, the thin films investigated in this chapter are significantly

thinner than the radius of the Rydberg atoms, i.e., for $n = 30$ the Rydberg radius is $\approx$ 45nm whereas the 30ML thin film has a thickness of $\approx$ 4nm. The classical image charge model would in this case locate the image point charges within the thin films support substrate, in this case a Mica insulator. However, the image charge is not a point charge, but is a localisation of charge near the front of the surface, which gives the same electrostatic field outside the surface as a point charge at a greater distance, much like an optical reflection of an object in a mirror. This assumption allows us to model the thin film as a symmetrical well on both sides, i.e., as an unsupported film.

6.2 Previous studies

Previous experimental studies have focused on determining the energy and spatial distribution of the well-states within a thin film [47]. Various photoemission studies have established the particle-in-a-box character of the well-states [47]. Additionally the effect the band gap of the substrate, the evaporant and the crystal plane of the thin film have on the resulting well-states has been investigated experimentally [45, 46]. However no previous experimental study has measured the energy of the well-image states investigated in this chapter.

Usman*et al* studied quantisation effects on the charge transfer dynamics of ground state H^- ions (from the negative ion to the metal surface) to thin films [9]. They found that when the electronic energy of the H^- is close to that of a one dimensional well-image state, the rate of charge transfer is enhanced by a resonance effect, and the resultant ionisation probability as a

function of distance exhibits multiple peaks due to the many quantised thin film states that the atomic energy level crosses when the H^- approaches the thin film [9].

The observation of a resonance effect close to the one-dimensional quantised level can be explained by the preferential direction of charge transfer, which is along the surface normal where the saddle point in the effective potential is located. Therefore the charge transfer is most efficient when there is a minimum transfer of momentum in the direction parallel to the surface (when the Rydberg energy is close to the one dimensional quantised state).

Surface ionisation experiments allow states with significant image-state character, such as the well-image states, to be probed directly. The advantage of using Rydberg atoms over ion projectiles for these surface ionisation experiments however is that a larger energy range can be probed, as can well-image states nearer the vacuum level. This allows for more of the surface electronic structure of the thin film to be investigated.

6.3 Surface production and characterisation

The films are prepared in situ, for optimal control over the flatness and cleanliness. A muscovite crystal, which has the Mica crystal type, is cleaved in air to produce a perfect (001) plane. The LEED pattern exhibited pseudo-hexagonal symmetry [92] suggesting the crystal is free from major defects and contaminants.

6.3.1 Producing thin films in situ

Thin films are deposited onto the muscovite base using an electron beam evaporator with an integrated flux monitor. The evaporator is mounted on axis. An iron rod is used as the evaporant as supplied by Mateck GMBH. The ion flux is measured by the integrated flux monitor and is approximately 1ML/min. The diameter of the evaporant beam is approximately 1cm as measured by XPS.

The integrated flux monitor is used to measure the evaporant ion flux in real time during the evaporation process. This allows the deposition rate to be calculated once the spot size is known. The evaporator used in these experiments has been used previously by Howard *et al*, who quoted the evaporation rate from the integrated flux monitor directly [98]. However as these experiments are the first time the evaporator has been used with the Rydberg surface experiment, additional XPS measurements were made to confirm the accuracy of the integrated flux monitor.

6.3.2 Film thickness analysis using XPS intensities

The XPS spectra of the muscovite base and three iron thin films are shown in figure 6.4. After evaporation of iron, peaks between 650eV and 1000eV grow in. These lines are the Fe XPS lines for the 1s at 845eV, 2s at 720eV and $2P_{\frac{3}{2}}$ at 707eV in Al x-rays [91]. The XPS signal amplitude is proportional to the film thickness. As the thickness increases, peaks from muscovite components will decrease in intensity whilst those from iron will increase.

The different spectra have different background levels between the sharp

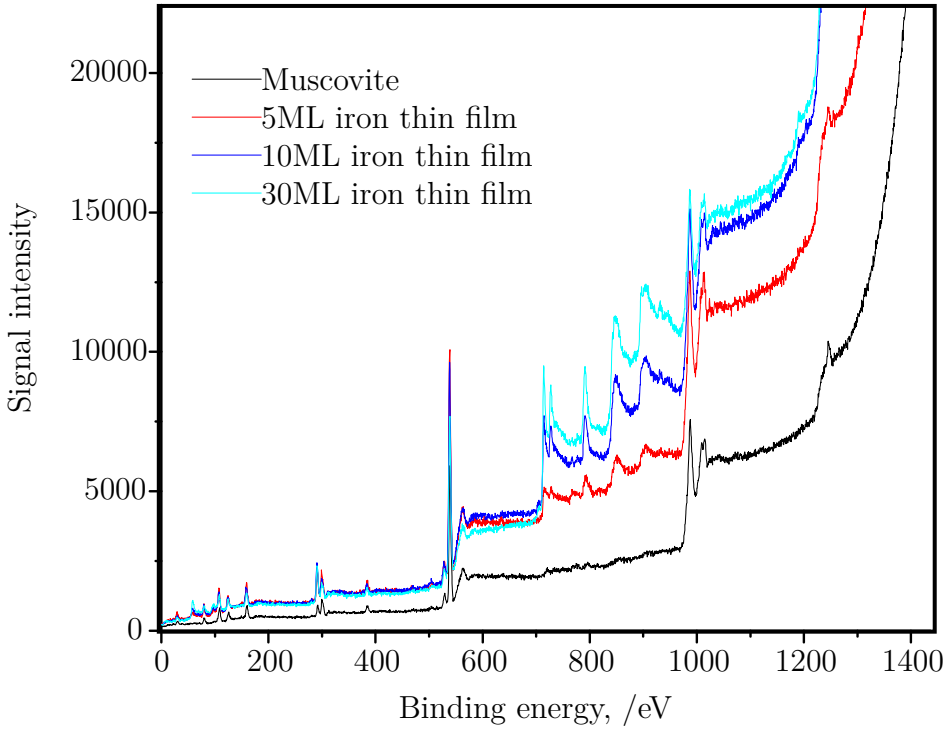

Figure 6.4: XPS of the Mica and 5ML, 10ML and 30ML iron thin films.

XPS and Auger peaks. The background is a combination of inelastically scattered electrons and excited intrinsic plasmons [99]. Both of these contributions are larger for metals, so as iron is added the background increases [91]. The peak height is taken to be the distance from the peak maxima to the background on the low binding energy side. The proportion of each element present in an XPS spectrum is approximated by,

$$\chi_A = \frac{{}^{I_A}/_{I_A^\infty}}{\sum_{i=1}^{n} {}^{I_i}/_{I_i^\infty}} \tag{6.1}$$

where χ_A is the mole fraction of element A in the sample, I_A is the intensity of the chosen XPS peak of element A, I_A^∞ is the tabulated sensitivity factor [100]

and n is the array of elements in the whole sample. Equation 6.1 therefore gives the stoichiometry of the substrate.

Using the black line in figure 6.4 the composition of muscovite is determined to be $Al_2KSi_3FO_{12}H_n$, compared to the expected composition of $Al_3KSi_3F_2O_{12}H_n$. The discrepancy in Al and F comes from the low sensitivity factors of these elements.

The model can be expanded to account for the film thickness of the thin films. Intensity analysis is carried out on the O 1s peak and the Fe 1s peak to give an amount ratio of Fe to O in the sample. By accounting for differences in the stoichiometry and size of the units cells a monolayer ratio can be determined, which after accounting for the unit cells dimensions results in a thickness ratio between the iron and the muscovite layers. Comparison of these ratios for sequential thin film thicknesses results in the ratio of amounts of iron in different films. For the five : ten : thirty monolayer thin film, the XPS analysis gave ratio of 1 :2.6 : 6.2. However this method fails to account for the differing amounts of inelastic scattering experienced by photoelectrons from the muscovite substrate and the iron thin films which are emitted from different depths within the surface.

Mica is a birefringent material, and this optical anisotropy makes it very difficult to carry out ellipsometry on the surface to determine thin film thickness after the sample has left the vacuum.

6.4 Experimental results

Surface ionisation profiles were measured for hydrogen atom Rydberg states incident at the bare muscovite surface, and three iron thin films of different thicknesses. Mid-manifold $k = 0$ Rydberg atoms were used unless otherwise stated, so the Rydberg energy will not change with applied field, to maximise the overlap with surface localised image-states, with principal quantum numbers $n = 26 - 34$. Four perpendicular collisional velocities of $500\mathrm{m\,s^{-1}}$, $600\mathrm{m\,s^{-1}}$, $700\mathrm{m\,s^{-1}}$ and $850\mathrm{m\,s^{-1}}$ were used to assess the velocity dependence of the surface ionisation profiles.

6.4.1 Muscovite surface

It is important to determine whether the ionisation dynamics at a thin film are dominated by the thin film or the evaporant substrate as described in section 6.1. Surface ionisation profiles for the evaporation substrate, a flat air cleaved muscovite surface, were first measured to test the validity of our unsupported thin film model.

Muscovite is a dielectric material which charges up in the presence of an external electric field. To minimise charging effects these experiments were carried out without a Stark field at the time of extraction. An extraction field was applied after 1µs. Unpolarised Rydberg atoms such as this can be described as a linear combination of all available Stark states with the relative population determined by the transition probabilities to these states and the presence of any stray fields. Previous measurements have shown that the use of unpolarised Rydberg atoms leads to a broader onset of field ionisation, as

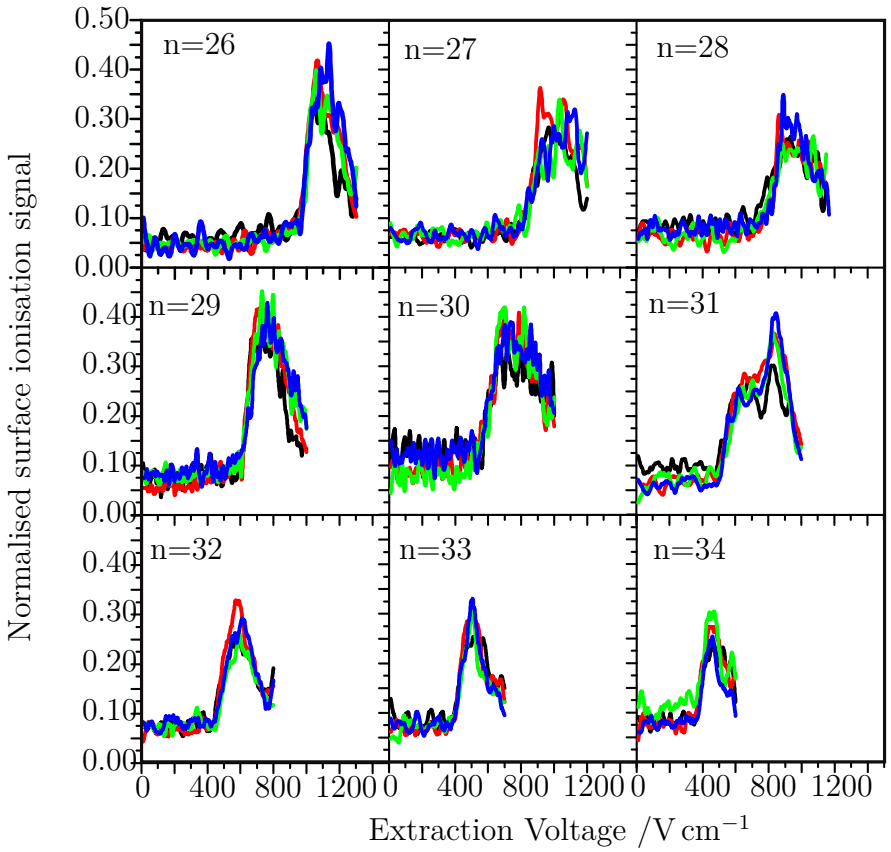

Figure 6.5: The surface ionisation profiles for the unpolarised $n = 26 - 34$ hydrogen atom Rydberg states incident at an air cleaved muscovite surface (Mica), for a series of perpendicular collisional velocities. The black lines are 850m s^{-1}, the red 700m s^{-1}, the green 600m s^{-1} and the blue 500m s^{-1}.

the different superposed k states have different field ionisation cutoffs [10].

The surface ionisation profiles in figure 6.5 show a measurable surface ionisation signal, but one that behaves very differently from a metallic surface. As the principal quantum number increases, the onset of surface ionisation shifts to lower fields. This is expected, as the increasing radius of the Rydberg atom facilitates ionisation further from the surface. However, the onset of surface ionisation occurs at higher voltages than we have observed for a

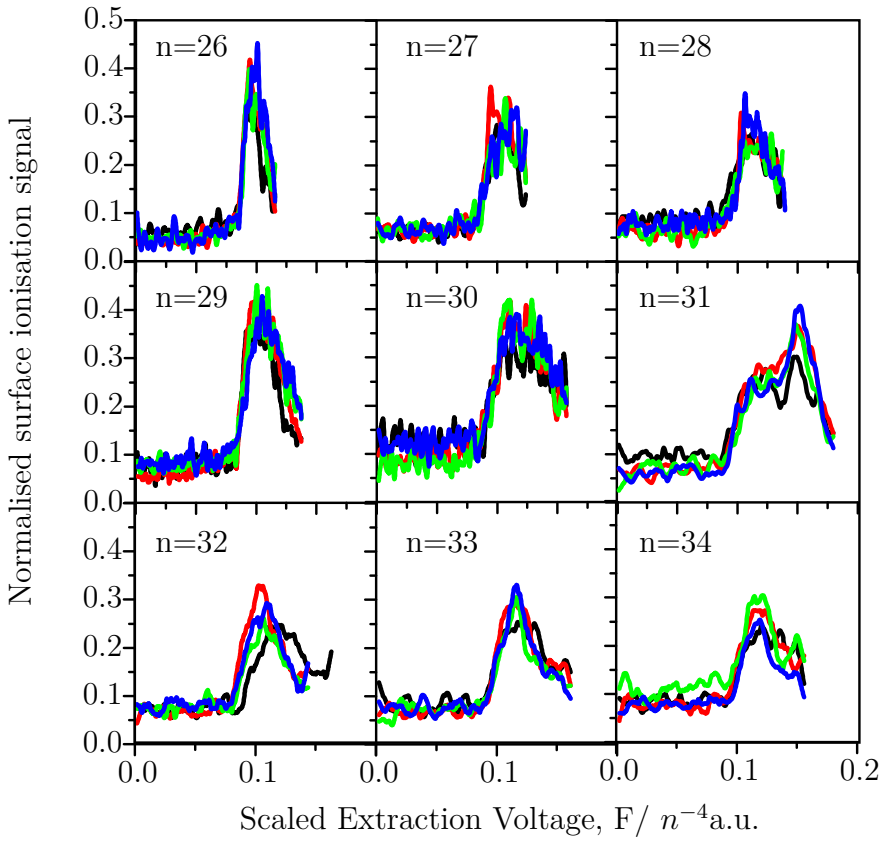

Figure 6.6: The surface ionisation profiles for the unpolarised $n = 26 - 34$ Hydrogen atom Rydberg states incident at a air cleaved muscovite surface, for a series of perpendicular collisional velocities. The black lines are $850\mathrm{m\,s^{-1}}$, the red $700\mathrm{m\,s^{-1}}$, the green $600\mathrm{m\,s^{-1}}$ and the blue $500\mathrm{m\,s^{-1}}$. The extraction field has been scaled to be account for the different expected onsets of surface ionisation for different principal quantum numbers.

metallic surface and there is a sharper onset for metallic surfaces. In each case there is a range of approximately two hundred $\mathrm{V\,cm^{-1}}$ where there is both a measurable field ionisation and surface ionisation signal. This may be due to using unpolarised Rydberg states which are a superposition of different k states, such that some k-components field ionise at fields for which others only surface ionise.

The surface ionisation signal occurs only over a range of three or four hundred $\mathrm{V\,cm^{-1}}$, suggesting a much smaller range of surface ionisation distances than for a metallic surface. By converting the minimum extraction field into a minimum ionisation distance, D_{min} using equation 1.21 and the experimental velocity range, the surface ionisation occurs between $3n^2 \geq D_{\mathrm{min}} \geq 5n^2$. This is in keeping with the expected range of field ionisation distances for a metallic surface in the absence of any patch fields on the surface. However, the surface ionisation signal is independent of collisional velocity. As F_{min} should be dependent on the perpendicular collisional velocity, equation 1.21 does not appear to be a valid description.

Figure 6.6 plots the same surface ionisation profiles as figure 6.5 on a n^{-4} scaled field axis [4, 25, 101]. Using the scaled field axis shows that the surface ionisation profiles seen for the mica surface have a shape and width that is dependent on the principal quantum number of the hydrogen Rydberg atom. The onset of surface ionisation is seen consistently at $0.1n^{-4}$, but the field ionisation does not cut off at the scaled field.

The surface ionisation profiles presented in figure 6.5 suggest the occurrence of a hitherto unseen mechanism of surface ionisation, which is distinct from the normal Rydberg surface ionisation seen at metallic surfaces. The localised

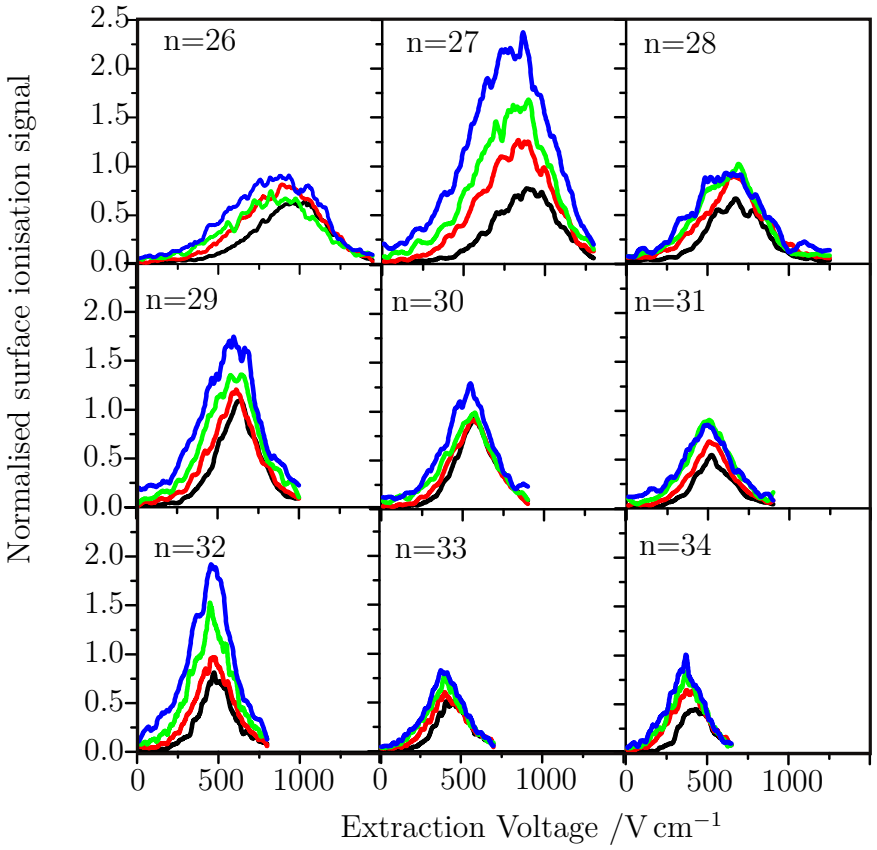

Figure 6.7: The surface ionisation profiles for the $k = 0$ $n = 26 - 34$ Hydrogen atom Rydberg states incident at a five monolayer iron thin film for a series of perpendicular collisional velocities. The black lines are for collisional velocities of 850m s^{-1}, the red 700m s^{-1}, the green 600m s^{-1} and the blue 500m s^{-1}.

bonding within the insulating muscovite surface suggests any induced image charge would be far more diffuse, and localised on specific atoms or bonds, than in the metallic case. The interpretation of these results requires further theoretical work.

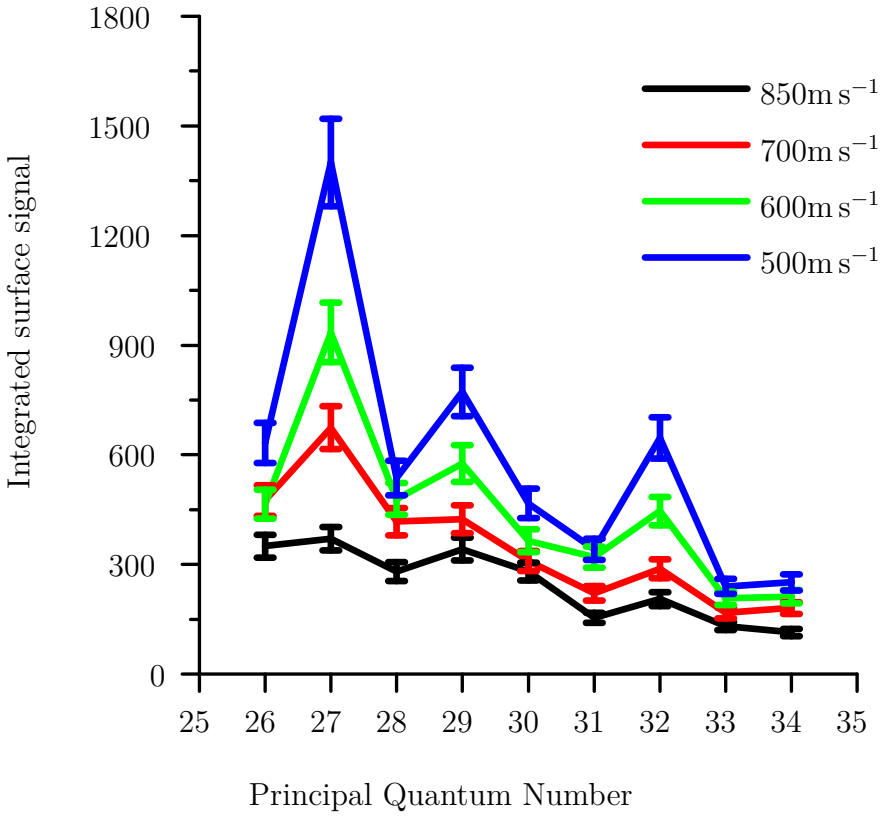

Figure 6.8: The integrated surface ionisation signal of the $n = 26 - 34$, $k = 0$ hydrogen atom Rydberg states with perpendicular collisional velocity 850m s^{-1} to 500m s^{-1}, at a five monolayer iron thin film.

6.4.2 Five monolayer iron thin film

Figure 6.7 plots the surface ionisation profiles for $n = 26 - 34$ hydrogen Rydberg atoms at a five-monolayer iron thin film on muscovite. The profiles were measured for four perpendicular collisional velocities, 850m s^{-1}, 700m s^{-1}, 600m s^{-1} and 500m s^{-1}. Due to the better conduction properties of the iron thin films, a Stark field was applied to the surface at the time of excitation, so the Rydberg atoms were prepared in the mid-manifold $k = 0$ state by spectroscopic selection.

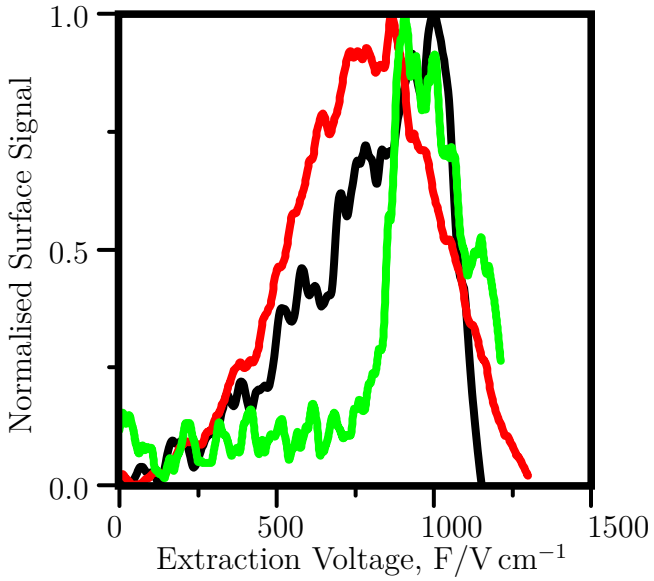

Figure 6.9: Surface ionisation profiles of the $n = 28$ 500m s^{-1} hydrogen atom Rydberg states incident at a Cu(100) surface in black, a 5 monolayer thin film in red and a muscovite surface in green. Note the maximum intensity of each profile has been normalised to 1 to aid comparison.

The surface ionisation profiles shown in figure 6.7 are significantly different to those in figure 6.5 , indicating that the form of these surface ionisation profiles is dominated by the interaction of the Rydberg atom with the thin metallic film, and not the muscovite surface. This supports the use of the free-standing thin film model to describe the behaviour.

Figure 6.9 shows the surface ionisation profile for the $n = 28$, 500m s^{-1} hydrogen Rydberg atom incident at a Cu(100) projected band gap surface, a bare Muscovite surface and a 5ML iron thin film on a muscovite base. The onset of field ionisation at an iron thin film is sharper and at lower fields than for the unpolarised Rydberg atoms at the bare muscovite surface. This behaviour is characteristic of a single Stark state rather than a superposition. However the onset of field ionisation is more gradual than for the $k = 0$

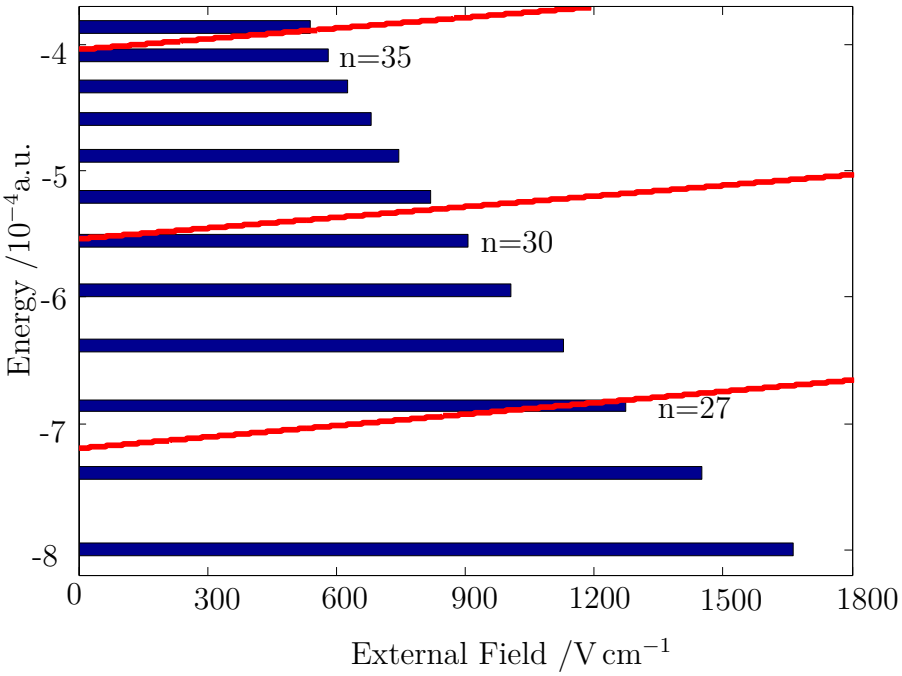

Figure 6.10: Energy level diagram of the five monolayer iron thin film and the $k = 0$, $n = 26 - 35$ hydrogen atom Rydberg states with the image-states in red and the Rydberg atom energies in blue.

copper measurements, suggesting that there is still some blurring of the field or ionisation signal by the muscovite substrate. The surface ionisation signal extends to nearly zero field, and the profile shape is similar to that observed for the Cu(100) measurements. Additionally there is significantly more signal for all of the profiles after normalisation than for the bare muscovite surface.

As figure 6.8 shows, principal quantum numbers $n = 27, 29, 32$ exhibit significantly more integrated surface ionisation signal than $n = 26, 28, 30, 31, 33, 34$, showing that there is resonance-enhanced charge transfer which we attribute to energy matching between the thin-film-localised well-image states and the Rydberg state. The energy level diagram in figure 6.10 predicts resonances at $n = 27, 30, 35$ for a five-monolayer thin film. This resonance-enhanced

charge transfer shows the preference for electron penetration along the surface normal, and suggests that the one-dimensional well-image states with low parallel momentum act as a conduit for electron density to pass into the degenerate band of higher angular momentum states associated with lower energy well-image states. Additionally the good matching between the experimental results and the theoretical energy level diagram provides evidence that the model used is accurate, and that therefore the thin-film-localised states are well-image states as described in section 6.1.

It is also observed that as the perpendicular collisional velocity changes the amount of surface ionisation signal increases. Decreasing velocity results in an increased mean atom-surface separation for surface ionisation, and a greater detectability of the ions. The acceleration on the Rydberg atom may mean these effects are exacerbated, as has been shown theoretically for a projected band gap surface [64]. For on-resonance states the effects are exaggerated more than off-resonant states. $n = 27$ shows a larger variation of integrated surface signal with velocity than its off-resonance neighbours. However for the on-resonance profiles, there is less of an obvious shape change than for the copper(100) measurements as described in chapter 5. The shape change seen for the Cu(100) surface is attributed to the field dependence of the resonance. The energies of the iron thin-film image-states in figure 6.10 change less with external field than the copper-localised image-states such that the resonance experienced is not as 'sharp' as a function of field, and less of a shape change is seen.

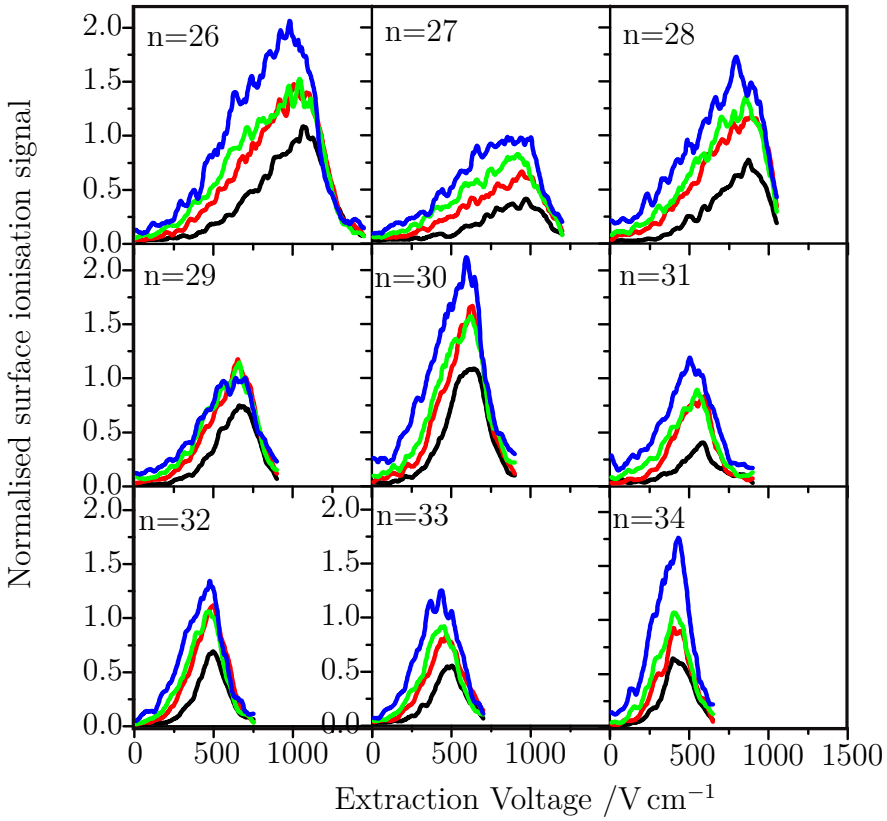

Figure 6.11: The surface ionisation profiles for the $k = 0$ $n = 26 - 34$ hydrogen atom Rydberg states incident at a ten monolayer iron thin film for a series of perpendicular collisional velocities. The black lines are for velocities of 850m s^{-1}, the red 700m s^{-1}, the green 600m s^{-1} and the blue 500m s^{-1}.

6.4.3 Ten monolayer iron thin film

By repeated deposition, thicker films can be prepared, in this case a film with an approximate thickness of ten monolayers or 1.14nm. Figure 6.12 shows the surface ionisation profiles for the $n = 26 - 34$, $k = 0$ hydrogen Rydberg atoms interacting with this surface at collisional velocities of 850m s^{-1}, 700m s^{-1}, 600m s^{-1} and 500m s^{-1}. The integrated surface ionisation

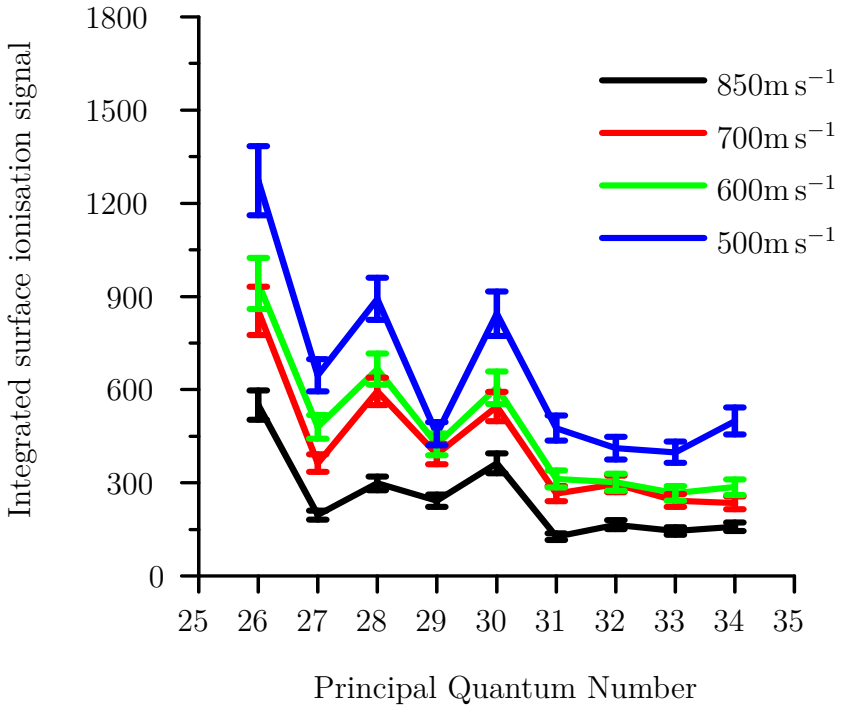

Figure 6.12: The integrated surface ionisation signal of the $n = 26 - 34$, $k = 0$ hydrogen atom Rydberg states with perpendicular collisional velocity 850m s^{-1} to 500m s^{-1}, at a ten monolayer iron thin film.

profile in figure 6.12 shows that there are again resonant principal quantum numbers.

For this thicker film the resonances occur at $n = 26, 28, 30, 34$ which are different than for the 0.67nm thick surface shown in figure 6.7. The movement of the peaks to different n indicates that the image-state energies have shifted for the thicker iron film, with the increased well width. Furthermore the peaks are closer together, $\Delta n = 2$ for the separation between resonances in the ten-monolayer case, rather than $\Delta n = 2, 3$ for the spacings in the five monolayer thin film shown in figure 6.8. The presence of the fourth resonance supports the expected particle-in-a-box style stacking of the energy levels

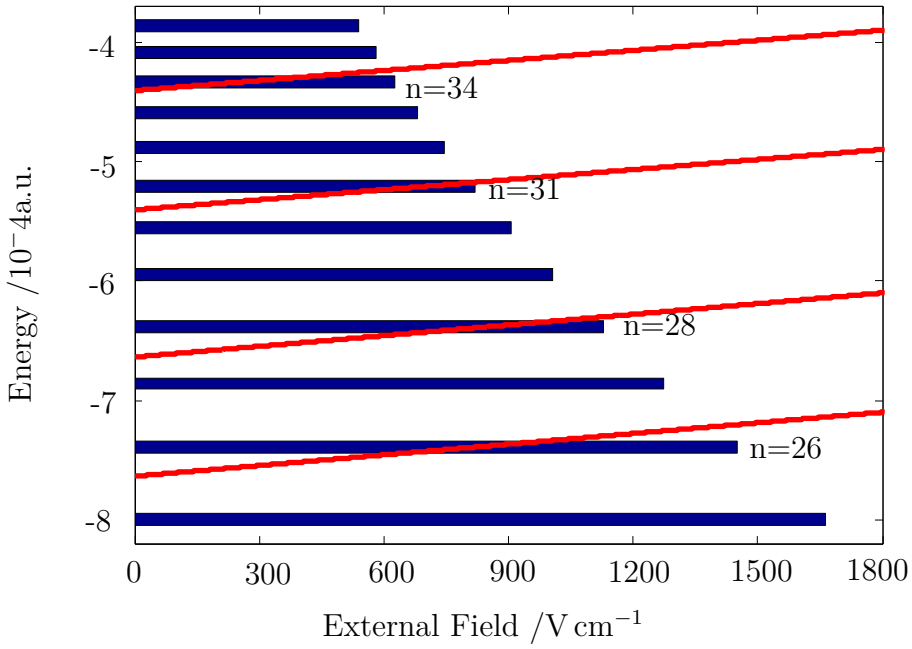

Figure 6.13: Energy level diagram of the twelve monolayer iron thin film and Rydberg system with the image-states in red and the Rydberg atom energies in blue.

within the thin film, with the film width determining the separation between the well-states ($E \propto n^2/L^2$ where L is the size of the box).

The calculated energy level diagram for a ten monolayer thin film does not show the same resonances as measured experimentally but it does show the correct number of resonances. However by using the thickness of the film (in monolayers) as a tuning parameter, a good match is found for the experimental measurements with the twelve monolayer energy level diagram which is within the experimental error in the film thickness as found from the XPS intensity analysis. This energy level diagram shown in figure 6.13 predicts resonances at $n = 26, 28, 31, 34$.

The velocity dependence of these surface ionisation profiles mirrors the

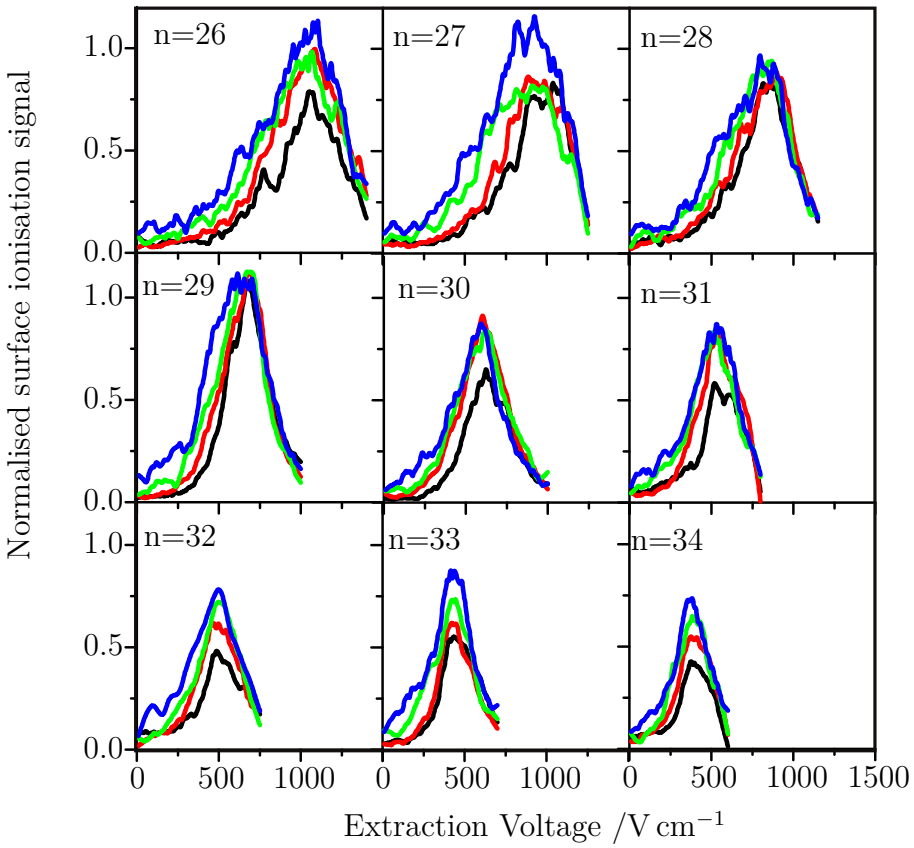

Figure 6.14: The surface ionisation profiles for the $k = 0$ $n = 26 - 34$ Hydrogen atom Rydberg states incident at a thirty monolayer iron thin film for a series of perpendicular collisional velocities. The black lines are for collisional velocities of 850m s^{-1}, the red 700m s^{-1}, the green 600m s^{-1} and the blue 500 m s^{-1}.

behaviour for the five-monolayer films with a greater spread of intensity with velocity for the on-resonance principal quantum numbers.

6.4.4 Thirty monolayer iron thin film

The surface ionisation profiles shown in figure 6.14 for the thirty-monolayer thin film have a much more monatomic variation with n than the surface ionisation profiles the other thin films. The maximum of the normalised

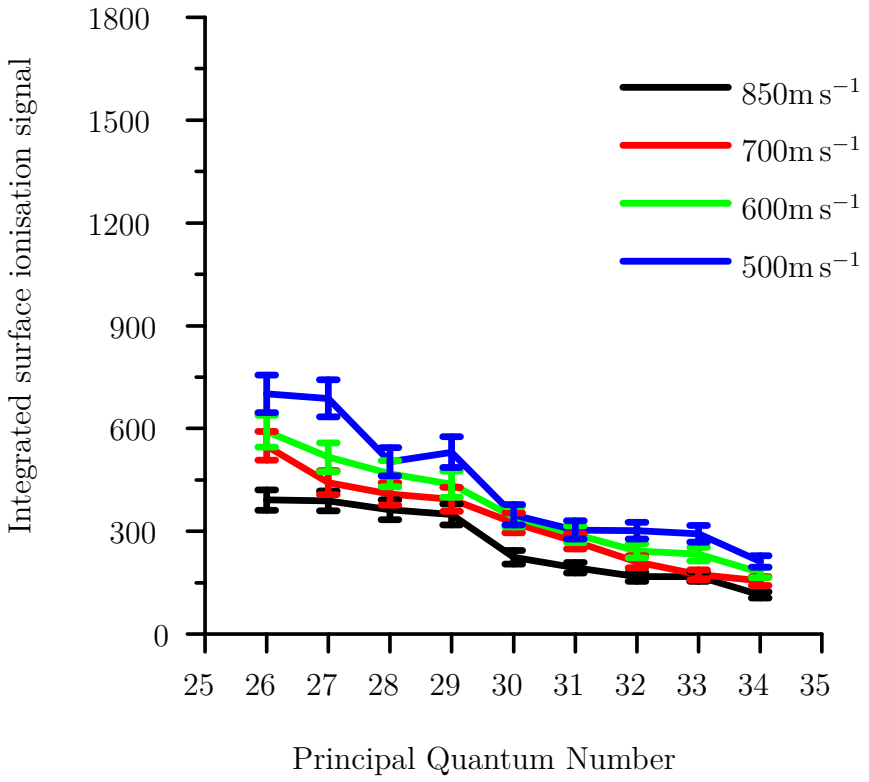

Figure 6.15: The integrated surface ionisation signal of the $n = 26 - 34$, $k = 0$ hydrogen atom Rydberg states with perpendicular collisional velocity 850 m s^{-1} to 500 m s^{-1}, at a thirty monolayer iron thin film.

surface ionisation signals occur between 0.5 and 1 and the variation of the integrated surface ionisation signal shown in figure 6.15 is far smoother behaving more like those expected for a bulk metal surface.

The calculated energy level diagram for the thirty-monolayer system shown in figure 6.16, shows that the spacings between the image-states are comparable in size to the spacings between the Rydberg atoms energies. As each Rydberg state is now in resonance with a well-image state, the thirty monolayer thin film can be thought of as 'bulk-like' with respect to the

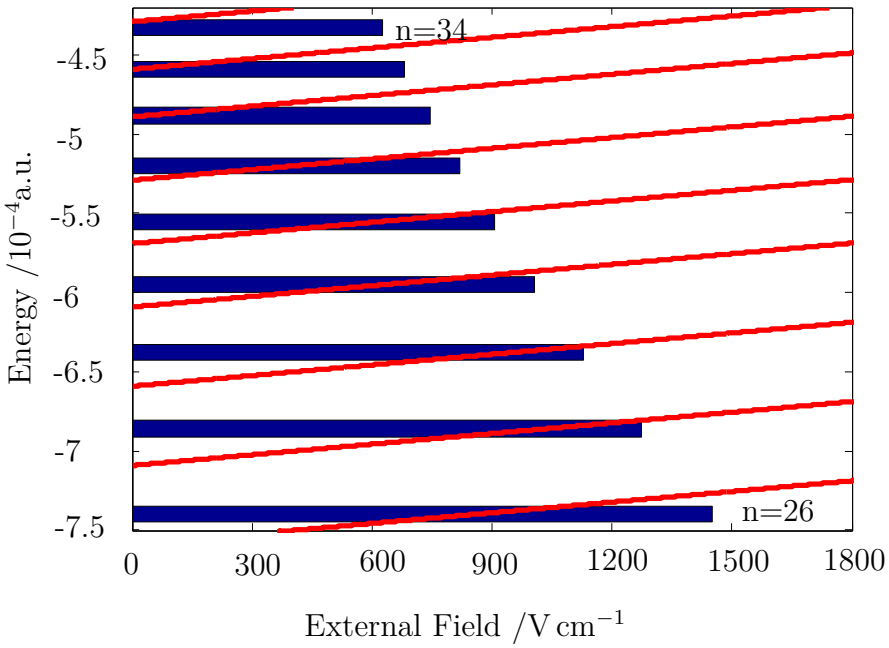

Figure 6.16: Energy level diagram of the thirty monolayer iron thin film and Rydberg system with the image-states in red and the Rydberg atom energies in blue.

resolution of our experiment, despite the energy levels along the surface normal still not forming a true continuum.

Figure 6.14 shows that the integrated surface ionisation signal increases as the principal quantum number is decreased, much as it would for a bulk metallic surface such as gold [5]. Lower-n H atoms field ionise at larger fields, and so can surface ionise over a greater range of voltages than high-n Rydberg atoms. Therefore the surface ionisation signal is integrated over a larger range of voltages, and increases with decreasing n. The small variation in integrated signal is likely to be due to a marginally better energy matching between Rydberg state and image-state energy levels for one n than another, but fundamentally the energies of all the principal quantum numbers overlap

with one or more well-image states.

The amount of surface ionisation signal for the thirty-monolayer thin film seems more comparable with the off-resonance Rydberg states for the 0.67nm and 1.14nm thin films. This can be understood by considering the wavefunctions of the thirty-monolayer thin film which are more contracted to the bulk, due to the greater contribution of the well-localised states for thicker films as described earlier in the chapter. The well-image states do not extend as far into the vacuum so there is poorer overlap with the incoming Rydberg state wavefunctions and less overall surface ionisation signal.

Finally, decreased perpendicular collisional velocity again increases the amount of surface ionisation signal, but by a smaller amount than seen for the other thin film systems.

6.4.5 Conclusions

The tunability of the well-image state energy with thin film thickness distinguishes this experimental work from a previous study probing image-state energies in Cu(100) [64,96]. Figure 6.17 plots the integrated surface ionisation signal for each of the thin films for a given collisional velocity. Clearly the surface ionisation behaviour changes with thin film thickness. The blue and red lines, which depict the integrated surface ionisation signal for the five- and twelve-monolayer thin films, have clear peaks at different principal quantum numbers, showing resonance-enhanced charge transfer occurring at different energies in the two thin films. The black line of the thirty monolayer thin film follows the trend expected for a bulk metallic surface, such as gold. The thirty

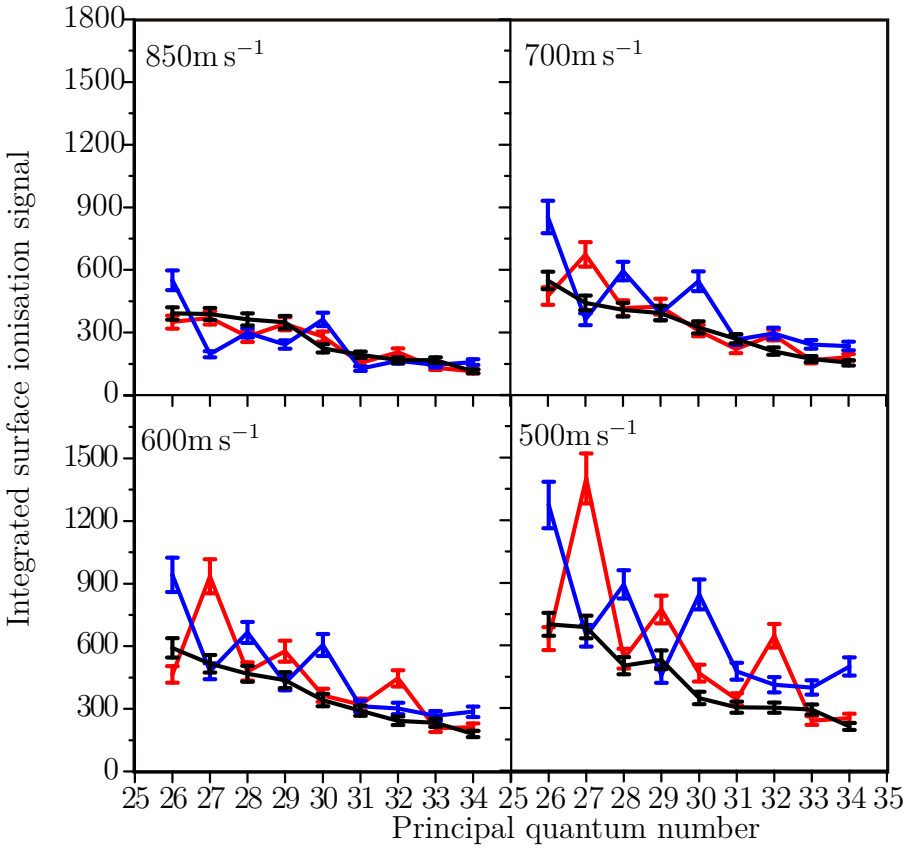

Figure 6.17: Integrated surface signal of the surface ionisation profiles of various thin film thicknesses at four collisional velocities. The red lines are the results from the five monolayer thin film, the blue the ten thin film and the black the thirty monolayer thin film.

monolayer system has a reduced amount of signal compared to the other thin films, with the exception of the set of measurements at highest velocity. However this particular data set is noisier due to the smaller overall signal at high velocities, and so is far more susceptible to issues with normalisation and noise. The bare muscovite measurements indicate a distinct, and previously unseen mechanism for surface ionisation in front of an insulator surface, which is not yet fully understood.

The image-state energy levels can be calculated by considering an electron outside of a 'soft' one-dimensional well, and determining the energies as a function of monolayer well thickness. The only fitting parameter required to match the experimental resonances with the theoretical resonance position is the well thickness, and good correlation between theory and experiment can be realised within the experimental error of the thin film thickness. The well-image state wavefunctions determined have significant combined image-state and particle-in-a-box character.

The velocity dependence of the surface ionisation process seems to be less complicated than for the previous copper study. This can be understood as the energies of thin film image-states are les sensitive to the external field than the Cu(100) image-states, and so the field dependence of the resonance is less pronounced. It is this field dependence which causes the shape change in the copper measurements [96].

Chapter 7

Conclusions and future work

The charge transfer of hydrogen Rydberg atoms to projected band gap surfaces, thin films and nanoparticles has been investigated theoretically and experimentally in this work. This extends previous studies investigating the surface ionisation dynamics of Rydberg hydrogen atoms at free-electron metal surfaces [5] to metallic structures with discrete states. A free-electron metal surface has image resonances which are broad and short lived because of their coupling to a degenerate conduction band, whereas projected band gap surfaces have pure zero-order image-states which are discrete and relatively long-lived. For the nanoparticles and the thin films investigated here hybrid well-image-states are formed from the overlap of image-states and localised discrete states within the metallic structure. Resonance-enhanced charge transfer has been seen for the first time in such surfaces.

Resonance-enhanced charge transfer has been seen conclusively for the first time between Rydberg atoms and a projected band gap surface in experiments presented here [96]. At specific principal quantum numbers, the energy of the

copper localised image-state and the Rydberg hydrogen atom match and an increase is seen in the surface ionisation signal at low fields, as the Rydberg atom is surface ionising further from the surface. The measurements involving the Cu(100) surface allowed the $n_{\mathrm{img}} \geq 5$ image-states of the surface to be directly measured for the first time. Previously such states were only accessible using a quantum-beat variant of two-photon photoexcitation spectroscopy. A simple model predicting the energies of the image-states in the absence of the ion core, and the Rydberg energies in the presence of a metal surface predicts reasonably well the principal quantum numbers at which resonances occur. More surface ionisation signal is seen for on-resonance Rydberg atoms at a Cu(100) surface, than for the same Rydberg atom incident at a gold free-electron surface, due to the pure image-state orbital protruding into the vacuum further than the image resonance and therefore overlapping better with the Rydberg-state wavefunction.

Wavepacket propagation calculations carried out for the copper projected band gap surface and low principal quantum number Rydberg hydrogen atoms predict resonance-enhanced charge transfer when the Rydberg state and image-state are degenerate [64]. Additionally these calculations were extended to investigate the velocity dependence of such effects. Generally a decrease in collisional velocity results in a shift in the surface-ionisation probability to larger mean atom-surface separations. Therefore a lower field is required to extract the ion, such that there is more surface ionisation signal at low fields, when the collisional velocity is decreased. As the shift with velocity in the mean surface ionisation atom-surface separation is larger for on-resonance principal quantum numbers it is expected that the change in

surface ionisation profile with collisional velocity will be more extreme for on-resonant states, such that tuning the velocity can be used to enhance sensitivity to any resonance effects present. Experimentally this was seen, however the field dependence of the resonance resulted in an additional shape change for on-resonant hydrogen Rydberg atoms.

The well-localised states in a thin metallic film drop in energy as the film thickness is increased, such that the energy and probability density of the hybrid well-image states which protrude into the vacuum also change. A thicker film results in more well-image states, which are closer in energy and have more well-state character. Wavepacket propagation calculations in my M.Chem part II thesis predicted a strong preference for charge transfer via one of these hybrid well-image states, rather than via a higher angular momentum state [79]. Iron thin films on a muscovite base were deposited in situ and the thickness monitored using an in-situ ion flux monitor and confirmed with XPS. A film of 5ML thickness had three resonances with the hydrogen Rydberg atoms. An additional deposition of 12ML changed the resonant principal quantum numbers and increased the number of resonant principal quantum numbers to 4. The resonant principal quantum numbers for both thin films were predicted within the experimental error of the film thickness using a simple model which treats the thin film as a soft-sided one-dimensional jellium well. The same model predicts that for a metallic film 30ML thick, the spacings between the well-image states are comparable to the spacings between the Rydberg states such that individual resonances are no longer resolvable. Experimental investigation of a 30ML thin film resulted in no variation with principal quantum number, and an overall decrease in

the amount of surface ionisation signal relative to the on-resonant states for the thinner metallic films. Assessment of the probability density of the well-image states revealed an increasing contribution from the well-localised states. This is unsurprising as the number of image-states is fixed, but as the film thickness increases there are more well-states to overlap with, such that the resulting well-image states have less image-state character and so do not protrude as far into the vacuum.

Resonance-enhanced charge transfer has been theoretically investigated for hydrogen Rydberg atoms at a nanoparticle, using a wavepacket propagation method following experimental work in the Softley group [80] using gold-nanoparticle coated surfaces. The nanoparticle has three-dimensional confinement and has discrete well-image states. Strong resonance effects are predicted when there is good energy matching between the nanoparticle well-image state and the hydrogen Rydberg state. When there is a significant energy gap between the Rydberg atom and the well-image state there is no measurable charge transfer into the nanoparticle. Such large variations between on- and off-resonant states make this a very tempting system to study experimentally however the level of control required during surface production makes it challenging, and the previous study struggled to resolve resonance effects [80]. However if a surface with monolayer coverage of regularly sized nanoparticles, could be prepared in-situ then the resonance effects would be expected to be striking. As the density of well-image states scales roughly with particle size, in the same way that the density of Rydberg states scales with orbital size, then these effects should be measurable even for larger nanoparticles for atoms and nanoparticles of comparable size.

Measurable resonance effects in discrete objects such as nanoparticles, allow for the possibility of using Rydberg surface ionisation to spatially map a surface. By using a particular Rydberg state resonance and a fixed extraction field, and then either moving the Rydberg beam across the surface, or improving the spatial mapping of the detection setup such that the positions that ions are formed at are accurately translated into a position on the imaging detector, then a two-dimensional image of the surface could be produced. At the moment the presence of large applied fields and the current form of the detection setup mean that the spatial resolution is poor, and we can only clearly resolve the differences between the field and surface ionisation signals, not the position from which individual ions are extracted.

An interesting extension of the two experimental studies presented in this thesis would be to measure the surface ionisation profiles of hydrogen Rydberg atoms incident at a series of iron thin films deposited on a Cu(100) projected band gap surface. The image-states and Rydberg-surface ionisation dynamics of a similar system, lead thin films on a Cu(111) surface, have been investigated theoretically previously and a wavepacket propagation study showed that resonance effects with Rydberg atoms were possible [102, 103]. The projected band gap surface is expected to modify the well depth of the one dimensional thin film potential, such that electrons are confined to the thin films for a smaller energy range. It is expected that similar trends with film thickness would be observed as for the thin films on an insulator substrate, but the locations of the resonances would be different.

The velocity dependence of the copper surface ionisation profiles and the corresponding wavepacket propagation calculations show a complex de-

pendence of the surface ionisation process on the collisional velocity of the Rydberg atom. In order to expand the range of accessible experimental velocities a chip Rydberg-Stark decelerator is being installed in front of the surface [16]. Similar chip decelerators have been used to successfully decelerate and trap Rydberg atoms previously. Additionally, in the longer term, it may to be possible to trap cold Rydberg atoms (eg. alkali metal atoms) at a fixed distance in front of the surface, such that the Rydberg-surface interaction can be measured as a function of distance [104].

Additionally the surface ionisation profiles for hydrogen Rydberg atoms incident at a insulating muscovite surface, shown in section 6.4.1, suggest further work is needed to understand the interaction of Rydberg atoms and insulating surfaces. The measurable surface ionisation signal does not behave as expected based on previous studies involving conducting and semi-conducting surfaces. However, a different kinds of resonance effect has been observed by Pfau and coworkers involving surface polariton states at an insulating surface [105].

To conclude, the work in this thesis shows that resonance-enhanced charge transfer from a hydrogen Rydberg atom to a discrete metal structure is experimentally measurable, and can be predicted using theoretical methods. Such experiments illustrate that Rydberg surface-ionisation can be used as a probe of surface structure, particularly when the surface has a high-lying discrete image-states which would otherwise be difficult to study.

Bibliography

[1] C. Fabre, M. Gross, J. M. Raimond, and S. Haroche. Measuring atomic dimensions by transmission of Rydberg atoms through micrometre size slits. *J. Phys. B*, 16(21):L671, 1983.

[2] C. A. Kocher and C. R. Taylor. High-Rydberg atoms as probes of surface electric fields and sub-monolayer adsorption. *Phys. Lett. A*, 124(1-2):68 – 72, 1987.

[3] G. E. McCown, C. R. Taylor, and C. A. Kocher. Excited-state atomic-beam studies of submonolayer adsorption on a fine mesh. *Phys. Rev. A*, 38(8):3918–3936, 1988.

[4] F.B. Dunning, S. Wethekam, H.R. Dunham, and J.C. Lancaster. Charge transfer rates for xenon Rydberg atoms at metal and semiconductor surfaces. *Nucl. Instrum. Methods Phys. Res., Sect. B*, 258:61–67, 2007.

[5] E. So, M. Dethlefsen, M. Ford, and T. Softley. Charge transfer of Rydberg H atoms at a metal surface. *Phys. Rev. Lett.*, 107:093201, 2011.

[6] E. So, M. T. Bell, and T. P. Softley. Wave-packet propagation study of the charge-transfer dynamics of Rydberg atoms with metal surfaces. *Phys. Rev. A*, 79(1):012901, 2009.

[7] D. F. Gray, Z. Zheng, K. A. Smith, and F. B. Dunning. Ionization of K(nd) Rydberg-state atoms at a surface. *Phys. Rev. A*, 38:1601–1603, Aug 1988.

[8] J. Hanssen, C. F Martin, and P. Nordlander. Dynamics of Rydberg atoms near metal surfaces in the presence of an electric field. *Surf. Sci.*, 423:L271 – L276, 1999.

[9] E. Yu. Usman, I. F. Urazgil'din, A. G. Borisov, and J. P. Gauyacq. Quantum size effect in the resonant electron transfer between an ion and a thin metal film. *Phys. Rev. B*, 64:205405, 2001.

[10] G. Sashikesh, E. So, M. S. Ford, and T. P. Softley. Surface ionisation of molecular H_2 and atomic H Rydberg states at doped silicon surfaces. *Mol. Phys.*, 112:2495–2503, 2014.

[11] Y. Pu, D. D. Neufeld, and F. B. Dunning. Ionisation of Rydberg atoms at metallic surfaces: Influence of stray fields. *Phys. Rev. A*, 81:042904, 2010.

[12] T. F. Gallagher. *Rydberg atoms*. Cambridge University Press, 1994.

[13] G. R. Lloyd, S. R. Procter, and T. P. Softley. Ionisation of hydrogen Rydberg molecules at a metal surface. *Phys. Rev. Lett.*, 95(13):133202, 2005.

[14] D. Townsend, A. L. Goodgame, S. R. Procter, S. R. Mackenzie, and T. P. Softley. Deflection of krypton Rydberg atoms in the field of an electric dipole. *J. Phys. B*, 34(3):439, 2001.

[15] Y Yamakita, S. R. Procter, A. L. Goodgame, T. P. Softley, and F Merkt. Deflection and deceleration of hydrogen Rydberg molecules in inhomogeneous electric fields. *J. Chem. Phys*, 121(3):1419–1431, 2004.

[16] S. D. Hogan, P. Allmendinger, H. Saßmannshausen, H. Schmutz, and F. Merkt. Surface-electrode Rydberg-Stark decelerator. *Phys. Rev. Lett.*, 108:063008, Feb 2012.

[17] T. P. Softley. Applications of molcular Rydberg states in chemical dynamics and spectroscopy. *Int. Rev. Phys. Chem.*, 23:1, 2004.

[18] H. Bethe and E. Salpeter. Quantum mechanics of one- and two-electron atoms. *Plenum Publishing Corporation, New York,*, 1977.

[19] J. D. Bekenstein and J. B. Krieger. Stark effect in hydrogenic atoms: Comparison of fourth-order perturbation theory with WKB approximation. *Phys. Rev.*, 188:130–139, 1969.

[20] M. A. Cazalilla, N. Lorente, R. D. Muino, J. P. Gauyacq, D. Teillet-Billy, and P. M. Echenique. Theory of Auger neutralization and deexcitation of slow ions at metal surfaces. *Phys. Rev. B*, 58(20):13991–14006, 1998.

[21] K. Ganesan and K. T. Taylor. Rydberg states of the hydrogen atom near a metal surface. *J. Phys. B*, 29(7):1293, 1996.

[22] A. G. Borisov, R. Zimny, D. Teillet-Billy, and J. P. Gauyacq. Energy and lifetime of one-electron multicharged-ion states in front of an Al surface. *Phys. Rev. A*, 53(4):2457–2465, 1996.

[23] P. J. Jennings, R. O. Jones, and M. Weinert. Surface barrier for electrons in metals. *Phys. Rev. B*, 37(11):6113–6120, 1988.

[24] E.V. Chulkov, V.M. Silkin, and P.M. Echenique. Image potential states on metal surfaces: binding energies and wave functions. *Surf. Sci.*, 437(3):330 – 352, 1999.

[25] E. So. Interaction of Rydberg hydrogen atoms with metal surfaces. *Dphil thesis*, 2011.

[26] W. P. Reinhardt. Complex coordinates in the theory of atomic and molecular-structure and dynamics. *Annu Rev Phys Chem*, 33:223–255, 1982.

[27] S. B. Hill, C. B. Haich, Z. Zhou, P. Nordlander, and F. B. Dunning. Ionisation of xenon Rydberg atoms at a metal surface. *Phys. Rev. Lett.*, 85(25):5444–5447, 2000.

[28] Z. Zhou, C. Oubre, S. B. Hill, P. Nordlander, and F. B. Dunning. Ionisation of xenon Rydberg atoms at surfaces. *Nucl. Instrum. Methods*, 193(1-4):403 – 407, 2002.

[29] P. Nordlander and F. B. Dunning. Interaction of Rydberg atoms with a metal surface in the presence of an external electric field. *Phys. Rev. B*, 53(12):8083–8089, 1996.

[30] D. D. Neufeld, H. R. Dunham, S. Wethekam, J. C. Lancaster, and F. B. Dunning. ionisation of xenon Rydberg atoms at Au(111) surfaces: Effect of stray fields. *Phys. Rev. B*, 78:115423, 2008.

[31] G. R. Lloyd, S. R. Procter, E. A. McCormack, and T. P. Softley. ionisation of H_2 Rydberg molecules at a metal surface. *J. Chem. Phys.*, 126(18), 2007.

[32] J. J. Paggel, T. Miller, and T.-C. Chiang. Quantum-well-states as fabry-perot modes in a thin-film electron interferometer. *Science*, 283(5408):1709–1711, 1999.

[33] P. Rinke, K. Delaney, P. García-González, and R. W. Godby. Image-states in metal clusters. *Phys. Rev. A*, 70(6):063201, 2004.

[34] M. N. Martin, J. I. Basham, and S. Chando, P.and Eah. Charged gold nanoparticles in non-polar solvents: 10-min synthesis and 2d self-assembly. *Langmuir*, 26(10):7410–7417, 2010.

[35] I. E. Tamm. Über eine mögliche art der elektronenbindung an kristall-loberflechen. *Z. Physik*, 76(11-12):849–850, 1932.

[36] W. Shockley. On the surface states associated with a periodic potential. *Phys. Rev.*, 56(4):317–323, 1939.

[37] D. Straub and F. J. Himpsel. Spectroscopy of image-potential states with inverse photoemission. *Phys. Rev. B*, 33:2256–2262, 1986.

[38] T. Klamroth, P. Saalfrank, and U. Höfer. Open-system density-matrix approach to image-potential dynamics of electrons at Cu(100): Energy-

and time-resolved two-photon photoemission spectra. *Phys. Rev. B*, 64(3):0, 2001.

[39] P. M. Echenique and J. B. Pendry. Existence and detection of Rydberg states at surfaces. *J. Phys. C Solid State*, 11(10):2065–2075, 1978.

[40] T. Fauster, F. J. Himpsel, J. J. , and A. Marx. Spectrometer for momentum resolved bremsstrahlung spectroscopy. *Rev. Sci. Instrum.*, 54(1):68–75, 1983.

[41] K. Giesen, F. Hage, F. J. Himpsel, H. J. Riess, and W. Steinmann. Binding energy of image-potential states: Dependence on crystal structure and material. *Phys. Rev. B*, 35:971–974, 1987.

[42] U. Höfer, I. L. Shumay, Ch. Reuss, U. Thomann, W. Wallauer, and Th. Fauster. Time-resolved coherent photoelectron spectroscopy of quantized electronic states on metal surfaces. *Science*, 277(5331):1480–1482, 1997.

[43] T. Hecht, H. Winter, A. G. Borisov, J. P. Gauyacq, and A. K. Kazansky. Role of the 2d surface state continuum and projected band gap in charge transfer in front of a Cu(111) surface. *Phys. Rev. Lett.*, 84:2517–2520, 2000.

[44] D. F. Padowitz, W. R. Merry, R. E. Jordan, and C. B. Harris. Two-photon photoemission as a probe of electron interactions with atomically thin dielectric films on metal surfaces. *Phys. Rev. Lett.*, 69:3583–3586, 1992.

[45] M. Milun, P. Pervan, and D. P. Woodruff. Quantum well structures in thin metal films: simple model physics in reality? *Rep. on Prog. Phys.*, 65(2):99, 2002.

[46] T. C Chiang. Photoemission studies of quantum well-states in thin films. *Surf. Sci.Reports*, 39:181 – 235, 2000.

[47] R. K. Kawakami, E. Rotenberg, H. J. Choi, E. J. Escorcia-Aparicio, M. O. Bowen, J. H. Wolfe, E. Arenholz, Z. D. Zhang, N. V. Smith, and Z. Q. Qiu. Quantum-well-states in copper thin films. *Nature*, 398:132–134, 1998.

[48] P. Wahl, M. A. Schneider, L. Diekhöner, R. Vogelgesang, and K. Kern. Quantum coherence of image-potential states. *Phys. Rev. Lett.*, 91:106802, 2003.

[49] J.W. Gadzuk. Theory of atom-metal interactions: I. alkali atom adsorption. *Surf. Sci.*, 6(2):133 – 158, 1967.

[50] M. Remy. Theory concerning the interaction of an alkali metal and a metallic surface. *J. Chem. Phys.*, 53:2487, 1970.

[51] P. Nordlander. Energies and lifetimes of atomic Rydberg states near metal surfaces. *Phys. Rev. B*, 53(7):4125–4132, 1996.

[52] P. Nordlander and J. C. Tully. Energy shifts and broadening of atomic levels near metal surfaces. *Phys. Rev. B*, 42(9):5564–5578, 1990.

[53] P. Nordlander and F. B. Dunning. Interaction of Rydberg atoms with surfaces: Electron tunneling processes. *Nucl. Instrum. Methods*, 125(1-4):300 – 304, 1997.

[54] D. Wang, M. L. Du, and S. Lin. Application of closed-orbit theory to the Rydberg hydrogen atom near a metal surface. *J. Phys. B*, 39(17):3529, 2006.

[55] J. Burgdörfer, P. Lerner, and F. W. Meyer. Above-surface neutralization of highly charged ions: The classical over-the-barrier model. *Phys. Rev. A*, 44(9):5674–5685, 1991.

[56] A. G. Borisov, D. Teillet-Billy, and J. P. Gauyacq. Energy shift and broadening of H levels in front of a metal surface. *Nucl. Instrum. Methods B*, 78(1-4):49 – 55, 1993.

[57] N. Shenvi, H. Cheng, and J. C. Tully. Nonadiabatic dynamics near metal surfaces: Decoupling quantum equations of motion in the wide-band limit. *Phys. Rev. A*, 74(6):062902, Dec 2006.

[58] A. G. Borisov, A. K. Kazansky, and J. P. Gauyacq. Resonant charge transfer in ion–metal surface collisions: Effect of a projected band gap in the $H^- - Cu(111)$ system. *Phys. Rev. B*, 59(16):10935–10949, 1999.

[59] J. Sjakste, A. G. Borisov, and J. P. Gauyacq. Ionisation of Rydberg atoms colliding with a metal surface. *Phys. Rev. A*, 73(4):042903, 2006.

[60] J. Sjakste, A. G. Borisov, J. P. Gauyacq, and A. K. Kazansky. Analysis of the population of continuum states in wave packet propagation calculations. *J. Phys. B*, 37(8):1593, 2004.

[61] John C. Light and Tucker Carrington. *Discrete-Variable Representations and their Utilization*, pages 263–310. John Wiley and Sons, Inc., 2007.

[62] J. V. Lill, G. A. Parker, and J. C. Light. Discrete variable representations and sudden models in quantum scattering theory. *Chem. Phys. Lett.*, 89(6):483 – 489, 1982.

[63] K M Dunseath, J-M Launay, M Terao-Dunseath, and L Mouret. Schwartz interpolation for problems involving the Coulomb potential. *J. Phys. B*, 35(16):3539, 2002.

[64] E. So, J. A. Gibbard, and T. P. Softley. Ionisation of Rydberg H atoms at band gap metal surfaces via surface and image-states. *arXiv*, 1504:07172, 2015.

[65] A. R. Barnett. Coulfg: Coulomb and bessel functions and their derivatives, for real arguments, by steed's method. *Comput. Phys. Commun.*, 27(2):147 – 166, 1982.

[66] W. H. Press, S. A. Teukolsky, B. P. Flannery, and W. T. Vetterling. Numerical recipes in Fortran: The art of scientific computing. 1992.

[67] D. Baye, M. Hesse, and M. Vincke. The unexplained accuracy of the Lagrange-mesh method. *Phys. Rev. E*, 65(2):026701, 2002.

[68] D. Baye. Constant-step Lagrange meshes for central potentials. *J. Phys. B*, 28(20):4399, 1995.

[69] M. Vincke and D. Baye. Hydrogen molecular ion in an aligned strong magnetic field by the Lagrange-mesh method. *J. Phys. B*, 39(11):2605, 2006.

[70] D. T. Colbert and W. H. Miller. A novel discrete variable representation for quantum mechanical reactive scattering via the S-matrix Kohn method. *J. Chem. Phys.*, 96(3):1982–1991, 1992.

[71] D. Morgan, A. J. H. M. Meijer, and R. J. Doyle. Spectral difference methods in bound state calculations. *J. Chem. Phys.*, 130(8):084114, 2009.

[72] M. H. Beck, A. Jockle, G. A. Worth, and H. D. Meyer. The multiconfiguration time-dependent hartree method: A highly efficient algorithm for propagating wavepackets. *Phys. Reports Rev. Sect. Of Phys. Lett.*, 324(1):1–105, 2000.

[73] A. G. Borisov, J. P. Gauyacq, A. K. Kazansky, E. V. Chulkov, V. M. Silkin, and P. M. Echenique. Long-lived excited states at surfaces: Cs/Cu(111) and Cs/Cu(100) systems. *Phys. Rev. Lett.*, 86(3):488–491, 2001.

[74] A. G. Borisov, J. P. Gauyacq, and A. K. Kazansky. Scattering by alkali adsorbates as a decay mechanism for image potential states on Cu surfaces. *Surf. Sci.*, 505(1-3):260–270, 2002.

[75] D. E. Manolopoulos. Derivation and reflection properties of a transmission-free absorbing potential. *J. Chem. Phys.*, 117(21):9552–9559, 2002.

[76] T. Gonzalez-Lezana, E. J. Rackham, and D. E. Manolopoulos. Quantum reactive scattering with a transmission-free absorbing potential. *J. Chem. Phys.*, 120(5):2247–2254, 2004.

[77] M. D. Feit and J. A. Fleck. Solution of the schrödinger equation by a spectral method ii: Vibrational energy levels of triatomic molecules. *J. Chem. Phys.*, 78:301, 1983.

[78] J. C. Tully. Mixed quantum-classical dynamics. *Faraday Discuss.*, 110:407–419, 1998.

[79] J. A. Gibbard. The interaction of Rydberg atoms and quantum wells, thin films and nanoparticles. *Part II thesis*, 2011.

[80] M. G. B. Dethlefsen. Charge transfer processes of atomic hydrogen Rydberg states near surfaces. *D.Phil thesis*, 2013.

[81] V. Kasperovich, K. Wong, G. Tikhonov, and V. V. Kresin. Electron capture by the image charge of a metal nanoparticle. *Phys. Rev. Lett.*, 85:2729–2732, Sep 2000.

[82] S. Willitsch, J. M. Dyke, and F. Merkt. *Helv. Chim. Acta.*, 86(4):1152–1166, 2003.

[83] R. Hilbig and R. Wallenstein. Enhanced production of tunable VUV radiation by phase-matched frequency tripling in krypton and xenon. *J. Quant. Elec.*, 17(8):1566, 1981.

[84] W. L. Fite and R. T. Brackmann. Collisions of electrons with hydrogen atoms. ii. excitation of lyman-alpha radiation. *Phys. Rev.*, 112:1151–1156, Nov 1958.

[85] E. A. McCormack, E. So, M. Dethlefsen, M. S. Ford, and T. P. Softley. Detection of electrons in the surface ionization of H Rydberg atoms and H_2 Rydberg molecules. *Journal of Physics B: Atomic, Molecular and Optical Physics*, 45(1):015204, 2012.

[86] William H. Aberth, Rafael Schnitzer, and Ferdinand C. Engesser. Construction of an einzel lens capable of high voltage operation. *Rev. Sci. Instrum.*, 45(10):1289–1290, 1974.

[87] W. C. Wiley and I. H. McLaren. Time of flight mass spectrometer with improved resolution. *Rev. Sci. Instrum.*, 26(12):1150–1157, 1955.

[88] M. Nobre, A. Fernandes, F. Ferreira da Silva, R. Antunes, D. Almeida, V. Kokhan, S. V. Hoffmann, N. J. Mason, S. Eden, and P. Limao-Vieira. The vuv electronic spectroscopy of acetone studied by synchrotron radiation. *Phys. Chem. Chem. Phys.*, 10:550–560, 2008.

[89] T.W. Fishlock, J.B. Pethica, and R.G. Egdell. Observation of a nanoscale chessboard superstructure in the Br^- Cu(100) adsorbate system. *Surf. Sci.*, 445(1):L47 – L52, 2000.

[90] D. P. Woodruff and T. A. Delchar. Modern techniques of surface science. 1986.

[91] Briggs and Grant. Surface analysis by Auger and X-ray photoelectron spectroscopy. 2003.

[92] F. Pesty and P. Garoche. Low-energy electron beam on an insulator surface: Impact of the charging process on the diffraction by mica muscovite. *Surf. Sci.*, 580(1 - 3):153 – 162, 2005.

[93] S. Andersson. Low-energy electron diffraction intensities from the clean copper (001) surface. *Surf. Sci.*, 18(2):325 – 340, 1969.

[94] Y. Pu and F. B. Dunning. Ionisation of Rydberg atoms at patterned electrode arrays. *Phys. Rev. A*, 88:012901, 2013.

[95] L. Fitzgibbon. A theoretical study of the interaction of Rydberg states with metal surfaces and thin films. *Part II*, 2009.

[96] J. A. Gibbard, M. Dethlefsen, M. Kohlhoff, C. J. Rennick, E. So, M. Ford, and T. P. Softley. Resonant charge transfer of hydrogen Rydberg atoms incident at a Cu(100) projected band-gap surface. *arXiv*, 1504:07191, 2015.

[97] Appendix 5 - effective ionic radii in pm for various oxidation states. In N. N. Greenwood and A. Earnshaw, editors, *Chemistry of the Elements (Second Edition)*, pages 1295 –. 1997.

[98] A Howard, D.N.S Clark, C.E.J Mitchell, R.G Egdell, and V.R Dhanak. Initial and final state effects in photoemission from Au nanoclusters on TiO_2. *Surf. Sci.*, 518(3):210 – 224, 2002.

[99] S. Tougaard and B. Jorgensen. Inelastic background intensities in XPS spectra. *Surf. Sci.*, 143(2−3):482 – 494, 1984.

[100] Briggs Wagner and Seah. Practical surface analysis. 1990.

[101] D. D. Neufeld, H. R. Dunham, S. Wethekam, J. C. Lancaster, and F. B. Dunning. ionisation of xenon Rydberg atoms at Au(111) surfaces: Effect of stray fields. *Phys. Rev. B*, 78(11):115423, 2008.

[102] A. Zugarramurdi, N. Zabala, V. M. Silkin, E. V. Chulkov, and A. G. Borisov. Quantum-well-states with image-state character for Pb overlayers on Cu(111). *Phys. Rev. B*, 86:075434, Aug 2012.

[103] C. Green. Wavepacket propagation studies of rydberg interactions with surfaces and thin films. *Part II thesis*, 2013.

[104] A. Tauschinsky, R. M. T. Thijssen, S. Whitlock, H. B. van Linden van den Heuvell, and R. J. C. Spreeuw. Spatially resolved excitation of Rydberg atoms and surface effects on an atom chip. *Phys. Rev. A*, 81:063411, 2010.

[105] H. Kuebler, J. P. Shaffer, T. Baluktsian, R. Loew, and T. Pfau. Coherent excitation of Rydberg atoms in micrometre-sized atomic vapour cells. *Nat. Photonics.*, 4(2):112–116, 2010.